Huazhong Normal University
Wuhan, CHINA

Event anisotropy v_2 at STAR

A dissertation submitted
for the degree of
Doctor of Philosophy in Physics

by

Shusu Shi

Co-supervisors: Feng Liu and Nu Xu

March 2010

Abstract

At the early stages of relativistic heavy ion collisions, a hot and dense, strongly interacting medium is created. The subsequent system evolution is determined by the nature of the medium. Experimentally, the dynamics of the system evolution has been studied by measuring the azimuthal anisotropy of the particle production relative to the reaction plane. The centrality of the collision, defined by the transverse distance between the centers of the colliding nuclei called the impact parameter, results in an "almond-shaped" overlap region that is spatially azimuthal anisotropic. It is generally assumed that the initial spatial anisotropy in the system is converted into momentum-space anisotropy through re-scatterings. The elliptic flow, v_2, is the second harmonic coefficient of a Fourier expansion of the final momentum-space azimuthal anisotropy. Due to the self-quenching effect, it provides information about the dynamics at the early stage of the collisions. Elliptic flow can provide information about the pressure gradients, the effective degrees of freedom, the degree of thermalization, and equation of state of the matter created at the early stage. Thus, the centrality and system-size dependence of elliptic flow at different beam energies can be used to study the properties of the matter created in heavy ion collisions.

In this thesis, we analyze the data collected with the STAR detector from $\sqrt{s_{NN}} =$ 62.4 and 200 GeV Cu+Cu collisions during the fifth RHIC run in 2005 and $\sqrt{s_{NN}} = 9.2$ and 200 GeV Au+Au collisions during the seventh run in 2007. We present results on elliptic flow v_2 of identified particles in Au+Au collisions at $\sqrt{s_{NN}} = 200$ GeV. With the large statistics of the RHIC seventh run in 2007, we measured multi-strange hadrons, ϕ and Ω v_2 in high precision. We find they flow almost as strong as pion and proton. As multi-strange hadrons are created at the early stage of the collisions, and they are less sensitive to the late hadronic process with their smaller hadronic cross section, thus, the significant v_2 of multi-strange hadrons indicates the partonic collectivity has been built up in the heavy ion collisions at RHIC. The Number of Quark (NQ) scaling reflects constituent quark is the most effect degree of freedom in determining hadron flow at intermediate p_T. This suggests that the system has been in the deconfined state prior

to hadronization. We systematically discuss the NQ scaling at RHIC and find it holds in the intermediate p_T region, $2 < p_T < 5$ GeV/c, for all systems (Au+Au and Cu+Cu) and beam energies (62.4 GeV and 200 GeV). It suggests the deconfinement has been reached at RHIC.

We present the results of an elliptic flow analysis of Cu+Cu collisions at $\sqrt{s_{NN}} = 62.4$ and 200 GeV. Elliptic flow as a function of transverse momentum, $v_2(p_T)$, is reported for different collision centralities for charged hadrons $h^{\pm}$, and strangeness containing hadrons K^0_S, $\Lambda + \bar{\Lambda}$ and $\Xi^- + \overline{\Xi}^+$ in the midrapidity region $|\eta| < 1.0$. Significant reduction in systematic uncertainty of the measurement due to non-flow effects has been achieved by correlating particles at midrapidity, $|\eta| < 1.0$, with those at forward rapidity, $2.5 < |\eta| < 4.0$. We also present azimuthal correlations in p+p collisions at $\sqrt{s} =$ 200 GeV to help estimating non-flow effects. To study the system-size dependence of elliptic flow, we present a detailed comparison with the results from Au+Au collisions at $\sqrt{s_{NN}} =$ 200 GeV. We observe that $v_2(p_T)$ of strange hadrons has similar scaling properties as were first observed in Au+Au collisions, i.e.: (i) at low transverse momenta, $p_T < 2$ GeV/c, v_2 scales with transverse kinetic energy, $m_T - m$, and (ii) at intermediate p_T, $2 < p_T < 4$ GeV/c, it scales with the number of constituent quarks, n_q. Eccentricity scaled v_2 values, v_2/ε, are larger in more central collisions, suggesting stronger collective flow develops in more central collisions. The comparison with Au+Au collisions which go further in density shows v_2/ε depend on the system size, number of participants $N_{\rm part}$. This indicates that the ideal hydrodynamic limit is not reached in Cu+Cu collisions, presumably because the assumption of thermalization is not attained.

The comparison of the data to the ideal hydrodynamic calculations may shed light on the thermalization issue at RHIC. We find that ideal hydrodynamic calculations fail to reproduce the centrality dependence of $v_2(p_T)$ in both Au+Au and Cu+Cu collisions at $\sqrt{s_{NN}} = 200$ GeV collisions. To date, there are serval effects not included in the model, such as geometrical fluctuations in the initial conditions (particularly important in central collisions), finite viscosity effects. It remains to be seen if these effects can account for the difference between the models and data.

With a transport model, we study the $1/S\ dN/dy$ dependence of v_2/ε. The extracted

Knudsen numbers show finite values, even for central collisions. It indicates that the system has reached $0.46^{+0.24}_{-0.07}$ and $0.75^{+0.14}_{-0.10}$ of ideal hydrodynamic limits, using Glauber and Color Glass Condensate (CGC) initial condition, respectively. The lack of perfect equilibration allows for estimates of the effective parton cross section in the quark-gluon plasma and of the shear viscosity to entropy density.

With 3 k events collected using STAR detector from a test run of the collider in the year 2008, we present the results of an elliptic flow analysis of Au+Au collisions at $\sqrt{s_{NN}}$ = 9.2 GeV. Our results are consistent with the corresponding previous results from NA49 at similar $\sqrt{s_{NN}}$. It demonstrates the capabilities of the STAR detector to pursue the proposed beam energy scan. The beam energy dependence of NQ scaling in v_2 should be a powerful tool for searching for the possible QCD phase boundary.

Table of Contents

List of Figures

List of Tables

CHAPTER 1

Introduction

1.1 Quantum ChromoDynamics

1.1.1 Confinement and Asymptotic Freedom

Quantum ChromoDynamics (QCD) [Dks03a] is thought to be a correct theory of the strong nuclear force, one of the four fundamental forces of nature. It describes the strong interactions among quarks, which are regarded as fundamental constituents of matter, via their color quantum numbers. The strong interactions among quarks are mediated by a set of force particles known as gluons. Different from *Quantum ElectroDynamics* (QED) - the gauge theory describing electromagnetic interaction, QCD is based on the non-Abelian gauge group $SU(3)$, with gauge bosons (color octet gluons), and hence the gluons could have self-interacting. This results in a negative β-function and *asymptotic freedom* at high energies and strong interactions at low energies.

These strong interactions are confining: the self-coupled gluons strongly restrain the isolation of the quarks at large distance. There is no single quark as a color-triplet state observed experimentally. Only color-singlet bound states can propagate over macroscopic distances. The only stable color-singlets with size of the order of 1 fm are quark−antiquark pairs, mesons, and three-quark states, baryons. At high energy reactions, like deep inelastic scattering, the quark and gluon constituents of hadrons act as quasi-free particles, partons. Such reactions can be factorized into the convolution of non-perturbative parton distribution functions, which cannot be calculated from first principles directly. But with process-dependent functions (*i.e. hard processes involving large momentum transfers*), the reactions can be calculated as perturbative expansions

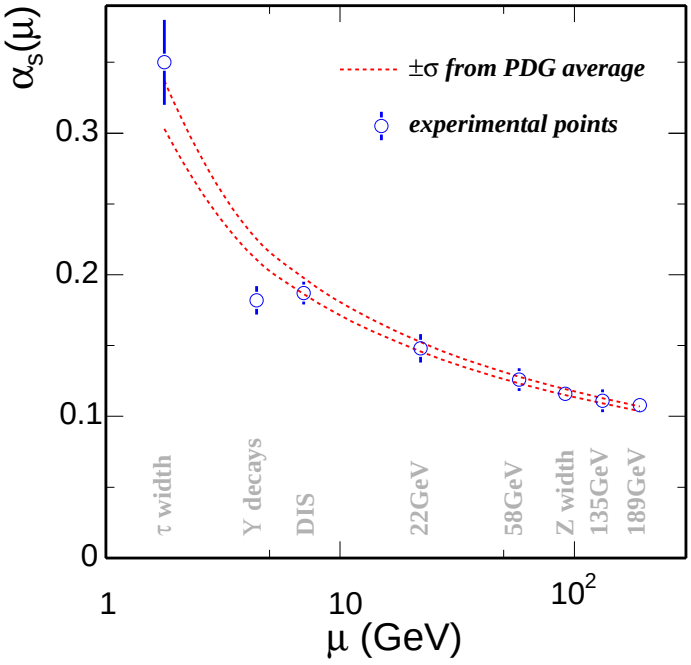

Figure 1.1: Measured QCD running coupling constant α_s from different experiments compared with Lattice QCD calculations.

in the coupling constant α_s.

In QED, the electrodynamic coupling constant $\alpha = \frac{1}{137}$. However, due to the gluons self-interactions, the renormalized QCD coupling shows renormalization scale (μ) dependence [Bet02a]. The running coupling $\alpha_s(\mu)$ can be written as:

$$\alpha_s(\mu) \equiv \frac{g_s^2(\mu)}{4\pi} \approx \frac{4\pi}{\beta_0 \ln(\mu^2/\Lambda^2_{\rm QCD})}, \tag{1.1}$$

where g_s, which is strong charge in the gauge group, is the only parameter in the QCD Lagrangian besides the quark masses. β_0 (>0) is the first coefficient of the β-function (renormalization neglects the higher orders). The strong force of the gluon-gluon self-coupling becomes smaller at shorter distance or with larger momentum transfers ($\alpha_s \to 0$ as $\mu \to \infty$), which is known as *asymptotic freedom*. In this case, QCD can be calculated perturbatively. Many experiments measured α_s at different scales. Since some of the precise measurements come from Z^0 decays, it has become universal to use $\alpha_s(M_z)$ as the label. The $\alpha_s(M_Z) = 0.1176 \pm 0.002$ [Pdg08a] comes from a fit to the experimental data, and the QCD scale $\Lambda_{QCD} \sim 200$ MeV. Fig. 1.1 shows the measured α_s at different momentum transfer scale μ compared with Lattice QCD calculations.

1.1.2 Deconfinement

Quarks are point-like and confined in the hadron by a binding potential $V_0(r)$, which increases with the quark separation r,

$$V_0(r) \sim \sigma r \tag{1.2}$$

where the string tension σ measures the energy per unit separation distance. Infinite amount of energy are needed to isolate a quark. It's impossible to split a hadron into isolated quarks. A deconfined quark is defined as the one that can move in a volume much larger than the volume of a nucleon (a hadron). We have never seen deconfined quarks in normal temperature and density.

The interaction of quarks in QCD is based on their intrinsic color charges. Confinement is a long-range feature of color charges. The long-range feature is also the nature of electric charges. In a extreme high density of color charges, color charges can be screened in the same way as electric charges known as Debye screening: the long-range interaction is shortened in dense medium of charges. At high density, the potential with the expected color screening [Sat00a] is given by

$$V(r) \sim \sigma r \left[\frac{1 - exp(-\mu r)}{\mu r}\right] \tag{1.3}$$

where μ is the color screening mass.

Figure 1.2 shows the potential as a function of r. When μ is equal to 0, the potential increases linearly with r. When μ is not equal to 0, the potential remains a finite constant as r increases. The resulting damping of the binding force removes all long range effects. Color screening occurs at sufficiently high density, so one can image a simple picture: hadrons made up of point-like quarks start to overlap, so each quark finds a large number of quarks in the vicinity of the volume size equal to intrinsic spatial extension of nucleons. It is no way to identify which quarks are the original constituents of a specific nucleon at some previous state of low density. Beyond a certain point, the concept of a hadron loses its meaning. So under color screening, the interactions between the quarks and gluons

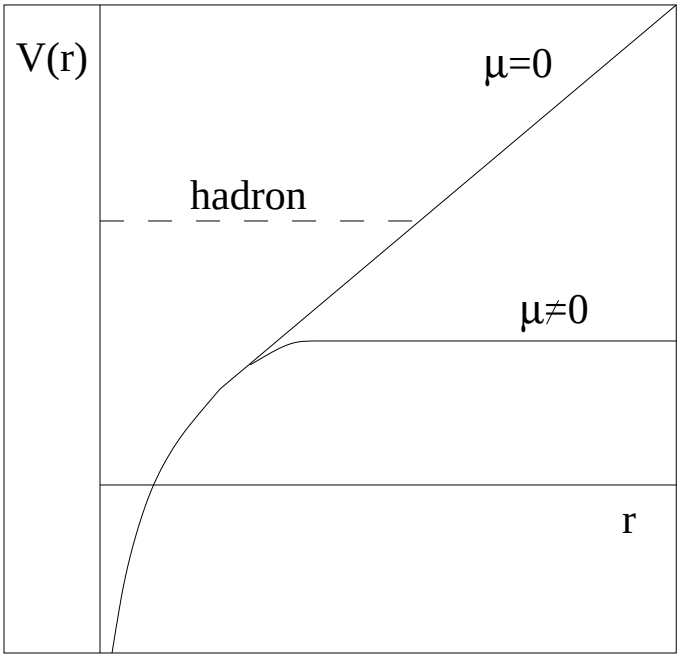

Figure 1.2: Color screening of confining potential. The calculations are from [Sat00a].

will be short-range. The color insulator is transformed to the color conductor, and the hadron matter is transformed to the Quark Gluon Plasma [Sat00a].

Recently, results from lattice QCD suggest that when sufficient high temperature is reached, quarks reveal effectively deconfined. The exposure of new (color) degrees of freedom should be manifested by a rapid increase in entropy density, hence in pressure, with increasing temperature. Figure 1.3 shows that above the critical temperature $T_c \sim 160$ MeV, the ratio of the pressure divided by T^4 (where T is the system temperature) rapidly rises. This sharp increase reveals a transition from a hadronic phase to a QGP phase, in which quarks and gluons are the relevant degrees of freedom. The arrows indicate the Stefan-Boltzman limits, where the deconfined quarks and gluons are non-interacting and massless. The deviation from the SB limit indicates remaining interactions among the quarks and gluons in the QGP phase.

1.2 Relativistic Heavy Ion Collisions

The main goal of building the Relativistic Heavy Ion Collider (RHIC) is to create bulk matter of deconfined quarks and gluons (Quark Gluon Plasma) and study its properties in

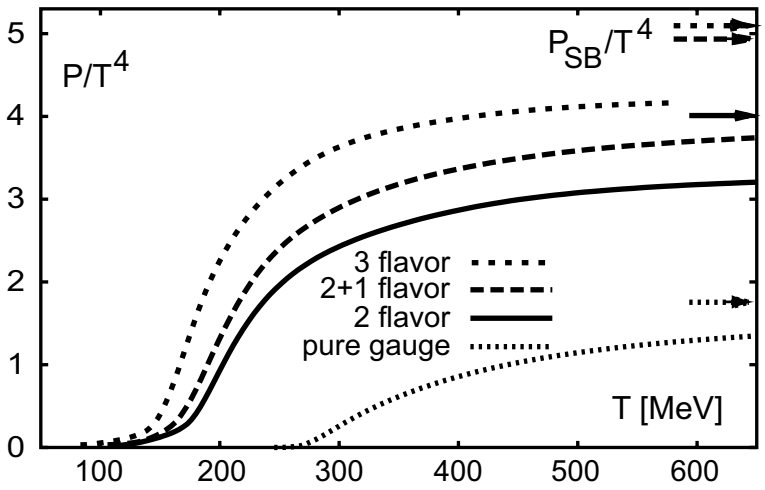

Figure 1.3: Pressure divided by T^4 as a function of T from LQCD calculation for several different choices of the number of quark flavors. The corresponding Stefan-Boltzmann pressure is indicated by the arrows near the right axis. LQCD calculation results from [Kar02a].

extreme high temperature and density. The new form of matter created in the laboratory is believed to exist at very early stage of universe evolution. Studying QGP formation will help us to understand the fundamental structure of the matter and evolution of our universe.

1.2.1 Collision Geometry

In relativistic heavy ion collisions, the geometry of the collisions can be defined by the participant spectator model. Figure 1.4 shows a schematic view of heavy ion collision between symmetric Lorentz contracted projectile and target nuclei in the center of mass frame. The impact parameter b is the distance between the center of nuclei and characterize the centrality of collision. The nucleons taking part in the primary collisions are called as participants and the rest that are not participated in the collisions are called as spectators. In most heavy ion experiments, the impact parameter is estimated by measuring the size of the participants and/or the spectators. The participants and the spectators are well separated experimentally because the spectator keeps it longitudinal velocity and mostly emitted in the forward (backward) rapidity, while the secondary particles from participants are peaked around mid-rapidity. Once the impact parameter

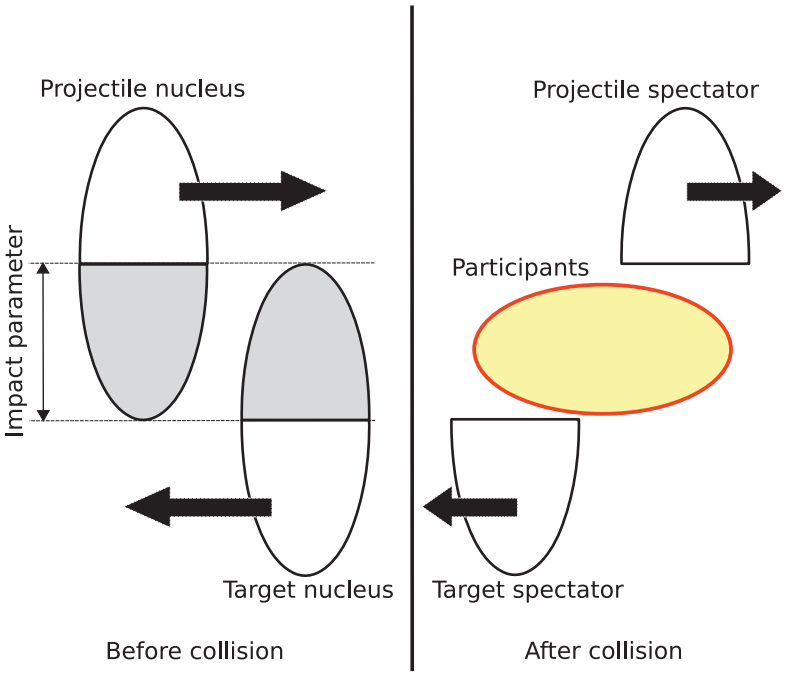

Figure 1.4: A schematic view of the geometry for a heavy ion collisions.

of the collision is determined, the Glauber Model [Mil07b] provides the number of participant nucleons (N_{part}), number of nucleon-nucleon collisions (N_{coll}), and the spatial eccentricity (ε) for a given impact parameter. These quantities can be calculated analytically or numerically under the following assumptions: a) Collisions of two nuclei are expressed in terms of the individual interactions of the constituent nucleons. b) At high energies, nucleons travels on straight line trajectories and are essentially undeflected. c) Inelastic nucleon-nucleon cross-section is independent of the number of collisions for a nucleon underwent before.

What is the relation between these quantities and the experimental observables? N_{part} is scaled with the volume of the interaction region, i.e., $N_{\mathrm{part}} \propto A$, where A is the mass number of nucleus, it is often assumed that the multiplicity dN/dy is proportional to N_{part}: $dN/dy \propto N_{\mathrm{part}} \propto A$. This relation can be obtained from the ideal hydrodynamics with (1+1)-dimensional expansion.

For processes involving large momentum transfer (hard scattering processes), all nucleon-nucleon collisions are assumed to be independent because of their small cross

sections. Therefore, the cross-sections for hard-scattering processes should scale with the number of binary nucleon-nucleon collisions.

Perfect liquid hydrodynamics suggest that initial anisotropy in the coordinate space are directly converted into the momentum anisotropy in the final momentum space. Since hydrodynamic model always assumes the local thermal equilibrium, the relation between initial spatial eccentricity and the final momentum anisotropy could provide the signal of possible thermalization in the early stage of heavy ion collisions.

1.2.2 Time Evolution

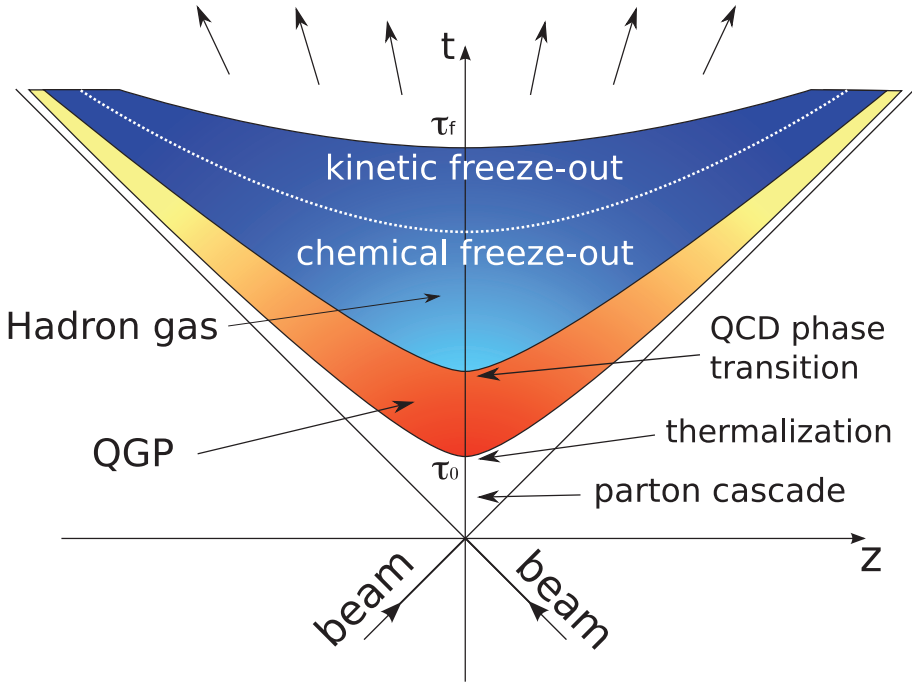

Figure 1.5: Space-time Evolution of a Heavy Ion Collision.

Fig. 1.4 shows a simplified space-time evolution of a heavy ion collision which consists of 4 stages; (i) a parton cascade stage, (ii) a QGP phase, (iii) an interacting hadron gas phase and (iv) a free hadron stage.

Parton cascade stage: $0 < \tau < \tau_0$

Several models are proposed to describe the dynamics of initial parton-parton scattering in heavy ion collisions: the color-string models [Mat87a], color glass conden-

sate [Mcl01a], and perturbative QCD models [Wan97a]. The parton production mechanism in parton cascade stage, however, is not well understood, and it is being actively studied both from theoretical and experimental point of view.

QGP phase and QCD phase transition: $\tau_0 < \tau < \tau_f$

The frequent scatterings of the partons leads to the local thermal equilibrim at τ_0. Once the local thermal equilibrium is attained, the relativistic hydrodynamics can be used to describe the evolution of the system. The hydrodynamic equation of motions [Kol03a] are given by:

$$\partial_\mu T^{\mu\nu} = 0, T^{\mu\nu}(x) = u^\mu u^\nu(\epsilon + P) - g^{\mu\nu}P \tag{1.4}$$

$$\partial_\mu j_i^\mu = 0, j_i^\mu(x) = n_i u^\mu \tag{1.5}$$

where ϵ, P and n_i are the proper energy density, pressure and density of charge i in local rest frame, and u_μ is the four velocity. $T^{\mu\nu}$ is the energy-momentum tensor, j^μ is the charge current density. The equation of motion is derived from the local conservation of energy and momentum $\partial_\mu T^{\mu\nu} = 0$ and local charge conservation $\partial_\mu j^\mu = 0$.

The essential assumption is the thermal and chemical equilibrium (locally) reached in the applied system. For heavy-ion collisions, due to the dense nature, the interactions between the constituents (partons or hadrons) should be strong and frequent. If the time of the interactions is long enough, the system will reach (local) equilibrium. The initial condition is prior to the reach of (local) equilibrium. At the late hadronic stage of system evolution, the interaction rates are small and can not sustain the (local) thermal equilibrium. So the hydrodynamics is only applicable in the middle possible QGP phase. The initial condition and hadronization need be modelled for a complete description of a collision. A sharp hadroniztion is modelled by the Cooper-Frye formula [Coo74a], which calculates the momentum distribution for hadrons created from the fluid elements on the freeze-out hyper-surface. Once modeling the hadronization is done, one can take advantage of the time evolution of hydrodynamics backward to estimate the initial conditions.

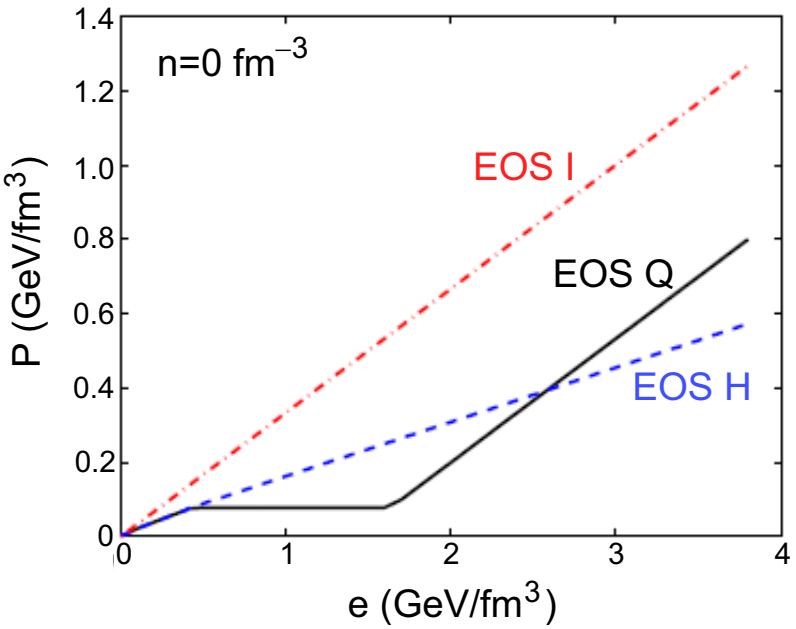

Figure 1.6: Pressure as a function of energy density at vanishing net baryon density for Equation-of-State of a Hagedorn resonance gas (EOS H), an ideal gas of massless partons (EOS I) and a connection of the two via a first-order transition at $T_c = 164$ MeV (EOS Q) [Kol03a].

With the equation of motion, the equation-of-state (EOS) need be modelled for calculation of the thermodynamic quantities of the system. Figure 1.6 shows the Equation of State from LQCD results. These EOS are used in hydrodynamic calculation in [Kol03a]. One example of EOS for a heavy ion collision is shown in solid line (EOS Q) connecting an ideal gas of massless partons at high temperature to a Hagdorn hadron resonance gas at low temperature via a first-order phase transition.

Freeze-out and free hadrons stage: $\tau_f < \tau$

The plasma expansion lead the drop of temperature, eventually hadronization takes place and relative number of species of the emitted particles is fixed at chemical freezeout temperature. The particles are rescattering each other until the hadronic interactions no longer occurred. Kinetic freeze-out happens if the kinetic equilibrium is no longer maintained, and no further hadronic interactions occur until the free streaming particles are detected. Only the hadrons from the free hadrons stage can be detected in the heavy ion experiments. It is very challenging to probe the early stage of the heavy ion collisions with hadrons measured in the finalstage.

1.3 Experimental Observations

To search for the QGP in experiment, it is critical to begin by defining clearly what QGP mean for experimental aspects. QGP is taken to be a (locally) thermalized state of matter in which quarks and gluons are deconfined, so that color degrees of freedom become manifest over the nuclear, rather than merely nucleonic , volumes [Ada05a]. The thermalization and deconfinement are the two experimental concentrations to claim QGP formation. In particular, thermalization is viewed as a necessary condition to be dealing with a state of matter. In this section, we review some experimental probes and results.

1.3.1 Hard Probe: Jet Quenching

The dynamical processes that produce the bulk medium also produce energetic particles through hard scattering processes. The interactions of these energetic particles with the medium provide a class of unique, penetrating probes. The hard partons (jets) will interact with the medium and thus suffer energy lose. The amount of the energy loss should reflect the gluon density of the medium. The softened partons fragmenting into hadrons will lead to the suppression of high p_T hadrons in the final state compared to that of no medium effects (p+p collisions). This effect is so called jet quenching [Wan92a, Wan98a, Wan05a]. For $p_T > 5$ GeV/c, the observed hadron spectra in Au+Au collisions at RHIC exhibit the power-law falloff in cross section with increasing p_T that is characteristic of perturbative QCD hard-scattering processes [Adl02a]. The nuclear modification factor is defined as

$$R_{AB}(p_T) = \frac{d^2N^{AA}/dp_T d\eta}{T_{AB} d^2\sigma^{pp}/dp_T d\eta} \tag{1.6}$$

where $d^2N^{AA}/dp_T d\eta$ is the differential yield in A+B collisions, $d^2\sigma^{pp}/dp_T d\eta$ is the measured differential cross section for p+p inelastic collisions. To compare two collisions, $T_{AB} = \langle N_{\rm bin}\rangle/\sigma^{pp}_{\rm inelastic}$, where $\langle N_{\rm Bin}\rangle$ is the mean number of binary nucleon-nucleon collisions, is introduced to account for the nuclear geometry. R_{AB} is equal to unit if A + B collision is a simple superposition of p+p collisions.

Left panel in Fig. 1.7 shows R_{AB} as a function of p_T for Au+Au and d+Au collisions. Large p_T hadrons in central Au+Au collisions are suppressed by a factor of 5 relative to naive binary scaling expectations. High p_T hadron suppression is not observed in d+Au collisions. This is an evidence that nuclear effects, such as nuclear shadowing of parton distribution functions and initial state multiple scattering can not account for the suppression. Further, the energy lose is expected to depend on the length of the path, which partons travel. The parton near the surface can penetrate the medium while the back-to-back produced parton will go through the significant length in dense matter and loose most of its energies into the medium thus can not be observed. Right panel in Fig. 1.7 shows the azimuthal distribution of hadrons with $p_T > 2$ GeV/c relative to a trigger

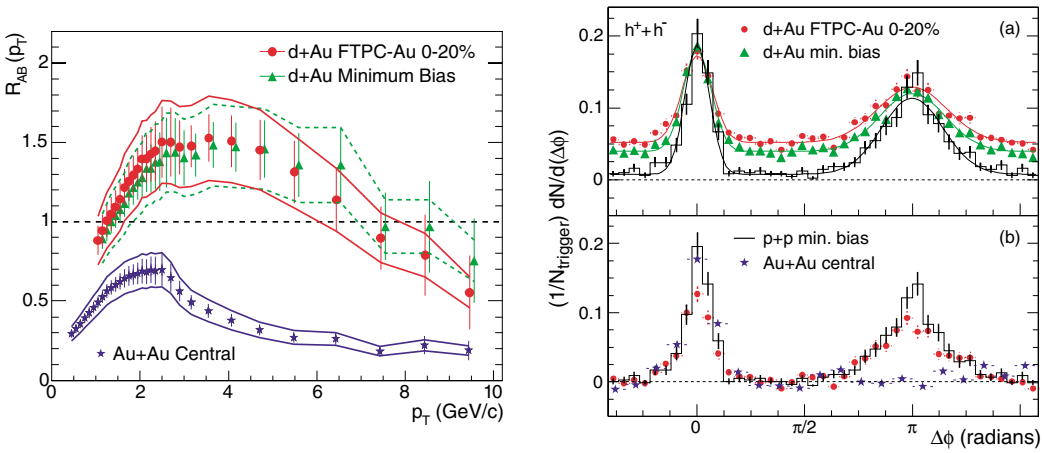

Figure 1.7: Left Panel: $R_{AB}(p_T)$ for minimum bias and central d+Au collisions, and central Au+Au collisions. The minimum bias d+Au collisions data are displaced 100 MeV/c to the right for clarity. The bands show the normalization uncertainties, which are highly correlated point-to-point and between the two d+Au distributions. The right Panel: (a) Efficiency corrected two-particle azimuthal distributions for minimum bias and central d+Au collisions, and for p+p collisions. (b) Comparison of two-particle azimuthal distributions for central d+Au collisions to those seen in p+p and Au+Au collisions. The respective pedestals have been subtracted. The figure is from [Ada03b]

hadron with $p_T^{\rm trig} > 4$ GeV/c. A hadron pair from a single jet will generate the near-side correlation ($\Delta\phi \approx 0$) as observed in p+p , d+Au and Au+Au collisions. A hadron pair from back-to-back di-jets will generate the away-side correlation ($\Delta\phi \approx \pi$) as observed in p+p and d+Au collisions. The significant disappearance of back-to-back correlation is observed in central Au+Au collisions. These results provide experimental evidence that the hot and dense medium has bee formed at RHIC.

1.3.2 Bulk Properties and Collective Dynamics

The properties of bulk matter created in collisions can be studied via multiplicities, yields, momentum spectra, especially at low p_T, where most of particles are produced. Due to the dynamical origin and evolution of the bulk matter, information on its degree of thermalization and its Equation of State related to the QGP formation are expected to be obtained.

1.3.2.1 Hadron Yield and Chemical Freeze-out

In heavy ion collisions, inelastic collisions cease at chemical freeze-out and the abundance of the chemical elements become fixed. The measured yields for different hadron species can provide information on the properties of the bulk matter at chemical freeze-out. Thermal model, assuming chemical and thermal equilibrium, is used to extract chemical freeze-out information such as chemical freeze-out temperature $T_{\rm ch}$, baryon chemical potential μ_B and strangeness suppression factor γ_s [Bra03a, Hwa03a, Hua88a].

Figure 1.8 shows p_T integrated particle yield ratios for various hadron species in central Au+Au collisions at $\sqrt{s_{NN}} = 200$ GeV measured by the STAR experiment. The thermal model fit to the data is shown by horizontal lines. From the fit, the chemical freeze-out temperature is 163 ± 4 MeV, and the baryon chemical potential is 24 ± 4 MeV. The thermal model fits well for stable and long-lived hadrons through multi-strange baryons. The deviations for the short-lived resonance yields, such as for Λ^* and K^* from the fits, presumably result from hadronic re-scatterings after chemical freeze-out. The inset in Fig. 1.8 shows the strangeness suppression factor γ_s [Xu02a]

as a function of number of participants. γ_s reflects how far a system is from chemical equilibrium. γ_s increases from 0.75 in peripheral Au+Au collisions to 0.99 in central Au+Au collisions. γ_s consistent with unity for central collisions strongly indicates that the chemical equilibrium has been reached in central collisions at RHIC.

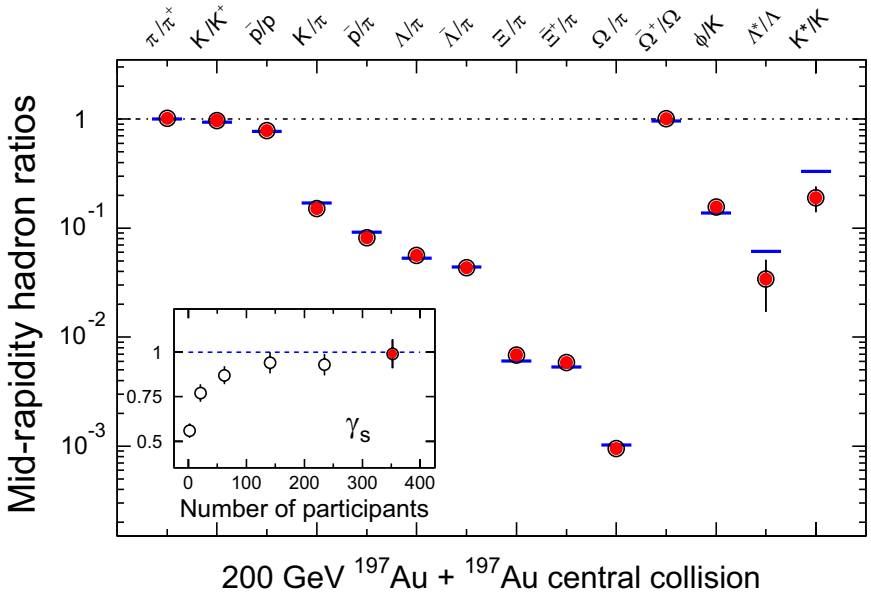

Figure 1.8: Ratios of p_T-integrated mid-rapidity yields for different hadron species for central Au+Au collisions at $\sqrt{s_{NN}}$ = 200 GeV measured by STAR. The horizontal bars represent thermal model fits to the measured yield ratios. The fit parameters are $T_{ch} = 163 \pm 4$ MeV, $\mu_B = 24 \pm 4$ MeV, $\gamma_s = 0.99 \pm 0.07$ [Bar04a]. The inset shows the variation of γ_s with number of participants, including the value (leftmost point) from fits to yield ratios for 200 GeV p+p collisions measured by STAR.

1.3.2.2 Spectra and Kinetic Freeze-out

The elastic collisions do not cease after chemical freeze-out until the kinetic or thermal freeze-out. The measurements of hadron transverse momentum spectra can provide information on the characteristics of the system at kinetic freezeout. In order to characterize the transverse expansion of the system, the hydrodynamics-motivated fit [Sch93a] to the spectra has been used to extract the random motion component and the collective motion component, which is respectively described by the fit parameter kinetic freeze-out temperature $T_{\rm fo}$ and radial flow collective velocity $\langle\beta_T\rangle$.

Figure 1.9 shows $T_{\rm fo}$ and $\langle\beta_T\rangle$ as a function of centrality from STAR experiment. For the copiously produced particles π, K and p, the extracted $T_{\rm fo}$ becomes smaller and smaller as the collisions appear more and more central, while the extracted $\langle\beta_T\rangle$ becomes larger and larger. This indicates that the system created in central collisions grows cooler and develops stronger flow than peripheral collisions. Compared to p+p collisions, most peripheral centrality bin has the similar $T_{\rm fo}$ but smaller $\langle\beta_T\rangle$. On the other hand, for most central collisions, the multi-strange particles ϕ and Ω appear to manifest a higher freeze-out temperature and lower radial flow velocity than π, K and p. Their freeze-out temperature is close to the chemical freeze-out temperature. ϕ and Ω are suggested to have small hadronic interactions with the expanding matter after chemical freeze-out [Ada04a, Bar04a, Bra95a, Bra99a, Bas99b]. If this is true, the radial flow velocity of ϕ and Ω have to be accumulative prior to the chemical freezeout, making them particularly sensitive to the early partonic stage in the system evolution.

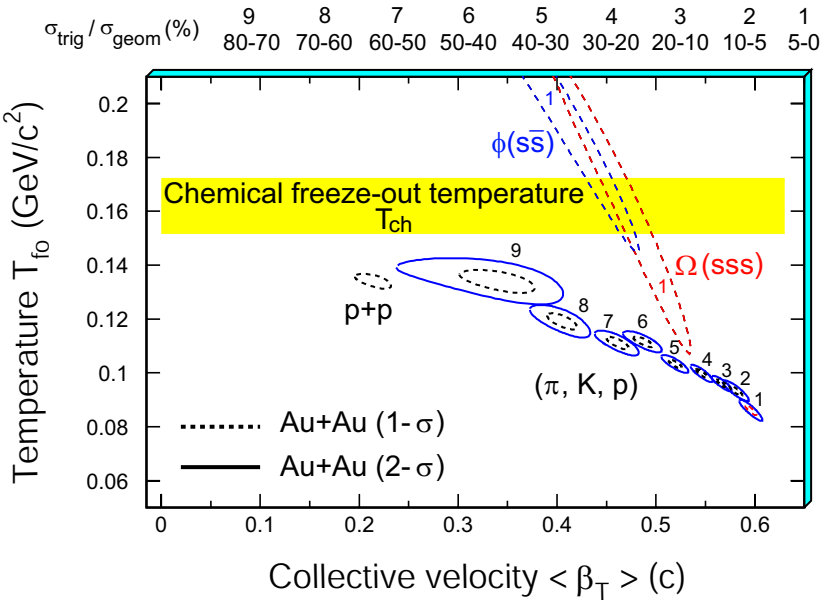

Figure 1.9: The χ^2 contours for T_{fo} and $\langle\beta_T\rangle$ extracted from thermal + radial flow fits to π, K, p together in 9 centrality bins from top 5% to 70%-80% for Au+Au collisions at $\sqrt{s_{NN}}$ = 200 GeV and for p+p collisions at $\sqrt{s_{NN}}$ = 200 GeV. The results for ϕ and Ω are shown only for most central Au+Au collisions at $\sqrt{s_{NN}}$ = 200 GeV. Dashed and solid lines are the 1σ and 2σ contours, respectively. The figure is from [Ada05a].

1.3.2.3 Collective Flow

The transverse momentum distribution of different particles reflects a random and collective component. The random component can be identified with the temperature of the system at kinetic freeze-out. Collective component has its origin of the matter density gradient from the center to the boundary of the fireball created in mid-rapidity. Interactions between constituents push the matter outwards: frequent interactions will lead to a common velocity distribution. Thus *Collective flow* is sensitive to the strength of interactions and degrees of freedom. Collectivity is defined as all particles moving with a common velocity.

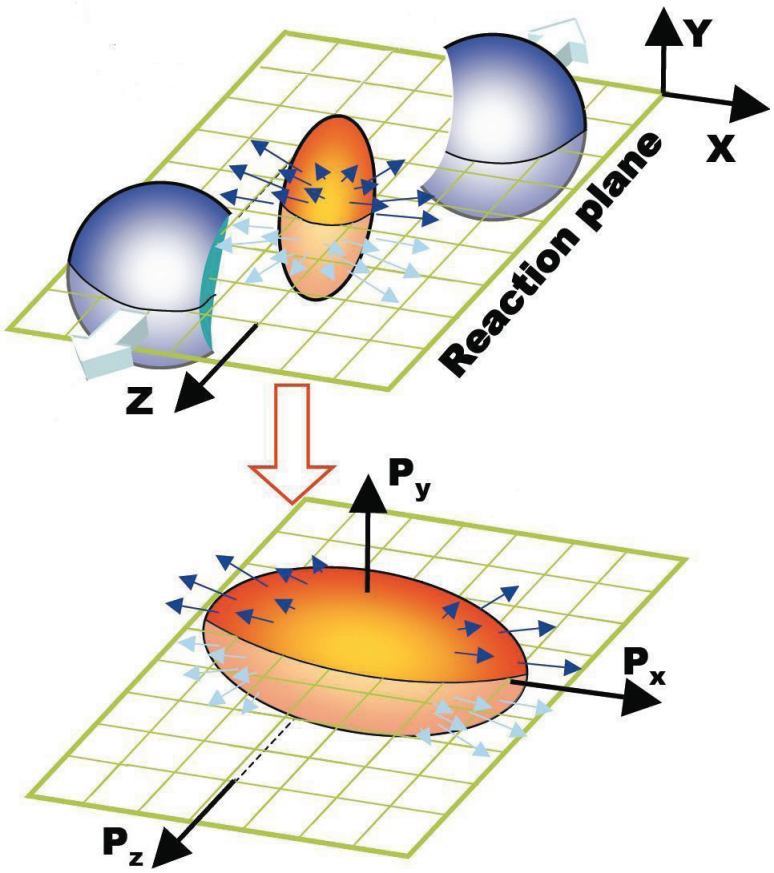

Figure 1.10: Azimuthal anisotropy in coordinate space and momentum space with respect to the reaction plane determined from the impact parameter and z (beam) directions.

The reaction plane is determined by the impact parameter and beam (z) directions.

The azimuthal anisotropy of transverse momentum distribution is well studied with respect to the reaction plane illustrated in Fig. 1.10. Since the initial spatial anisotropy has its almond shape with respect to the reaction plane, this almond shape of the initial profile is converted into a momentum asymmetry by the pressure gradient.

$$\frac{\partial \rho}{\partial x} \sim \Delta p_x$$

$$\frac{\partial \rho}{\partial y} \sim \Delta p_y$$

$$\langle p_x \rangle > \langle p_y \rangle$$

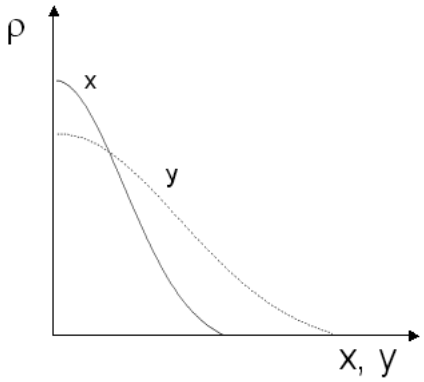

Figure 1.11: A sketch map of initial particle density in x and y direction.

In spatial coordinate, the length in x direction is shorter than that in y direction, shown on the top of Fig. 1.10. This results in larger density gradient in x direction than in y direction, which is shown in Fig. 1.11 with projection of all particles on one dimension (x or y direction). The area under the density variation curves in x direction and in y direction is the same, which is equal to total number of particles. Through frequent interactions among particles, the larger density gradient in x direction leads to the larger pressure gradient than in y direction. The larger pressure gradient further leads to larger collective flow velocity. The momentum space azimuthal anisotropy results from azimuthal anisotropy of collective flow velocity, which is shown at the bottom of Fig. 1.10. The initial spatial anisotropy will be washed out by the momentum space anisotropy during the system expansion, so this self-quenching effect makes anisotropic flow sensitive to the early stage [Sor97a].

Figure 1.12: Two components of hydrodynamic flow.

The term flow has two important aspects: (i) collectivity of produced hadrons and

(ii) the local thermalization among these hadrons, as shown in Fig. 1.12. As long as there are interactions among constituents, collectivity of the matter will be developed provided that the distribution of matter density is inhomogeneous. When the interactions last long enough the system will eventually approach local equilibrium and hence develops hydrodynamic type flow.

1.3.2.4 Elliptic Flow and Results

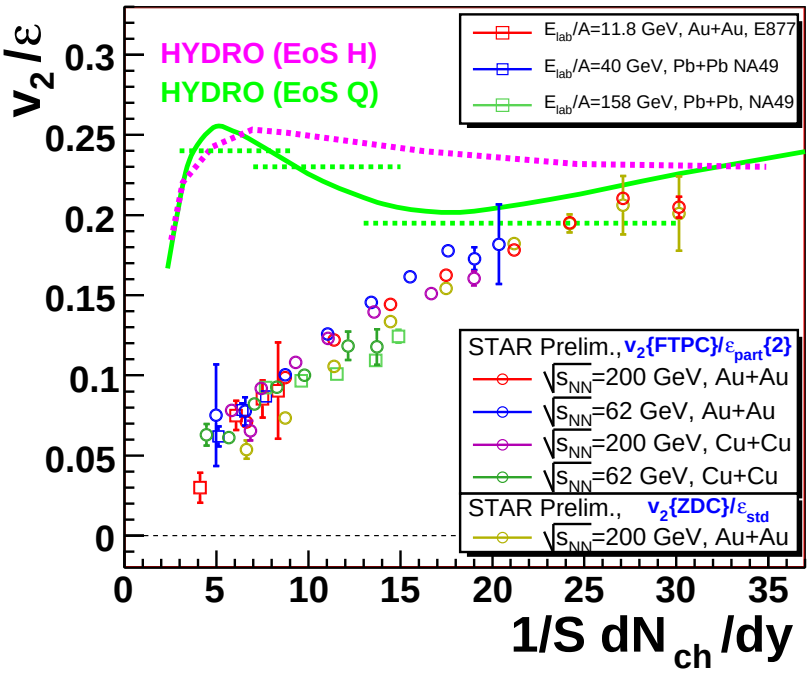

Figure 1.13: Charge particle v_2/ε versus $1/S\ dN_{\rm ch}/dy$ from AGS, SPS to RHIC energies. The figure is from [Vol07a].

In non-central Au+Au collisions, the initial spatial anisotropy in the reaction region is characterized by the eccentricity defined by:

$$\varepsilon = \frac{\langle y^2 - x^2 \rangle}{\langle y^2 + x^2 \rangle} \tag{1.7}$$

where x and y are the spatial coordinates in the plane perpendicular to the collision axis. The angle brackets $\langle\ \rangle$ denote an average weighted with the initial density.

The anisotropic flow can be studied by the Fourier expansion [Oll92a, Oll93a, Vol96a] of azimuthal angle distribution of produced particles with respect to the reaction plane:

$$E\frac{d^3N}{d^3p} = \frac{1}{2\pi}\frac{d^2N}{p_T dp_T dy}(1 + \sum_{n=1}^{\infty} 2v_n cos[n(\phi - \Psi_r)]) \tag{1.8}$$

where p_T and y are the transverse momentum and rapidity of a particle, ϕ is its azimuthal angle, v_n is the nth harmonic coefficient and Ψ_r is the azimuthal angle of the reaction plane. The different harmonic coefficients represent different aspects of the global flow behavior. v_1 is so called directed flow and v_2 is so called elliptic flow since it is the largest component characterizing the ellipse shape of the azimuthal anisotropy. Equivalently, v_2 can be calculated by:

$$v_2 = \langle\frac{p_x^2 - p_y^2}{p_x^2 + p_y^2}\rangle \tag{1.9}$$

The experimental evidence of the system reaching (local) thermalization is required to claim the QGP formation. Reference [Vol00a] suggests centrality dependence of elliptic flow can be related to whether the system has reached the thermal equilibrium or not. The argument is based on: 1. In the hydro limit, which complete thermalization is reached, the centrality dependence of elliptic flow is mostly defined by the eccentricity. 2. In the low density limit, where dynamical thermalization is not expected, elliptic flow is proportional to the eccentricity and the initial particle density.

Figure 1.13 shows charge particle v_2/ε as a function of $1/S\ dN_{\rm ch}/dy$, where S is the area of the overlapping zone, thus $1/S\ dN_{\rm ch}/dy$ is the measured particle density in mid-rapidity. At RHIC energies, STAR measurements are presented for Au+Au and Cu + Cu collisions at both 62.4 GeV and 200 GeV. At SPS energies, NA49 measurements are presented for Pb+Pb collisions at 40A GeV and 158A GeV. At AGS energies, E877 measurements is shown for Au+Au at 11.8A GeV. v_2/ε increases with $1/S\ dN_{\rm ch}/dy$. The particle density $1/S\ dN_{\rm ch}/dy$ defines the re-scattering probability among constituents. In more central collisions, there are more frequent interactions among constituents. This increase in v_2/ε indicates the system created in heavy ion collisions evolves towards the thermalization in central collisions.

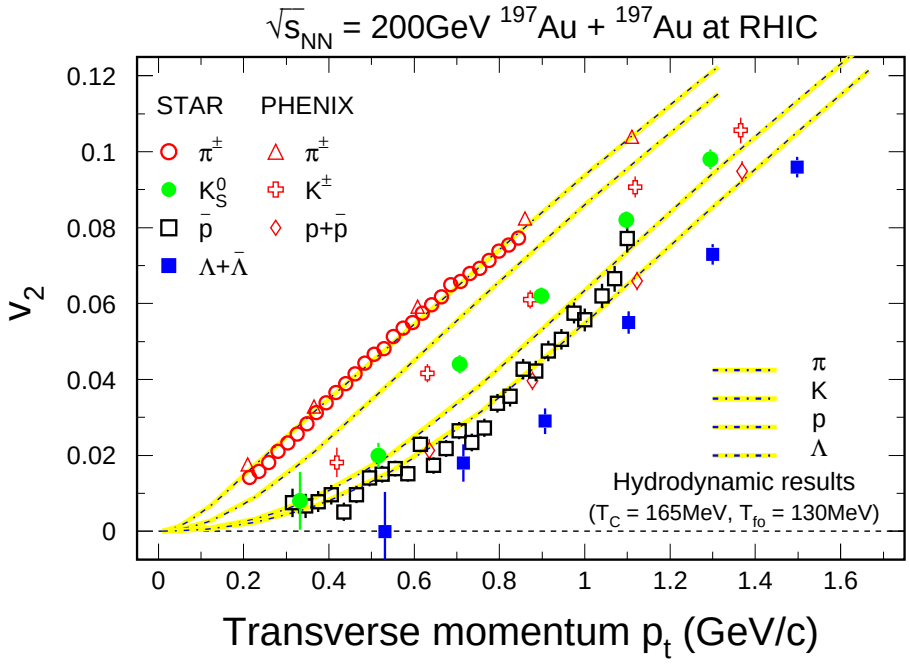

Figure 1.14: minimum bias $v_2(p_T)$ results from the STAR and PHENIX experiments for $\pi^{\pm}$, K^0_S, $\bar{p}$ $(p + \bar{p})$ and $\Lambda + \bar{\Lambda}$ up to 1.6 GeV/c. Hydrodynamics calculation [Huo01a, Huo03a] assuming early thermalization, ideal fluid expansion, an equation of state from LQCD calculation including a phase transition at $T_c = 165$ MeV and a sharp kinetic freeze-out with $T_{fo} = 130$ MeV (EOS Q in [Kol03a] and Fig. 1.6), are shown as dot-dashed lines. The figure is from [Old04a]

Figure 1.14 shows the measured low-p_T v_2 distribution from minimum bias in Au+Au collisions at $\sqrt{s_{NN}} = 200$ GeV from STAR and PHENIX experiments. Identified particle v_2 are shown for $\pi^{\pm}$, K^0_S, $\bar{p}$ $(p+\bar{p})$ and $\Lambda+\bar{\Lambda}$. Up to 1.6 GeV/c, at a given p_T, the heavier particle has the smaller v_2 than the lighter particle. This characteristic mass-ordering is predicted by the hydrodynamic calculation represented by the dot-dashed lines. This indicates the collectivity has been developed at RHIC. In this hydrodynamic calculation [Huo01a, Huo03a], the critical temperature is 165 MeV and the freeze-out temperature is 130 MeV. The absolute magnitude of v_2 is well produced as the parameters of the hydrodynamics calculations have been tuned to achieve good agreement with data. In particular, since the parameters are tuned for zero impact parameter while data is measured for minimum bias, the comparison for v_2 between the theory and the experiment should test hydrodynamical calculations as a function of centrality. This is especially a critical test in assessing QGP claims since the hydrodynamical calculations assume local thermalization while the system is most likely to reach thermalization in central collisions.

Figure 1.15 shows elliptic flow results at intermediate p_T for minimum bias in Au+Au collisions at $\sqrt{s_{NN}} = 200$ GeV. Panel (a) and (b) show v_2 as a function of p_T for K^0_S and $\Lambda+\bar{\Lambda}$ up to 6 GeV. Multi-strange baryon $\Xi^- + \overline{\Xi}^+$ and $\Omega+\bar{\Omega}$ are shown in (a) and (b), respectively. Hydrodynamics calculations [Huo01a] are indicated by dotted curves. At intermediate p_T, v_2 values deviate from hydrodynamic calculations and then saturate. Baryons saturate with higher v_2 value at higher p_T value than mesons. The dot-dashed curves in Fig. 1.15 (a) and (b) represent simple analytical function fits to K^0_S and $\Lambda+\bar{\Lambda}$ v_2. The saturated v_2 of K^0_S and $\Lambda+\bar{\Lambda}$ is independent on p_T up to 6 GeV with larger statistical uncertainties. The multi-strange baryon $\Xi^- + \overline{\Xi}^+$ and $\Omega+\bar{\Omega}$ are consistent with that of $\Lambda+\bar{\Lambda}$ within still sizable statistical uncertainties. Multi-strange baryons are suggested to have small hadronic cross section [Bar04a, Bra95a, Bra99a, Bas99b]. If this interpretation is correct, the development of their substantial v_2 must be accumulated at early partonic stage. Thus the multi-strange hadron v_2 indicates that partonic collectivity has been developed at RHIC.

Both v_2 and p_T scaled by the number of constituent quarks n_q are shown in Fig. 1.15

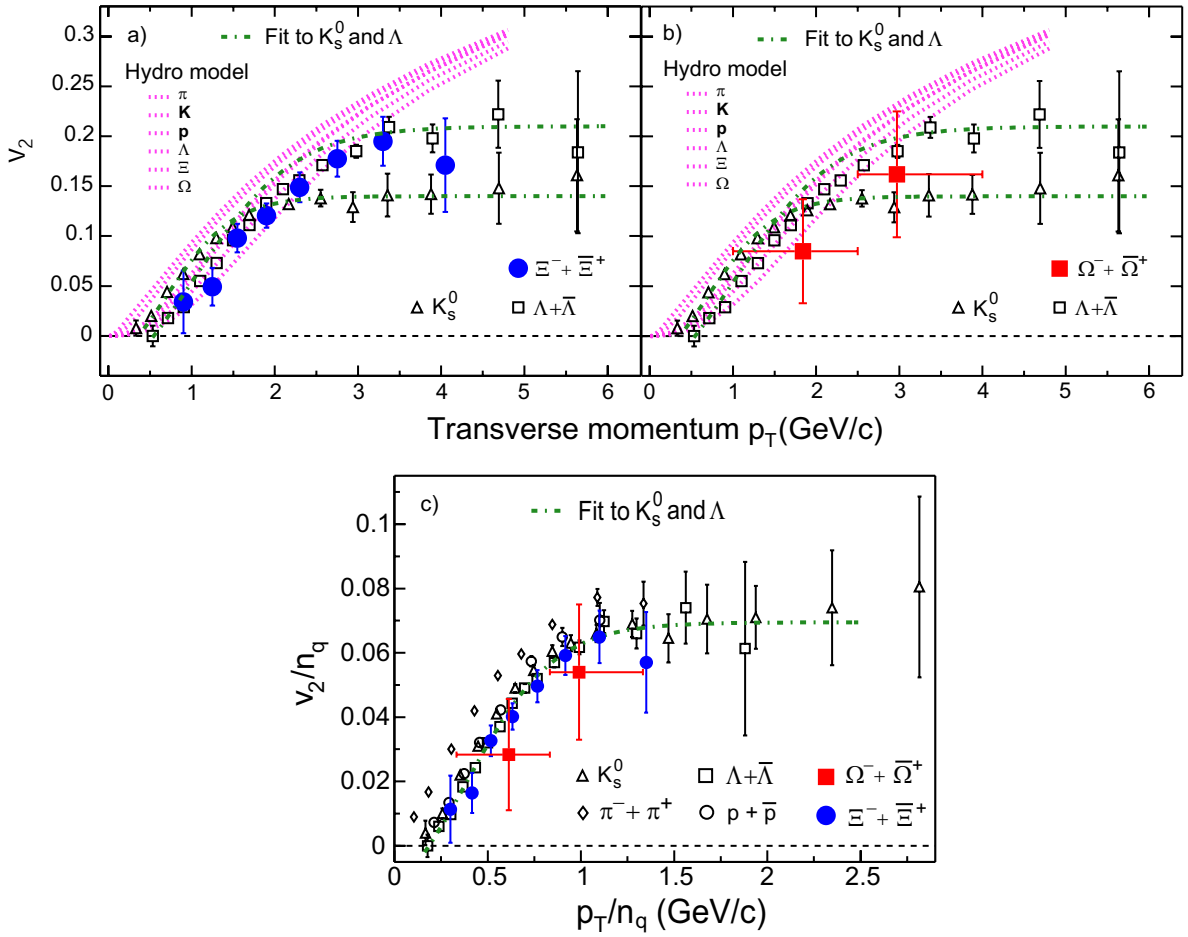

Figure 1.15: (a) and (b): transverse momentum dependence of elliptic flow for various hadron species in minimum bias Au+Au collisions at $\sqrt{s_{NN}} = 200$ GeV. STAR results [Ada04c] for K^0_S and $\Lambda+\bar{\Lambda}$ are shown in both panels, together with a simple analytic function fits (dot-dashed lines). STAR multi-strange baryon results for $\Xi^- + \bar{\Xi}^+$ and $\Omega + \bar{\Omega}$are shown in (a) and (b), respectively. Hydrodynamics calculations ar e indicated by dotted curves. (c): both v_2 and p_T scaled by the number of constituent quarks (n_q) in each hadron. Additionally, PHENIX results for π and $p+\bar{p}$ are shown together with STAR results in (a) and (b). The figure is from [Ada05a]

(c) for all particles in Fig. 1.15 (a) and (b), together with π and $p+\bar{p}$. For mesons, n_q is equal to 2 while for baryons, n_q is equal to 3. For $p_T/n_q > 1$ GeV/c, all particles follow a universal curve. This is so called Number of constituent Quark (NQ) scaling. This scaling itself seems to point to constituent quarks as the most effect degree of freedom in determining hadron flow at intermediate p_T. The data need to be improved in statistical precision and p_T extent for more identified mesons and baryons in order to establish this scaling more definitively.

Quark recombination/coalescence models [Fri03a, Gre03a, Lin02a, Vol02a] assume that the constituent quarks carry its v_2 by themselves, before they start to form hadrons. The hadron v_2 is developed by recombining constituent quarks into hadrons (i.e. hadronization). These models can roughly explain the NQ scaling. This suggests that the system has been in the deconfined state prior to hadronization.

1.4 Thesis Motivation

In this thesis, we will present the v_2 measurement of charged hadrons and strange hadrons in Au+Au and Cu+Cu collisions with different beam energies at RHIC-STAR experiment. Our main motivations and goals are as follows:

1. The previous results mainly focus on the v_2 measurement in Au+Au collisions. Since the conditions in Au+Au collisions might not hold in smaller systems and at lower beam energies, the system-size and beam-energy dependence of identified hadron v_2 will shed light on the systematic properties of partonic collectivity and quark degrees of freedom. Further, the study of v_2 in collisions of nuclei smaller than Au+Au will allow us to test the early thermalization hypothesis in Au+Au collisions. To date, there are only a few studies of identified hadron v_2 in Cu+Cu collisions. In this thesis, we present the results of v_2 for charged hadrons, K^0_S, $\Lambda + \bar{\Lambda}$ and $\Xi^- + \bar{\Xi}^+$ in Cu+Cu collisions at$\sqrt{s_{NN}} = 62.4$ and 200 GeV.

2. The Number of Quark scaling reflects constituent quark is the most effect degree of freedom in determining hadron flow at intermediate p_T. This suggests that the system

has been in the deconfined state prior to hadronization. We will discuss the partonic collectivity by testing the validity of the NQ scaling in collisions at RHIC and measuring the v_2 for multi-strange hadrons ϕ, $\Xi^- + \overline{\Xi}^+$ and $\Omega + \bar{\Omega}$.

3. The centrality and system size dependence of v_2 is related to the physics of the system created in high energy nuclear collisions. Since in the ideal hydrodynamic limit the centrality dependence of v_2 is mostly defined by the elliptic anisotropy of the overlapping region of the colliding nuclei, and in the low density limit by the product of the elliptic anisotropy and the multiplicity, it should be a good indicator of the degree of equilibration reached in the reaction. We will present a systematical study of centrality and system size dependence of v_2.

4. Theoretical analyses found that the centrality and system size dependence of v_2 can be described by a simple model based on eccentricity scaling and incomplete thermalization. Within these models the lack of perfect equilibration allows for estimates of the effective parton cross section in the quark-gluon plasma and of the viscosity to entropy density ratio (η/s) [Oll07a]. Thus, the v_2 results in this thesis should allow extrapolation to the ideal hydrodynamic limit and extraction of η/s.

The rest of the thesis is organized as following. Chapter 2 will review the facilities used to study heavy-ion collisions. The Relativistic Heavy Ion Collider (RHIC) and its programs will be discussed. The STAR detector system will be discussed in more details. Chapter 3 includes analysis methods. Techniques for measuring charged hadron and strange hadron v_2 and different flow methods will be discussed. Chapter 4 will present the results of this analysis. Chapter 5 will stimulate discussions on centrality dependence of v_2 measurements. Chapter 6 will give summary and outlook. In the following, we use $h^{\pm}$, Λ, Ξ and Ω to denote charged hadron, $\Lambda + \bar{\Lambda}$, $\Xi^- + \overline{\Xi}^+$ and $\Omega + \bar{\Omega}$, respectively.

CHAPTER 2

Experimental Setup

2.1 History of Heavy Ion Accelerator Facilities

The first facility to accelerate ion beams is BEVALAC made at Lawrence Berkeley National Laboratory, which accelerate ion beams energies up to 2 AGeV. It starts the study on relativistic heavy ion collisions. The high-energy physics researches have been driving the accelerator to higher energies. The Alternating Gradient Synchrotron (AGS) at the Brookhaven National Laboratory (BNL) provided gold beams up to an energy of 11.7 AGeV and allowed Au+Au collisions at center of mass energies per nucleon pair from $\sqrt{s_{NN}}$ = 2.68 GeV to $\sqrt{s_{NN}}$ = 4.75 GeV. The Super Proton Synchrotron (SPS) at CERN can accelerate lead ion beams up to an energy of 158 AGeV and lead-on-lead collisions up to $\sqrt{s_{NN}}$ = 17.3 GeV. A new accelerator is planned to be built at GSI. It is designed to accelerate Uranium beams up to an energy of about 20 AGeV.

The Relativistic Heavy-Ion Collider (RHIC) is a heavy-ion collider located and operated by the Brookhaven National Laboratory (BNL) in Upton, New York. RHIC is the first facility designed to collide the heavy-ion beams. The top energy at RHIC is $\sqrt{s_{NN}}$ = 200 GeV for gold beams and higher energy for lighter beams. The next large collider in development is the Large Hadron Collider (LHC) at CERN. It is originally designed for proton-on-proton collisions up to an energy of 14 TeV and lead-on-lead collisions up to $\sqrt{s_{NN}}$ = 5.5 TeV.

2.2 The Relativistic Heavy-Ion Collider

The RHIC collider consists of two quasi-circular concentric accelerator/storage rings on a common horizontal plane, one ("Blue Ring") for clockwise and the other ("Yellow Ring") for the counter-clockwise beams. Bending and focusing of ion beams are achieved by the ring super-conducting magnets. The counter-rotating beams can collide with one another at six location along their 3.8 km circumference. The two independent rings and two sources of ions make a various collisions possible, such as equal ion species from Au+Au to p+p , unequal ion species of protons on gold ions or light ions on gold. The basic design parameters of the collider are shown in Table 2.1. The top energy for heavy ion beams is 100 GeV/u. The operational momentum increases with the charge-to-mass ratio, resulting in the top energy of 125 GeV/u for lighter ion beams and 250 GeV/u for proton beams. The average luminosity for gold-on-gold collisions at $\sqrt{s_{NN}} = 200$ GeV is 8×10^{26} cm$^{-2}s^{-1}$ without electron cooling and 7×10^{27} cm$^{-2}s^{-1}$ with electron cooling. The average luminosity for proton-on-proton collisions at 250 GeV is 2.4×10^{32} cm$^{-2}s^{-1}$ without electron cooling and 8×10^{32} cm$^{-2}s^{-1}$ with electron cooling.

	Au+Au
Top beam energy	100 GeV/u
Nominal luminosity	1×10^{26} cm$^{-2}s^{-1}$
RHIC II luminosity	8×10^{26} cm$^{-2}s^{-1}$
Luminosity lifetime	10 hours
Number of bunches/ring	60

Table 2.1: RHIC performance parameters

The RHIC acceleration scenario is shown in Fig. 2.1. Three accelerators in the injector chain will successively boost the energy of ions, and strip electrons from the atoms. Negatively charge gold ions from the ion source at the Tandem Van de Graaff are partially stripped of their electrons with a foil, and then accelerated to the energy of 1 MeV/u by the seconde stage of the Tandem. After further stripping at the exit of the Tandem and a charge selection by bending magnets, beams of gold ions with the

charge state of +32e are delivered to the Booster Synchrotron and accelerated to 95 MeV/u. Ions are stripped again at the exit of the Booster Synchrotron to reach the charge state of +77e, and injected into the Alternating Gradient Synchrotron (AGS) for acceleration to the RHIC injection energy of 10.8 GeV/u. The beams are transferred to RHIC through the AGS-to-RHIC Beam Transfer Line. Gold ions are fully stripped to the charge state of +79e at the exit of the AGS. Finally, beams are accelerated to the top energy at RHIC.

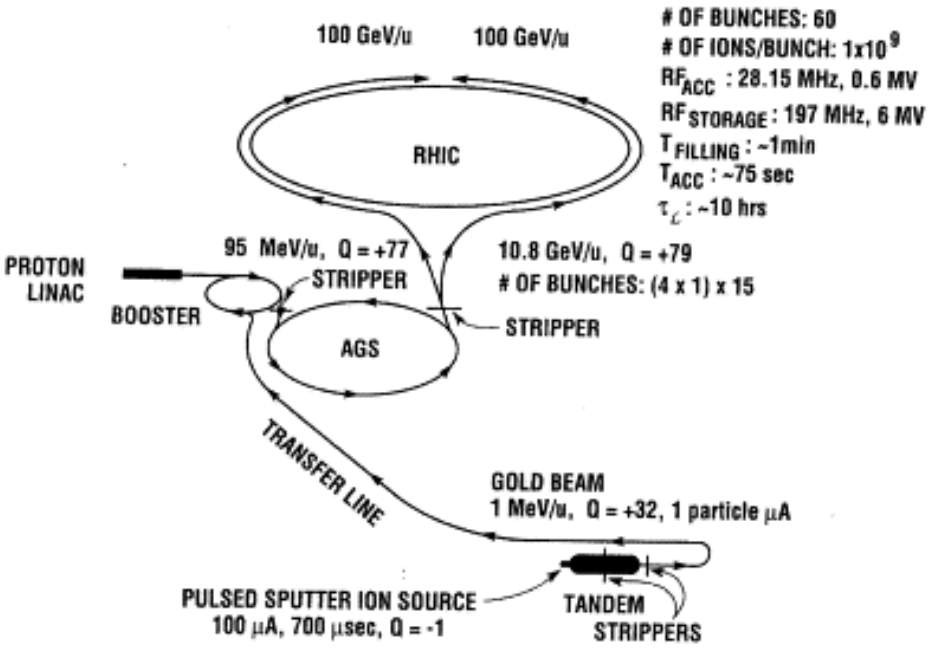

Figure 2.1: A diagram of the Relativistic Heavy-Ion collider complex at the Brookhaven National Laboratory including the facilities that accelerate the gold ions up to the RHIC injection energy.

Acceleration and storage of beam bunches at RHIC use two Radio Frequency (RF) system. One operating at 28 MHz is used to capture the AGS bunches and accelerate to the top energy. The other operating at 197 MHz is used to store the beam, which is transferred from the acceleration RF system. The storage RF system shorten the bunches and store the beam for 10 hours.

2.3 RHIC Experiments

There are four experimental programs at RHIC: STAR collaboration located at 6 o'clock position, PHENIX collaboration located at 8 o'clock position, PHOBOS collaboration located at 10 o'clock position, BRAHMS collaboration located at 2 o'clock position. Figure 2.2 shows the global view of STAR, PHENIX, PHOBOS and BRAHMS detectors.

STAR experiment [Ack03a] is designed to focus on global event reconstruction, resonance identification, event-by-event variables and fluctuations with full azimuthal acceptance. A large solenoidal tracking detector covers the full azimuthal angle $0 < \phi < 2\pi$. Subsystems include a main TPC covering $|\eta| < 1.3$, two forward TPCs covering $2.5 < |\eta| < 4$ and others such as, silicon vertex tracker, electromagnetic calorimeter, time of flight.

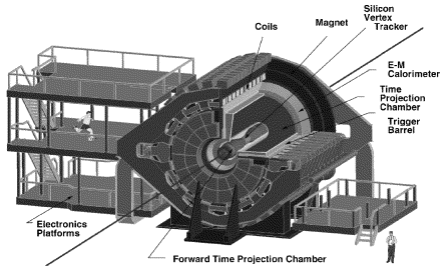

STAR detector

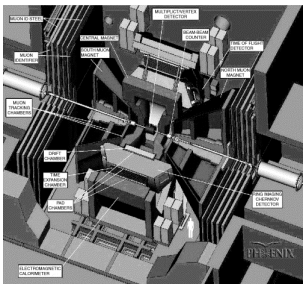

PHENIX detector

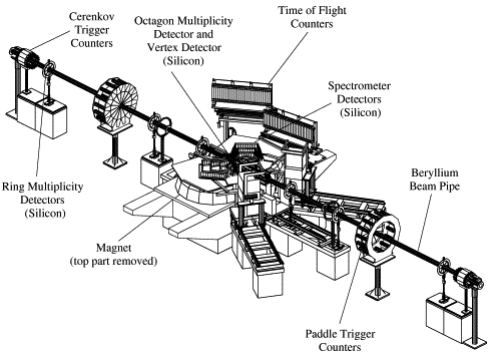

PHOBOS detector

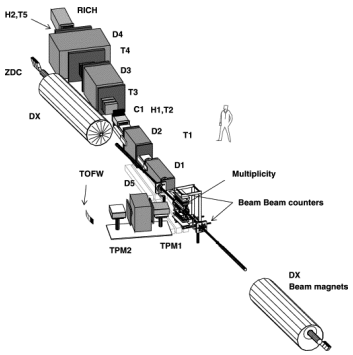

BRAHMS detector

Figure 2.2: Global view of STAR detector, PHENIX detector, PHOBOS detector and BRAHMS detector at RHIC.

PHENIX experiment [Adc03a] is designed to focus on rare probes, hadron identifica-

tion and electron identification with smaller acceptance and faster detectors. A central spectrometer with two arms and tracking sub-system, each subtends $\pi/2$ radians and covers $|\eta| < 0.35$. It is used to measure electrons, hadrons and photons at mid-rapidity. Two forward muon spectrometers covers $1.1 < |\eta| < 2.4$ and azimuthal angle $0 < \phi < 2\pi$. They are used to measure muons at forward rapidity.

BRAHMS experiment [Ada03a] is designed to measure charge hadrons over the widest possible range of rapidity and transverse momentum ($0 < y < 4$, $0.2 < p_T < 3.0\ GeV/c$) with two small solid-angle spectrometers.

PHOBOS experiment [Bac03a] is designed to detect charge particles over the full solid angle using a multiplicity detector and measure identified charge particles near mid-rapidity in two spectrometers arms.

2.4 STAR Detector Systems

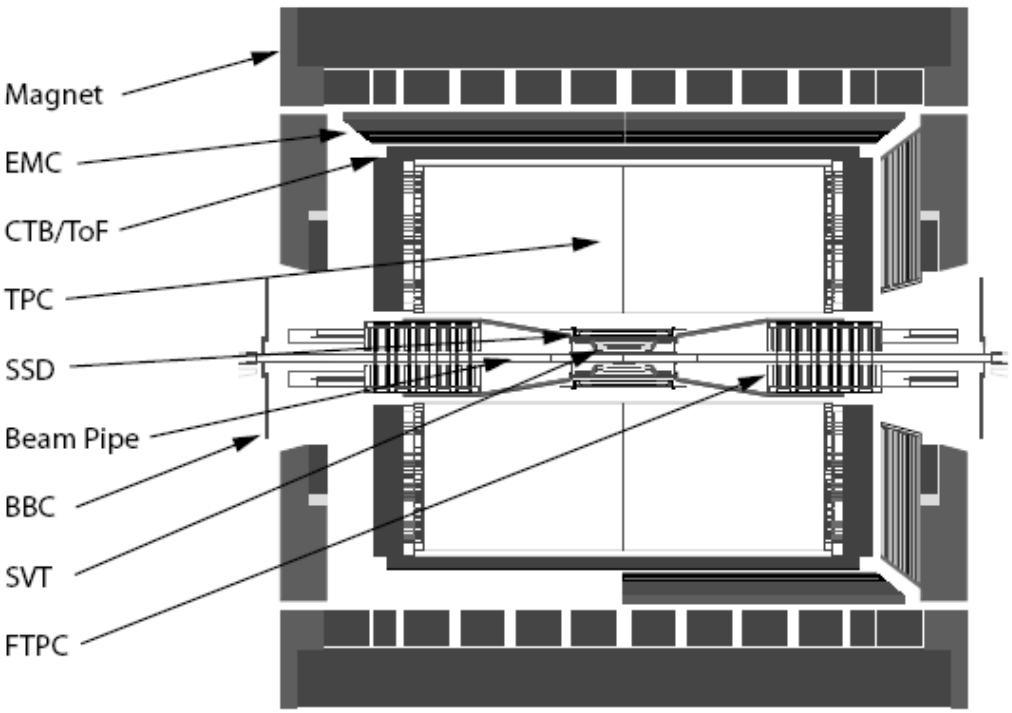

Figure 2.3: Cutaway side view of the STAR detector as configured in 2004

To search for signatures of Quark Gluon Plasma (QGP), the Solenoidal Tracker At RHIC (STAR) was constructed for measurements of hadron production over a large solid angle with high precision momentum. It is particularly suitable to measure event-by-event fluctuations, correlations and jets. Particle identification provides the possibility to study those observables for different particle species and identified particle spectra.

A cutaway side view of the STAR detector as configured for the RHIC 2004 run is displayed in Figure 2.3. The STAR detector consists of several subsystems, which integrate to the whole functionality of the detector. The STAR detector sits in a large solenoidal magnet with an uniform magnitude 0.25 or 0.5 Tesla [Ber03a]. The beam is surrounded by the beam pipe [Mat03a]. Its material, Berillium with low density and low nuclear charge is chosen to minimize the number of photon conversions and multiple scattering of particles traversing the beam pipe. The main tracking detector in STAR is the Time Projection Chamber (TPC) [And03a], which provide symmetric tracking information with coverage $|\eta| < 1.8$. To extend the tracking to the forward region, a radial-drift TPC (FTPC) [Ack03b] is installed covering $2.5 < |\eta| < 4$ with complete azimuthal coverage and symmetry. The Silicon Vertex Tracker (SVT) [Bel03a] supplements tracking information provided by the TPC for precise location of primary vertex and secondary vertex of the weak decay that move from the primary vertex before decaying into charge particles. The Silicon Strip Detector (SSD) [Arn03a] complete the intermediate trackers and improve the extrapolation of TPC tracks trough SVT hits with good hit position resolution. A full-barrel electromagnetic calorimeter (EMC) and the end-cap calorimeter located on the west side [Bed03a, All03a], provide capability of photon and electron identification. Measurements of the spatial distribution of photons within $2.5 < \eta < 3.5$ is also provided by the Photon Multiplicity Detector (PMD) [Agg03a]. Time-of-Flight based on Multi-gap Resistive Plate Chamber (TOFr) [Bon03a] extends TPC capability of particle identification. It covers $-1 < \eta < 1$ and 2π in azimuth.

The STAR trigger system [Bei03a] is based on input from fast detectors to control the event selection for the much slower tracking detectors. The Central Trigger Barrel (CTB) at $|\eta| < 1$ and Zero Degree Calorimeters (ZDC) located in the forward direction

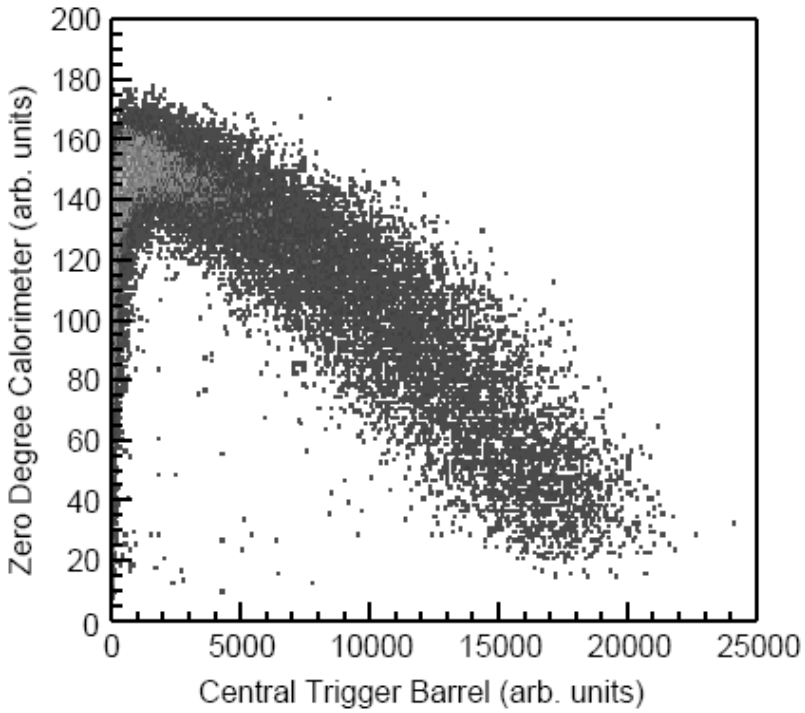

Figure 2.4: Correlation between the summed pulse heights from the ZDC and the CTB for events with a primary collision vertex reconstructed from tracks in the TPC.

at $\theta < 2$ mrad, provide input to the trigger system. The CTB surrounds the outer cylinder of the TPC, and determines the flux of charge particles in the mid-rapidity region. The ZDCs determining the energy in neutral particles remaining in the forward direction. The correlations between ZDC pulse height and that of the CTB shown in Figure 2.4 is a monotonic function, which is used to in experiment to provide a trigger for centrality of the collision. Peripheral collisions characteristically leave a large amount of energy in forward direction into the ZDC and a small amount of energy and particles sideward into the CTB. Central collisions leave less energy into ZDC and more energy and particles into the CTB. The largest number of events occurs for large ZDC values and small CTB values, which is corresponding to the peripheral collisions. A minimum bias trigger require at least one neutron in each of the forward ZDCs, which corresponds to 95% of the geometrical cross-section. Central triggers further require less energy in ZDCs and sufficient CTB signals to reduce the second branch at low CTB values shown in Figure 2.4.

Future upgrades of STAR detectors are under development to expand the detection

capabilities and physics program. TOF upgrade has been finished successfully in 2009. It will provide full azimuthal coverage and two units in pseudo-rapidity $-1.0 < \eta < 1.0$. This allows STAR to extend capability of particle identification over full acceptance and TPC pseudo-rapidity coverage. It will benefit detailed and precise measurement of observables such as correlations and fluctuations. Heavy Flavor Tracker (HFT) [Wie06a] is proposed to extend STAR's capability to measure displaced vertices very close to the primary vertex, namely direct reconstruction of open charm states such as D meson. Measurement of D meson v_2 will gain information on the thermalization among u, d, s quarks. Measurement of D meson R_{AA} will test heavy flavor energy loss.

2.5 STAR Time Projection Chamber

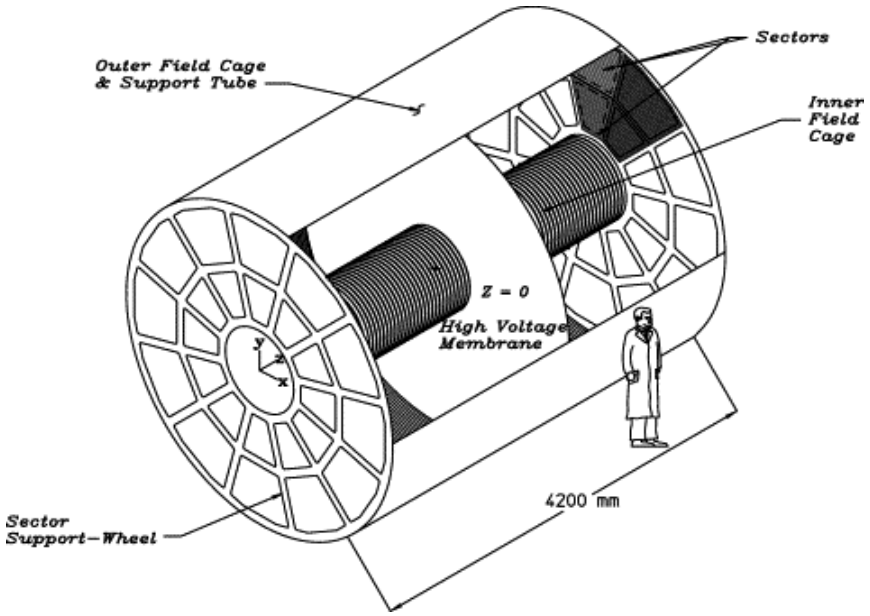

Figure 2.5: Perspective view of the STAR TPC.

The STAR TPC is shown schematically in Figure 2.5. The TPC is the primary detector element of the STAR detector. A large volume Time Projection Chamber (TPC) [Tho02a] for charge particle tracking and particle identification is located at a radial distance from 50 to 200 cm from the beam axis. The TPC is 4 m long and it covers a pseudo-rapidity range $|\eta| < 1.8$ for tracking with complete azimuthal symmetry

$(0 < \phi < 2\pi)$ providing the equivalent of 70 million voxels via 136,608 channels of front-end electronics (FEE). The TPC records the tracks of particles, measures their momenta, and identifies particles by measuring their ionization energy loss (dE/dx). Particles are identified over a momentum range from 100 MeV/c to greater than 1 GeV/c, and momenta are measured over a range of 100 MeV/c to 30 GeV/c.

The TPC sits in a large solenoidal magnet that operates at 0.5 T [Ber03a]. It is an empty volume of gas in a well-defined, uniform, electric field of $\sim$ 135 V/cm. The paths of primary ionizing particles passing through the gas volume are reconstructed with high precision from the released secondary electrons which drift to the readout end caps at the end of the chamber. The uniform electric field which is required to drift the electrons is defined by a thin conductive Central Membrane (CM) at the center of the TPC, concentric field-cage cylinders and the readout end caps. Electric field uniformity is critical since track reconstruction precision is sub-millimeter and electron drift paths are up to 2.1 m.

The readout system is based on Multi-Wire Proportional Chambers (MWPC). The drifting electrons avalanche in the high fields at the 20 μm anode wires providing an amplification of 1000-3000. Diffusion of the drifting electrons and their limited number defines the position resolution. Ionization fluctuations and finite track length limit the dE/dx particle identification.

2.5.1 Sub-structures

The uniform electric field in the TPC is defined by establishing the correct boundary conditions with the parallel disks of the CM, the end caps, and the concentric field cage cylinders. The central membrane is located at the center of TPC and is operated at high voltage 28 kV. The Inner Field Cage (IFC) and Outer Field Cage (OFC) insure that the electric field uniformity is high. The field cage cylinders provide a series of equi-potential rings that divide the space between the central membrane and the anode planes into 182 equally spaced segments. One ring at the center is common to both ends. The central membrane is attached to this ring. The end caps as a whole are at ground.

2.5.1.1 Central Membrane

The CM is made from a number of pie-shaped, carbon-loaded kapton file sections, each of which is 70 μm thick. An outer hoop, which is mounted in the OFC, supports and keeps the CM secured under tension. There is no mechanical coupling to the IFC, other than a single electrical connection. This design minimizes material and maintains a good flat surface to within 0.5 mm. Thirty six aluminum stripes have been attached to each side of the CM to provide a low work function as the target for the TPC laser calibration system [Abe03a, Leb02a]. Electrons are photo-ejected when ultraviolet laser photons hit the stripes, and since the position of the narrow stripes are precisely measured, the ejected electrons can be used for spatial calibration.

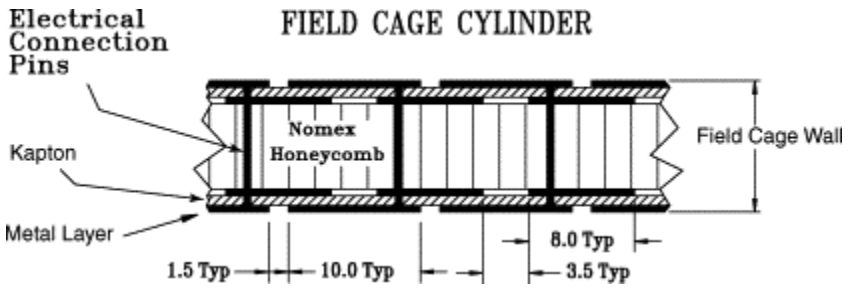

Figure 2.6: An example of IFC construction and composition of the cylinder wall.

2.5.1.2 Field Cage

The field cage cylinders serve the dual purpose of both gas containment and electric field definition. The mechanical design was optimized to reduce mass, minimize track distortions from multiple Coulomb scattering, and reduce background from secondary particle production. As the particles make their way from the collision vertex, through the IFC, and eventually to the active detector region of the TPC, the corruption of their kinematic information is kept to a minimum. Mechanically, the walls of the low mass self-supporting cylinders are effectively a bonded sandwich of two metal layers separated by NOMEX honeycomb (see Figure 2.6 for a cutaway view). Punch-through pins were used to electrically connect the layers on the two sides of the sandwich. The metal layer, which consists of kapton with metal on both sides, is etched to form electrically

separated 10 mm strips separated by 1.5 mm. The 1.5 mm break is held to the minimum required to maintain the required voltage difference between rings safely in order to limit the dielectric exposure in the drift volume thus reducing stray, distorting electric fields. The metal layer, is etched into stripes so that, after rolling the whole assembly into a cylinder, the stripes become rings around the cylinder. The sandwich structure of the OFC cylinder wall is 10 mm thick while the IFC has a wall thickness of 12.9 mm. Nitrogen gas or air insulation was used to electrically isolate the field cage from surrounding ground structures. This design choice requires more space than solid insulators, but it has two significant advantages. One advantage is to reduce multiple scattering and secondary particle production. The second advantage is the insulator is not vulnerable to permanent damage. The IFC gas insulation is air and it is 40 cm thick without any detectors inside the IFC. The OFC has a nitrogen layer 5.7 cm thick isolating it from the outer shell of the TPC structure. The field cage surfaces facing the gas insulators are the same as the surfaces facing the TPC drift volume. This design avoids uncontrolled dielectric surfaces, which can distort the electric field. The outermost shell of the TPC is a structure that is a sandwich of material with two aluminum skins separated by an aluminum honeycomb. The skins are a multi-layer wraps of aluminum. The innermost layer, facing the OFC, is electrically isolated from the rest of the structure.

2.5.1.3 End Caps

The end-cap readout planes of STAR is similar to the designs used in other TPCs but adjusted to accommodate the high track density at RHIC. The readout planes, MWPC chambers with pad readout, are modular units mounted on aluminum support wheels. The readout modules, or sectors, are arranged as on a clock with 12 sectors around the circle. Only 3 mm spaces between the sectors is to reduce the dead area between the chambers. Each sector is divided into two sub-sectors. An inner radius sector and an outer radius sector (see Figure 2.7). The construction and maintenance of the sectors is greatly simplified by their modular nature and their manageable size. As illustrated in Figure 2.8, the MWPC chambers consists of four elements, a pad plane and three wire planes. The anode wire plane, with wires of 20 μm in thickness, along with the

pad plane on one side and the ground wire on the other side, comprise the amplification layer. The anode wires are biased on a high voltage to provide the necessary electric field to avalanche the electrons from the track ionization.

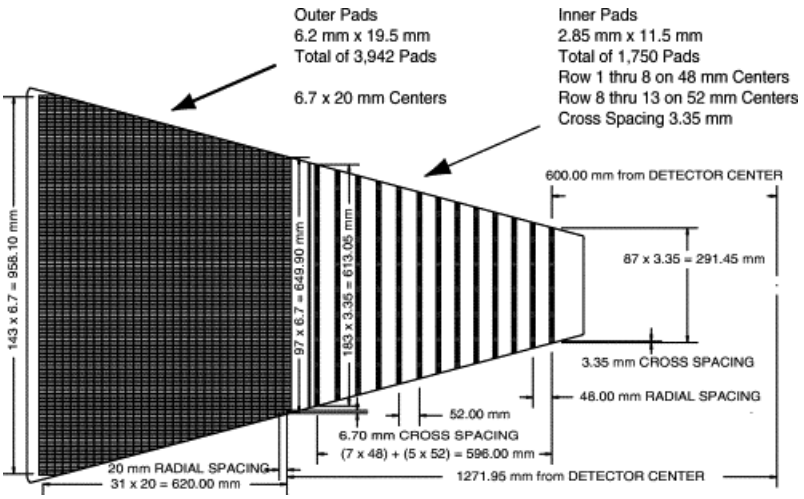

Figure 2.7: Full sector pad plane of TPC end caps. The inner sub-sector is shown on the right and the outer sub-sector is shown on the left.

The gating grid is the third wire plane and its purpose is to establish the boundary conditions defining the electric field in the TPC drift volume at the ends of the TPC. The gating grid also functions as a gate to control the passage of electrons from the active volume of the TPC into the MWPC. The gating grid allows drift electrons to pass through to the MWPC only while an event is being recorded. Otherwise, it is electrostatically opaque to electrons. More importantly, it also prevents ions produced in the MWPC from entering the active TPC volume. The drift velocity of ions is much slower than electrons, so they are too slow to move into the active TPC volume while the gating grid is "open". Furthermore, ions produced in the MWPC are drifted to cathode and gating grid electrodes while the gating grid is "closed".

2.5.1.4 TPC Material

The design emphasis was to limit material at the inner radius where multiple coulomb scattering is most important for accurate tracking and accurate momentum reconstruction. For this reason, aluminum was used in the IFC, limiting it to only 0.5% radiation

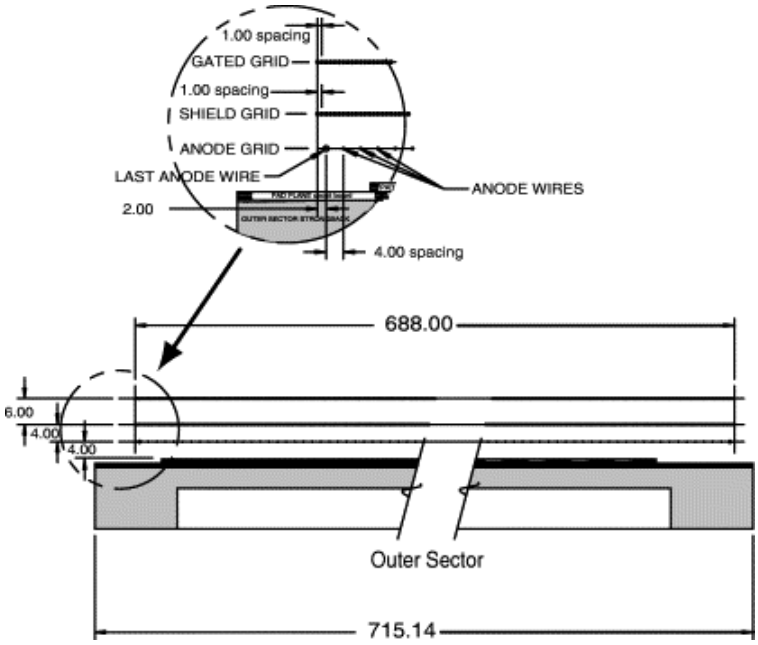

Figure 2.8: Outer sub-sector wire geometry of TPC end-caps.

length (X_0) and copper was used for the OFC, limiting it to 1.3% X_0.

CHAPTER 3

Analysis Method

In this chapter, we present the selection criteria for events and tracks, reconstruction of K^0_S, Λ, Ξ and Ω, event plane determination, the analysis methods for v_2 measurement, and systematic uncertainties on v_2.

3.1 Event and Track Selection

The data set used in this thesis consists of, minimum bias events for Cu+Cu collisions at $\sqrt{s_{NN}}$ = 200 GeV and 62.4 GeV taken during run V and minimum bias Au+Au events at $\sqrt{s_{NN}}$ = 200 GeV and 9.2 GeV taken during run VII.

Trigger Setup Name	Production	Vertex Cut	Trigger ID	Events No.
cuProductionMinBias	P06ib	$\|V_z\| < 30$ cm	66007	28 M
cuProductionHighTower	P06ib	$\|V_z\| < 30$ cm	66007	10 M

Table 3.1: Run V trigger and events selection in minimum bias Cu+Cu collisions at $\sqrt{s_{NN}}$ = 200 GeV.

Trigger Setup Name	Production	Vertex Cut	Trigger ID	Events No.
cu62ProductionMinBias	P05id	$\|V_z\| < 30$ cm	76007, 76011	17 M

Table 3.2: Run V trigger and events selection in minimum bias Cu+Cu collisions at $\sqrt{s_{NN}}$ = 62.4 GeV.

The trigger and event selection are summarized in Table 3.1-3.4. Events with the z position of vertex (V_z) further than 30 cm (75 cm for 9.2 GeV Au+Au dateset) from the main TPC center were discarded. Events useful for our analysis are listed in the

Trigger Setup Name	Production	Vertex Cut	Trigger ID	Events No.
ProductionMinBias	P08ic	$\|V_z\| < 30$ cm	200001, 200003, 200013	55 M
Production2	P08ic	$\|V_z\| < 30$ cm	200001, 200003, 200013	11 M

Table 3.3: Run VII trigger and events selection in minimum bias Au+Au collisions at $\sqrt{s_{NN}}$ = 200 GeV.

Trigger Setup Name	Production	Vertex Cut	Trigger ID	Events No.
ProductionMinBias	P08ic	$\|V_z\| < 75$ cm	minimum bias	3 k

Table 3.4: Run VII trigger and events selection in minimum bias Au+Au collisions at $\sqrt{s_{NN}}$ = 9.2 GeV.

most right column. The total number of minimum bias events is 38 million for 200 GeV Cu+Cu data set, 17 million for 62.4 GeV Cu+Cu data set, 66 million for 200 GeV Au+Au data set and 3 k for 9.2 GeV Au+Au data set.

Centrality Bin	Multiplicity	Geometric Cross Section
1	19-29	$50-60\%$
2	30-45	$40-50\%$
3	46-66	$30-40\%$
4	67-97	$20-30\%$
5	98-138	$10-20\%$
6	$\geq$139	$0-10\%$

Table 3.5: Run V centrality bins in Cu+Cu collisions at $\sqrt{s_{NN}}$ = 200 GeV.

There are two kind of reconstructed tracks. One is the global track, other is the primary track. The global track is defined by the helix fit to the TPC points one by one. The collision vertex can be identified from all the reconstructed global tracks. The primary track is defined by the helix fit to the TPC points along with the vertex. The number of tracks (i.e. multiplicity) measured by the main TPC is used to define the STAR's centrality intervals. The TPC reference multiplicity is the number of the primary tracks in the TPC with the 15 or more fit points having the pseudo-rapidity

Centrality Bin	Multiplicity	Geometric Cross Section
1	14-21	$50-60\%$
2	22-32	$40-50\%$
3	33-48	$30-40\%$
4	49-70	$20-30\%$
5	71-100	$10-20\%$
6	$\geq$101	$0-10\%$

Table 3.6: Run V centrality bins in Cu+Cu collisions at $\sqrt{s_{NN}} = 62.4$ GeV.

Centrality Bin	Multiplicity	Geometric Cross Section
1	10-20	$70-80\%$
2	21-38	$60-70\%$
3	39-68	$50-60\%$
4	69-113	$40-50\%$
5	114-177	$30-40\%$
6	178-268	$20-30\%$
7	269-398	$10-20\%$
8	399-484	$5-10\%$
9	$\geq$485	$0-5\%$

Table 3.7: Run VII centrality bins in Au+Au collisions at $\sqrt{s_{NN}} = 200$ GeV.

Centrality Bin	Multiplicity	Geometric Cross Section
1	17-73	$30-60\%$
2	74-161	$10-30\%$
3	$\geq$162	$0-10\%$

Table 3.8: Run VII centrality bins in Au+Au collisions at $\sqrt{s_{NN}} = 9.2$ GeV.

from -0.5 to 0.5 and a distance of closet approach (DCA) to the primary vertex less than 3 cm.

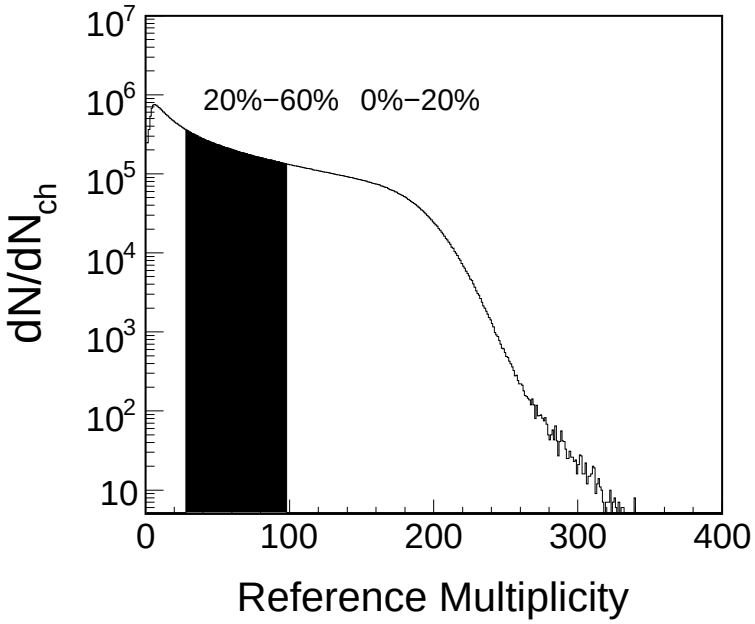

Figure 3.1: The reference multiplicity distribution in Cu+Cu collisions at $\sqrt{s_{NN}} = 200$ GeV. The geometry cross section used for v_2 analysis is combined into two centrality intervals shown in the Figure.

The inclusion of inner tracking for the Run VII Au+Au 200 GeV data rendered reference multiplicity a poor method to determine centrality. There is a dependence on the primary vertex position for the reconstruction efficiency in the $|V_z| < 30$ cm region. The dependence was generally absent for TPC tracking only used in many of the previous productions, and is undesirable since it requires the centrality cuts to change as a function of V_z. To this end, another variable called global reference multiplicity (gRefmult) was introduced. The only difference between the reference multiplicity and global reference multiplicity is that the global reference multiplicity requires the primary tracks in the TPC with the 10 or more fit points. The remaining issues are biases on multiplicity distribution introduced by the main online Vertex Position Detector (VPD) trigger setup (200013). The biases come from two sources. Firstly, over the full range in V_z, the VPD is more efficient at triggering on central events relative to peripheral. This leads to a general deficit in peripheral events for a given data sample. The second

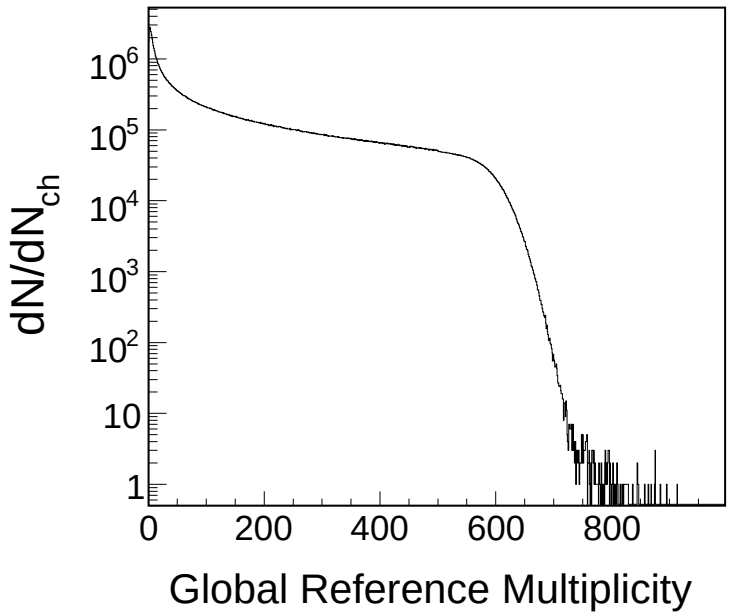

Figure 3.2: The Global reference multiplicity (gRefmult) distribution in Au+Au collisions at $\sqrt{s_{NN}} = 200$ GeV.

comes from a centrality dependence of the VPD's online V_z resolution which is worse for peripheral events relative to central. Since the trigger setup (200013) insisted events fall within the inner tracking acceptance i.e. with an online cut of $|V_z| < 5$ cm, the resolution issue means that events at the higher $|V_z|$'s are more likely to peripheral whereas the events at lower $|V_z|$'s are more likely to be central. The V_z dependent biases in multiplicity distribution require a re-weighting correction to be applied for all analysis. The correction has to be applied as a function of V_z in 2 cm bins for acceptance reasons. In a given V_z bin, firstly the weights have to be determined. This is done by normalizing the 1D global reference multiplicity distribution by the number of events with global reference multiplicity > 500. The ideal multiplicity distribution from MC Glauber then has to be divided by the normalized global reference multiplicity distribution to calculate the weights.

The centrality bins and the corresponding geometric cross section for Cu+Cu and Au+Au collisions are listed in Table 3.5 - 3.8. A part of low multiplicity events are rejected due to a lower cut on CTB to reject the non-hadronic events. The total number of events should be corrected by the Glauber model. The geometric cross section listed

in Table 3.5 - 3.7 is the fraction of the corrected total number of events.

Figure 3.1 shows reference multiplicity distribution without the Glauber correction in Cu+Cu collisions at $\sqrt{s_{NN}} = 200$ GeV. Events more peripheral than 60% centrality are not used in the analysis. The three combined centrality bins used in the analysis are $0-20\%$, $20-60\%$ and $0-60\%$, which are indicated in the Figure 3.1. Figure 3.2 shows global reference multiplicity distribution with the re-weighting correction mentioned before.

3.2 K^0_S, Λ, Ξ and Ω Reconstruction

We reconstruct K^0_S, Λ, Ξ and Ω through their weak decay channels. The properties of these decays are summarized in Table 3.9.

Particle Type	Decay Channel	Branching Ratio (%)	$c\tau$ (cm)	Mass (GeV/c^2)
K^0_S	$\pi^+ + \pi^-$	68.95 ± 0.14	2.68	0.497
$\Lambda(\bar{\Lambda})$	$p + \pi^-$ $(\bar{p} + \pi^+)$	63.9 ± 0.5	7.89	1.115
Ξ^- $(\bar{\Xi}^+)$	$\Lambda + \pi^-$ $(\bar{\Lambda} + \pi^+)$	99.89 ± 0.04	4.91	1.321
Ω^- $(\bar{\Omega}^+)$	$\Lambda + K^-$ $(\bar{\Lambda} + K^+)$	67.8 ± 0.7	2.46	1.672

Table 3.9: K^0_S, Λ, Ξ and Ω weak decay properties

3.2.1 K^0_S and Λ Reconstruction

The identification of K^0_S and Λ is based on statistics-wise invariant mass distribution. The charged p and π tracks are identified by the energy loss in TPC. We define the four-momentum of p and π by assigning their mass and momentum measured from the helix in TPC and then calculate the invariant mass of all possible pairs of positive and negative charged particles.

There are many fake decay vertex among the reconstructed decay vertex known as the combinatorial background. Many reasons could lead to the combinatorial background such as the misidentification of daughter track, the decay vertex close to the primary vertex and daughter tracks of a pair from different V^0.

We utilize decay geometry to reject fake pairs. $c\tau$ of K^0_S and Λ is 2.68 cm and 7.89 cm. Most of them will decay in the TPC of 2 m radius. In the laboratory frame, the decay vertex is in the order of a few centimeter further than primary vertex with several hundreds microns. So the decay vertex is well separated from the primary vertex. The decay topology is shown in Figure 3.3. The V^0 is named after the "V" topology with the "0" net charge. The dca (distance of closet approach) between two daughter tracks is the parameter to determine the point of the decay vertex. The real decay vertex should distribute at smaller dca than fake decay vertex. Dca1 (Dca2) is the dca of the daughter to the primary vertex. The decay daughters should distribute at larger values than primary tracks. b is the dca from the primary vertex to the direction of V^0 momentum. Ideally, b is equal to zero. rv is the distance which V^0 travels in TPC (decay length).

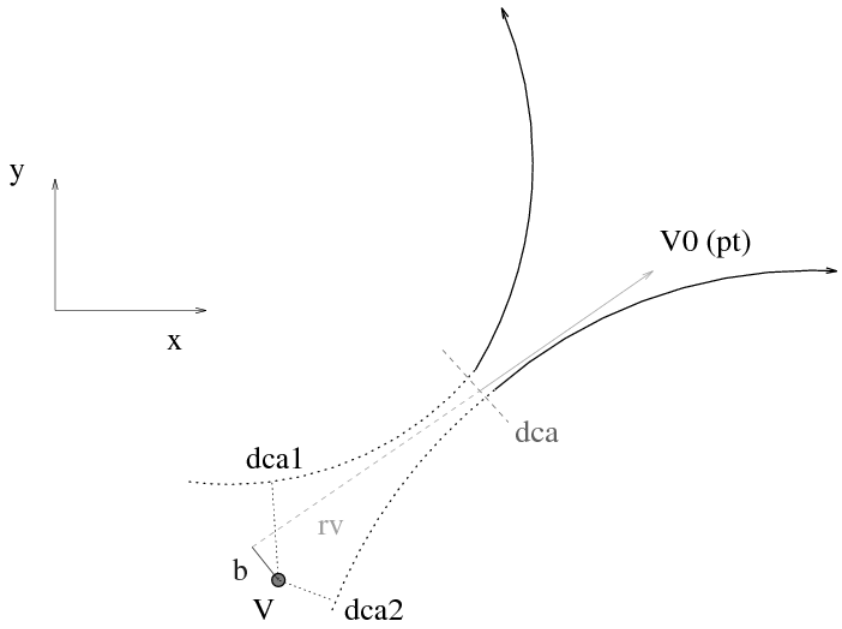

Figure 3.3: V^0 decay topology, Figure from [Mar98a]

Table 3.10 and Table 3.11 list the V^0 optimized cuts for K^0_S and Λ in Cu+Cu collisions at $\sqrt{s_{NN}}$ = 200 GeV, respectively. These cuts are used for this v_2 analysis. Applying these cuts, the signal over background ratio will be significantly enhanced.

p_T (GeV/c)	< 0.8	0.8-3.6	> 3.6
π dca to primary vertex (cm)	> 1.5	> 1.0	> 0.5
dca between daughters (cm)	< 0.7	< 0.75	< 0.5
dca from primary vertex to V0	< 0.7	< 0.75	< 0.5
decay length (cm)	4-150	4-150	10-120

Table 3.10: Cuts selection criteria for K^0_S in Cu+Cu collisions at $\sqrt{s_{NN}} = 200$ GeV.

p_T (GeV/c)	< 0.8	0.8-3.6	> 3.6
π dca to primary vertex (cm)	> 2.5	> 2.0	> 1.0
p dca to primary vertex (cm)	> 1.0	> 0.75	> 0
dca between daughters (cm)	< 0.7	< 0.75	< 0.4
dca from primary vertex to V0	< 0.7	< 0.75	< 0.75
decay length (cm)	4-150	4-150	10-125

Table 3.11: Cuts selection criteria for Λ in Cu+Cu collisions at $\sqrt{s_{NN}} = 200$ GeV.

3.2.2 Ξ and Ω Reconstruction

Both Ξ and Ω leave a signature decay structure: a three-track "cascade" topology, as seen on Figure 3.4. Any multi-strange baryon decays into a charged meson and a neutral Λ baryon, which in turn decays into a pion and a proton. The track information for the multi-strange particle decay is carried by the three daughter tracks, shown in Figure 3.4 as solid lines. Thus, reconstruction of a multi-strange baryon involves a step-by-step reconstruction of a multilateral vertex, first finding a suitable Λ baryon candidate, and then finding a matching meson.

The three resultant particles are then separately reconstructed in the TPC, as described in last section. A Λ decay is reconstructed from its daughters. But first, one needs to identify the tracks that compose a given V^0 decay vertex.

Then, particle selection is made based on seven possible topological criteria, described in Figure 3.4, three track criteria, and a cleaner cut around the Λ daughter mass. The three track quality criteria are the number of fit points used to make a track (there are

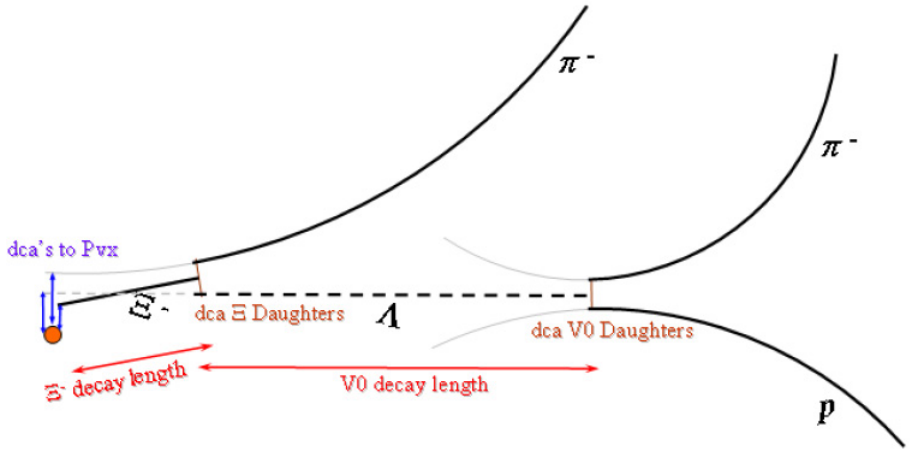

Figure 3.4: The topology of a Ξ decay, where the weak decay of a Ξ^- baryon is taken as an example. The charged tracks are represented in the figure by solid lines, and the neutral Λ track by a dashed line. The vertex type is called a "cascade" because of the multi-stage decay process. All seven geometrical variables used for Ξ^- topological reconstruction are represented.

three because there are three tracks involved in the Ξ (Ω) reconstruction). The possible topological criterias were:

1. Distance of closest approach of the multi-strange baryon to the primary vertex (dca Ξ (Ω) to PV).

2. Distance of closest approach of the Λ daughter to the primary vertex (dca Λ to PV).

3. Distance of closest approach of the bachelor pion to the primary vertex (dca Bach. to PV).

4. Distance of closest approach between Ξ (Ω) daughters, Λ and the bachelor pion (kaon).

5. Distance of closest approach between Λ daughters, the proton and the Λ daughter pion.

6. The decay length of Ξ (Ω) baryon.

7. The decay length of Λ daughter.

Table 3.12 lists the optimized cuts for Ξ (a) and Ω (b) in collisions at $\sqrt{s_{NN}} = 200$

GeV.

Cut Parameter	Cut Value
dca Ξ to PVx	< 0.4
dca bach. to PVx	> 1.5
dca Λ to PVx	> 0.1
dca Λ to bach.	< 0.7
dca p to π daug.	< 0.7
dl Ξ	≥ 5 cm
dl Λ	> 23 - $4 \times$ dl Ξ
mass Λ	± 0.007 GeV/c^2
nHits bach.	≥ 25
nHits p	≥ 25
nHits π	≥ 25
N. $\sigma_{dE/dx}$ bach.	3
N. $\sigma_{dE/dx}$ p	3
N. $\sigma_{dE/dx}$ π	3

(a)

Cut Parameter	Cut Value
dca Ω to PVx	< 0.6
dca bach. to PVx	$> 0.1 + 1.6 \times \sqrt{\text{dca}\Omega \text{ to PV}}$
dca Λ to PVx	$> 0.1 + 1.8 \times \sqrt{\text{dca}\Omega \text{ to PV}}$
dca Λ to bach.	< 0.5
dca p to π daug.	< 0.3
dl Ξ	≥ 3.2 cm
dl Λ	≥ 3.2 cm
mass Λ	± 0.007 GeV/c^2
nHits bach.	≥ 30
nHits p	≥ 30
nHits π	≥ 25
N. $\sigma_{dE/dx}$ bach.	3
N. $\sigma_{dE/dx}$ p	3
N. $\sigma_{dE/dx}$ π	3

(b)

Table 3.12: Selection parameters for Ξ (a) and Ω (b) in $\sqrt{s_{NN}} = 200$ GeV data. dca stands for 'distantce of closest approach', dl stands for 'decay length', bach. stands for 'bachelor', daug. for 'daughter', and PVx is the abbreviation of 'primary vertex'.

3.2.3 Invariant Mass Distributions

Figure 3.5 shows K^0_S, Λ, Ξ and Ω invariant mass distribution in $\sqrt{s_{NN}} = 200$ GeV Cu+Cu collisions for a selected p_T region in mini-bias collisions $(0 - 60\%)$. The red dashed lines are the background estimation.

For K^0_S and Λ, the remaining backgrounds are estimated from the fit to the invariant mass distribution with functions describing signals and backgrounds. The fit function is two gaussian plus a polynomial. We use two gaussian functions with the same mass peak parameter to describe signal and use a polynomial function to describe the backgrounds. The fourth and second order polynomial functions are used in order to estimate the systematic errors from background uncertainties. The systematic error is a few percent,

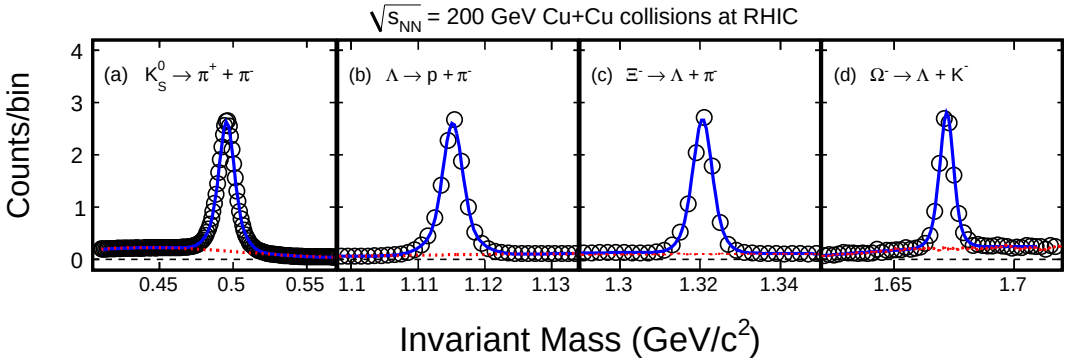

Figure 3.5: Invariant mass distributions for (a) K^0_S ($1.2 < p_T < 1.4$ GeV/c), (b) Λ ($1.4 < p_T < 1.6$ GeV/c), (c) Ξ ($1.25 < p_T < 1.75$ GeV/c) and (d) Ω ($0 < p_T < 10$ GeV/c) in $\sqrt{s_{NN}}$ = 200 GeV Cu+Cu minimum bias ($0 - 60\%$) collisions. The dashed lines are the background estimation from the fit to the invariant mass distribution for K^0_S and Λ, the reconstruction of pion (kaon) and rotated Λ track pairs for Ξ and Ω. For clarity, the invariant mass distributions for K^0_S, Λ, Ξ and Ω are scaled by 1/50 000, 1/130 000, 1/5 000 and 1/1 000, respectively. The error bars are shown only for the statistical uncertainties.

we will discuss in details later. The background distribution is estimated from the polynomial in the fit. The signal distribution is estimated by data minus polynomial. The signal over total ratio distribution and background over total ratio distribution (fit over data) will be used to extract K^0_S and Λ signal v_2 .

For Ξ and Ω, the background can be reproduced by rotating the Λ candidate by 180^0 in the transverse plane and then reconstructing the Ξ and Ω candidates. The rotation of the Λ breaks the correlation in the invariant mass and therefore mimics the background of uncorrected decay pairs.

3.3 Event Plane

In this section, we introduce the Fourier expansion of azimuthal particle distribution and its properties with respect to the reaction plane. And we also introduce event plane which is the estimate of the true reaction plane determined by using the signal of flow itself.

3.3.1 Fourier Expansion of Azimuthal Distribution

Since the azimuthal distribution of emitted particles $dN/d\phi$ is the periodic function with 2π fundamental period, it is natural to expand azimuthal distribution into fourier series with 2π period.

$$\begin{aligned}\frac{dN}{d\phi} &= \frac{x_0}{2\pi} + \frac{1}{\pi}\sum_{n=1}^{\infty}(x_n\cos(n\phi) + y_n\sin(n\phi)) \\ &= \frac{x_0}{2\pi}(1 + 2\sum_{n=1}^{\infty}(\frac{x_n}{x_0}\cos(n\phi) + \frac{y_n}{y_0}\sin(n\phi)))\end{aligned} \tag{3.1}$$

Because there is only a finite number of particles in each event, the Fourier coefficients x_n and y_n can be expressed as:

$$x_n = \int_0^{2\pi} d\phi \frac{dN}{d\phi}\cos(n\phi) = \sum_{n=1}^{M} w_i\cos(n\phi_i) \equiv Q_x \tag{3.2}$$

$$y_n = \int_0^{2\pi} d\phi \frac{dN}{d\phi}\sin(n\phi) = \sum_{n=1}^{M} w_i\sin(n\phi_i) \equiv Q_y \tag{3.3}$$

where i runs over all particles (M) used to determined the event plane, ϕ_i is the azaimuthal angle of the emitted i^{th} particle and w_i is the weight (p_T, ϕ etc) to minimize the dispersion of event plane (i.e. maximum event plane resolution). We define the following two-dimentional vector $\mathbf{Q} = (Q_x,\ Q_y)$ called as a flow vector.

If we assume ϕ in Eq. 3.1 is defined relative to the reaction plane, then $dN/d\phi$ becomes an even function and we can omit y_n terms since the integration would be zero in Eq. 3.3,

$$\frac{dN}{d\phi} = \frac{x_0}{2\pi}(1 + 2\sum_{n=1}^{\infty}\frac{x_n}{x_0}\cos(n\phi)) = \frac{x_0}{2\pi}(1 + 2\sum_{n=1}^{\infty}\frac{x_n}{x_0}\cos(n[\phi_{\text{lab}} - \Psi])) \tag{3.4}$$

Where ϕ_{lab} is the azimuthal angle of fixed orientation in the experiment, Ψ is the azimuthal angle of true reaction plane and $v_n = x_n/x_0$ is the magnitude of anisotropy. We introduce the following two variables,

$$v_n^{\text{obs}} = \frac{x_n}{x_0} \tag{3.5}$$

$$\Psi_n = \frac{1}{n}\tan^{-1}(\frac{y_n}{x_n}), \quad 0 \leq \Psi_n \leq \frac{2\pi}{n} \tag{3.6}$$

From Eq. 3.5 and 3.6, measured azimuthal distribution $r^m(\phi)$ can be given by

$$r^m(\phi) = \frac{x_0}{2\pi}(1 + 2\sum_{n=1}^{\infty} v_n^{\rm obs}\cos(n[\phi_{\rm lab} - \Psi_n])) \tag{3.7}$$

Compare Eq. 3.4 and 3.7, one can see that Ψ_n gives event plane, which is the estimate of an azimuthal angle of true reaction plane. It is reconstructed from the reaction products event-by-event basis. The reconstructed plane (event plane) differs in general from the true reaction plane by an error $\Delta\Psi$, thus, the measured azimuthal angle of event plane Ψ_n is related to the true azimuthal angle of reaction plane Ψ by $\Psi_n = \Psi + \Delta\Psi$. Averaging over many events, one obtains the following relation between the measured and true Fourier coefficients:

$$\begin{aligned} v_n^{\rm obs} &= \langle\cos(n[\phi_{\rm lab} - \Psi_n])\rangle \\ &= \langle\cos(n[\phi_{\rm lab} - \Psi] - n[\Psi_n - \Psi])\rangle \\ &= \langle\cos(n[\phi_{\rm lab} - \Psi])\cdot\cos(n\Delta\Psi)\rangle + \langle\sin(n[\phi_{\rm lab} - \Psi])\cdot\sin(n\Delta\Psi)\rangle \\ &= \langle\cos(n[\phi_{\rm lab} - \Psi])\cdot\cos(n\Delta\Psi)\rangle \\ &= v_n\langle\cos(n\Delta\Psi)\rangle \end{aligned} \tag{3.8}$$

from line 3 to 4, we assume that $\phi_{\rm lab} - \Psi$ and $\Delta\Psi$ are statistically independent. And we use the reflection symmetry of $\phi_{\rm lab} - \Psi$ and $\Delta\Psi$, i.e. average sine term vanish under that condition. This assumption is valid for the system with large multiplicity.

3.3.2 Event Plane Determination

Since an azimuthal angle of true reaction plane is unknown, we have to determine estimated reaction plane (event plane) experimentally. In this analysis, the Time Projection Chamber (TPC) and the Forward Forward Time Projection Chambers (FTPC) are used to determine an event plane for each event. Both the TPC and the FTPC have full azimuthal coverage. The FTPC cover pseudo-rapidity $2.5 < |\eta| < 4.0$. This rapidity gap helps to reduce non-flow contributions, which is the correlations not originated

from the reaction plane, such as di-jet correlations, resonance decays, and Bose-Einstein correlations.

Event plane is calculated by the Eq. 3.9 - 3.11

$$Q_2 \cos(2\Psi_2) = X_2 = \sum_i w_i \cos(2\phi_i) \tag{3.9}$$

$$Q_2 \sin(2\Psi_2) = Y_2 = \sum_i w_i \sin(2\phi_i) \tag{3.10}$$

$$\Psi_2 = \left(\tan^{-1} \frac{\sum_i w_i \sin(2\phi_i)}{\sum_i w_i \cos(2\phi_i)} \right) /2 \tag{3.11}$$

where X_2 and Y_2 is the projection of event plane to x and y axes respectively. The sum goes over particles used in the event plane calculation, which is called flow tracks. The flow tracks selection criteria are list in Table 3.13, where the nHits means the number of the hits used for reconstruction of the tracks, nHits/nMax means the ratio of the number of fit hits to maximum possible hits. The w_i is weights. Usually the weights are assigned with the transverse momentum. This choice of weights is to make the event plane resolution the best by maximizing the flow contributions to the flow vector. Note that the event plane angle Ψ_2 is in the range $0 < \Psi_2 < \pi$.

Flow track selection criteria	
nHits	> 15
nHits/nMax	> 0.52
dca	< 2 cm
transverse momentum	$0.15 < p_T < 2.0$ GeV/c

Table 3.13: Selection criteria for flow tracks used in the event plane reconstruction.

3.3.3 Flattening Event Plane Distribution

The event plane distribution should be isotropic in the laboratory frame. Thus the event plane distribution has to be a flat distribution if the detectors have the ideal acceptance.

In experiments, flattening the event plane procedure is necessary due to the acceptance effect. For event plane reconstructed from TPC tracks, ϕ weight, which is generated by inverting the ϕ distributions of detected tracks for a large event sample, is an effective method to flatten the distribution. The detector bias is removed by applying the ϕ weight at the ϕ of each track to that track. The ϕ weights are folded into the weight w_i in Equation 3.9 and 3.10.

Due to the serious loss of acceptance for FTPCs (the number of tracks detected by the best sector is about 6 times greater than the worst one), ϕ weight method is not enough to generate the flat event plane distribution. Thus, the shifting method [Bar97a] is applied to force the event plane distribution to be flat. The Equation 3.12 shows the formula for the shift correction. The average in Equation 3.12 goes over a large sample of events. In the analysis, the correction is done up to twentieth harmonic. The distributions of $\Psi_2^{\rm East}$ and $\Psi_2^{\rm West}$ are flatten separately and then the full-event plane distributions are flattened. Accordingly, the observed v_2 and resolution are calculated using the shifted (sub)event plane azimuthal angle.

$$\Psi^{'} \;=\; \Psi + \sum_n \frac{1}{n}[-\langle \sin(2n\Psi)\rangle \cos(2n\Psi) + \langle \cos(2n\Psi)\rangle \sin(2n\Psi)] \qquad (3.12)$$

Figure 3.6 shows the second harmonic event plane azimuthal distribution after shift corrections are applied. To show how flat it is, we do a constant fit to the event plane azimuthal distribution. The χ^2/ndf is less than 1. As the event plane is flat, the acceptance effects will not bias the measurements of v_2.

3.3.4 Event Plane Resolution

The observed v_2 is correlated to the event plane. Due to finite multiplicity in the event plane calculation, there are some uncertainties between the event plane and real reaction plane. The observed v_2 has to be corrected by the event plane resolution, which is given by Equation 3.13 [Vol98a].

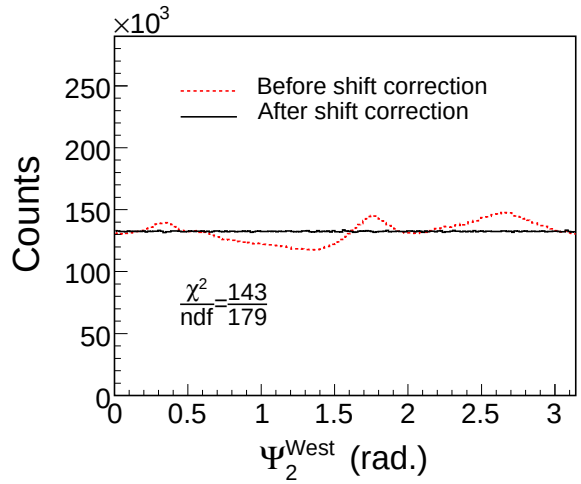

(a)

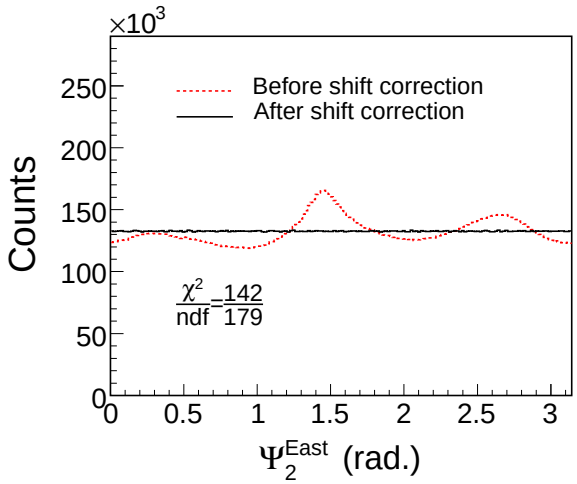

(b)

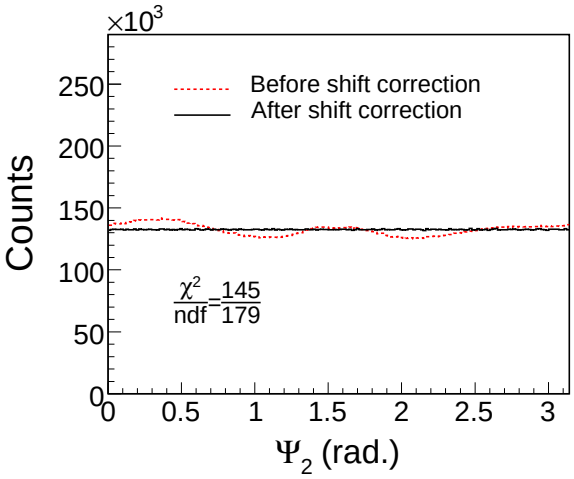

(c)

Figure 3.6: (a) Event plane reconstructed from west FTPC, (b) East FTPC, (c) West plus east FTPC, before and after shift correction. The χ^2 is for a fit to a constant.

$$v_2 = \frac{v_2^{\rm obs}}{\langle \cos[2(\Psi_2 - \Psi_r)] \rangle} \tag{3.13}$$

The mean cosine sums over the whole event sample. Where v_2, $v_2^{\rm obs}$, Ψ_2 and Ψ_r are the real v_2, observed v_2, the event plane angle and the real reaction plane angle. It is found that $\langle \cos[2(\Psi_2 - \Psi_r)] \rangle$ is the reaction plane resolution. To calculate it, we divide a full event into two sub-sets of tracks (sub-events). According to Equation 3.11, we calculate the event plane of two sub-events separately. The event plane resolution for the sub-event is given by Equation 3.14 [Pos98a].

$$\langle \cos[2(\Psi_2^A - \Psi_r)] \rangle = \sqrt{\langle \cos[2(\Psi_2^A - \Psi_2^B)] \rangle} \tag{3.14}$$

Since we have two independent event plane from west and east FTPC, we can estimate the event plane resolution by measuring the relative azimuthal angle $\Delta\Psi_2^{\rm FTPC} \equiv 2(\Psi_2^{\rm West} - \Psi_2^{\rm East})$. This is based on the assumption that there are no other correlations except flow effects. Taking into account that the multiplicity of the full event is twice as large as that of the sub-event, the full event plane resolution is given by Equation 3.15.

$$\langle \cos[2(\Psi_2 - \Psi_r)] \rangle \;=\; C\sqrt{\langle \cos[2(\Psi_2^A - \Psi_2^B)] \rangle} \tag{3.15}$$

In the case of low resolution (≤ 0.2), such as for the FTPC event plane, C approaches $\sqrt{2}$.

Centrality Bin	Resolution	Geometric Cross Section
1	0.112 ± 0.004	$50 - 60\%$
2	0.138 ± 0.004	$40 - 50\%$
3	0.163 ± 0.003	$30 - 40\%$
4	0.180 ± 0.003	$20 - 30\%$
5	0.175 ± 0.003	$10 - 20\%$
6	0.147 ± 0.003	$0 - 10\%$
	0.160 ± 0.001	$0 - 60\%$

Table 3.14: Resolution for the FTPC event plane in Cu+Cu collisions at $\sqrt{s_{NN}} = 200$ GeV.

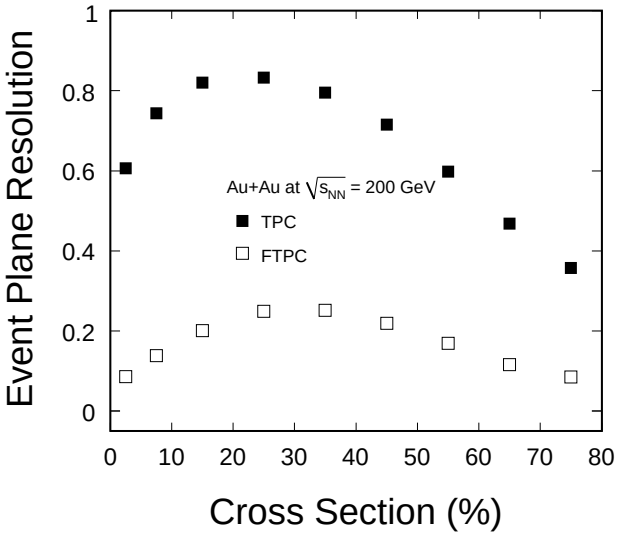

Figure 3.7: Resolution for the TPC and FTPC event plane in Au+Au collisions at $\sqrt{s_{NN}}$ = 200 GeV.

Table 3.14 shows the resolution for FTPC event plane in Cu+Cu collisions at $\sqrt{s_{NN}}$ = 200 GeV. The resolution depends on the number of tracks used and the magnitude of the event asymmetry. For the most peripheral collisions, the small multiplicity reduces the resolution while for the most central collisions, the small v_2 weakens it. As a consequence, the resolution reaches its maximum at the centrality of $20-30\%$ of the collision cross section. Figure 3.7 shows the resolution for the TPC and FTPC event plane in Au+Aucollisions at $\sqrt{s_{NN}}$ = 200 GeV, the TPC event plane resolution is greater than that of the FTPC by a factor of 4.

3.4 v_2 Methods

In this section, we discuss the methods to extract v_2.

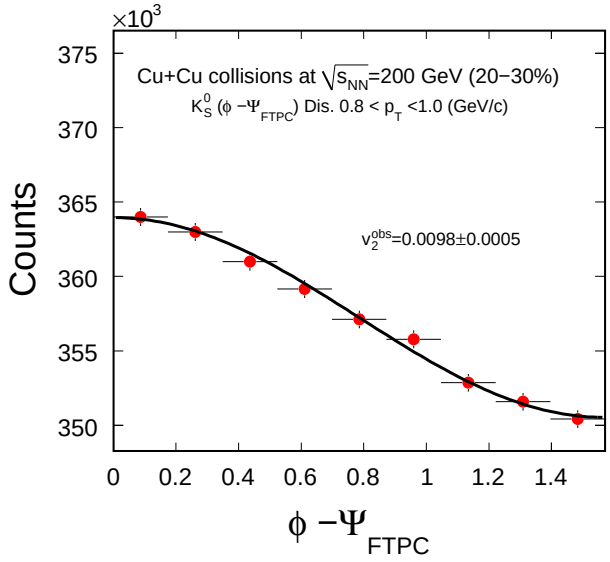

Figure 3.8: The distribution of $dN/d(\phi - \Psi_{\rm FTPC})$ for K^0_S at a chosen p_T bin (0.8 - 1.0 GeV/c) in Cu+Cu collisions at $\sqrt{s_{NN}}$ = 200 GeV. Black line shows the fit curve.

3.4.1 The Event Plane Method

Fig. 3.8 shows the $dN/d(\phi - \Psi)$ distribution for K^0_S at a chosen p_T bin (0.8 - 1.0 GeV/c). The measured v_2 is extracted by fitting $dN/d(\phi - \Psi)$ distribution with Fourier expansion of azimuthal distribution:

$$\frac{dN}{d(\phi - \Psi)} = N(1 + 2v_2^{\rm obs}\cos(2(\phi - \Psi_2))) \tag{3.16}$$

Where N and $v_2^{\rm obs}$ are free parameters. The measured v_2, i.e. $v_2^{\rm obs}$, need to be corrected with event plane resolution by Eq. 3.13.

3.4.2 The Scalar Product Method

The Scalar Product method [Adl02b, Ada05c] is similar to the Event Plane method, and gives v_2 as:

$$v_2(p_T) = \frac{\langle Q_2 u^*_{2,i}(p_T)\rangle}{2\sqrt{\langle Q_2^A Q_2^{B*}\rangle}} \tag{3.17}$$

where $u_{2,i} = \cos(2\phi_i) + i\sin(2\phi_i)$ is a unit vector of the ith particle, $Q_2 = \sum_k u_{2,k}$ is the flow vector with the sum running over all other particles k in the event. The superscript * denotes the complex conjugate of a complex number. A and B denote the two subevents. In the case that Q_2 is normalized to a unit vector, Eq. (3.17) reduces to the Event Plane method. In the Scalar Product method, one can use a different (re-centering) technique [Sel08a] to correct for detector effects, which presents an alternative to the weighting and shifting procedures. The Scalar Product method is applied to the v_2 measurement of charged hadrons.

3.4.3 The v_2 versus $m_{\rm inv}$ Method

v_2 versus $m_{\rm inv}$ method is used to measure v_2 of strange hadrons. K^0_S, Λ, Ξ and Ω candidates are identified on statistical basis. The invariant mass $m_{\rm inv}$ distributions show there are some remaining combinatorial backgrounds. The purpose of v_2 versus $m_{\rm inv}$ method is to extract signal v_2.

The essence of v_2 versus $m_{\rm inv}$ method is based on the following Equation:

$$v_2^{\rm Sig+Bg}(m_{\rm inv}) = v_2^{\rm Sig}\frac{\rm Sig}{\rm Sig+Bg}(m_{\rm inv}) + v_2^{\rm Bg}(m_{\rm inv})\frac{\rm Bg}{\rm Sig+Bg}(m_{\rm inv}) \qquad (3.18)$$

If we know signal plus background v_2 as a function of $m_{\rm inv}$ on left side of Equation 3.18, signal over total ratio as a function of $m_{\rm inv}$ and background over total ratio as a function of $m_{\rm inv}$ on right side of Equation 3.18, signal v_2 and background v_2 as a function of $m_{\rm inv}$ remain to be determined. With parameterizing $v_2^{\rm Bg}(m_{\rm inv})$ as a certain function, $v_2^{\rm Sig}$ can be extracted by a fit to $v_2^{\rm Sig+Bg}(m_{\rm inv})$ with Equation 3.18.

To illustrate this method, Figure 3.9 shows an example for K^0_S in Au+Au collisions at $\sqrt{s_{NN}} = 200$ GeV. Panel (a) shows invariant mass distribution for K^0_S. A $4^{\rm th}$ order polynomial fit to describe the background distribution is shown as solid line. $\frac{\rm Bg}{\rm Sig+Bg}(m_{\rm inv})$ is calculated by dividing fit line by data. $\frac{\rm Sig}{\rm Sig+Bg}$ is calculated by $(1 - \frac{\rm Sig}{\rm Sig+Bg})$. v_2 of K^0_S candidates represented by open circles are calculated and plotted in panel (b). The fit to v_2 of K^0_S candidates with Equation 3.18 is shown in solid line. The background contributions and the signal contributions are shown as dashed line and dot-dashed line

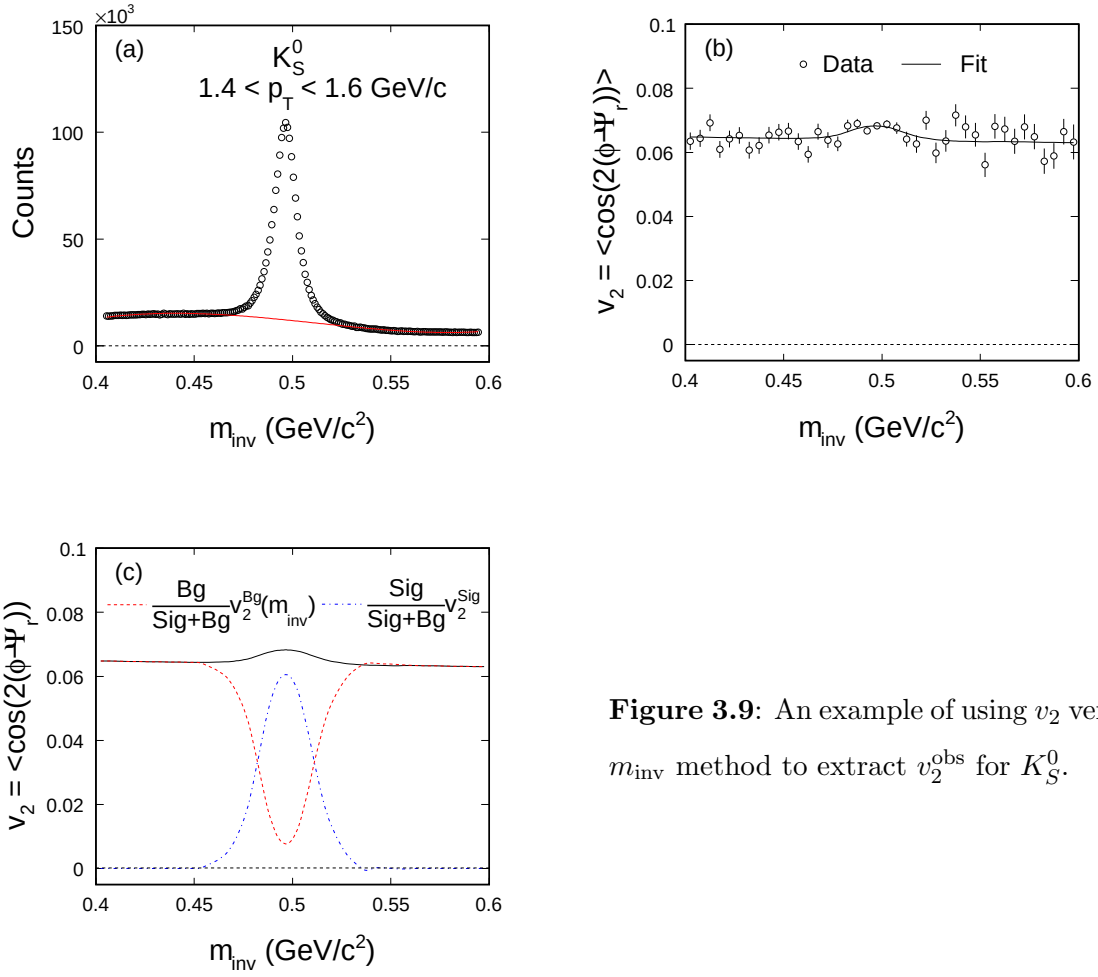

Figure 3.9: An example of using v_2 versus $m_{\rm inv}$ method to extract $v_2^{\rm obs}$ for K^0_S.

in (c) along with the total fit.

This method gives robust results: We fit a set of data points over wide $m_{\rm inv}$ region. Data points far from the mass peak region are only from background contributions since $\frac{\rm Bg}{\rm Sig+Bg}$ is equal to 1. $v_2^{\rm Sig+Bg}$ data points in this region have strong constraints on $v_2^{\rm Bg}$ when doing the fit. $v_2^{\rm Sig+Bg}$ data points in the mass region under peak constraint $v_2^{\rm Sig}$ with given $\frac{\rm Sig}{\rm Sig+Bg}$ and $\frac{\rm Bg}{\rm Sig+Bg}$ ratios. A large variation of $v_2^{\rm Sig}$ would lead to an strong disagreement of the fit curves with the measured data. Thus the shape of dip or bump of $v_2^{\rm Sig+Bg}$ in the mass region under peak is not necessary to measure v_2. The systematic uncertainty of this method lies in the estimate of $\frac{\rm Sig}{\rm Sig+Bg}$ and $\frac{\rm Bg}{\rm Sig+Bg}$ ratio as a function of $m_{\rm inv}$. This systematic uncertainty is studied by using different functions to fit the background, which will be discussed in systematics section.

3.5 Systematic Uncertainties

3.5.1 Systematic Error on the FTPC Event Plane

The systematic uncertainties in v_2 analysis procedures are studied. We estimate the systematic errors from shifting of the FTPC event plane by comparing v_2 using different maximum harmonic in Eq. (3.12). The systematic errors from the flattening process are less than 1%.

3.5.2 Systematic Error on Reconstruction of Strange Hadrons

The systematic errors in K^0_S and Λ v_2 measurement from background uncertainty, combining centrality and cut criteria are estimated using Event Plane method. The background uncertainty is estimated by fitting the background with second and fourth order polynomial. The systematic uncertainty from cut criteria is estimated by varying cuts with reasonable values.

The systematic errors on K^0_S and Λ from background and cut criteria are summarized in Table 3.15.

	K^0_S		Λ	
Centrality	Background	Cut criteria	Background	Cut criteria
$0-60\%$	1%	2%	1%	2%
$0-20\%$	1%	2%	1%	4%
$20-60\%$	4%	1%	5%	1%

Table 3.15: Summary of systematic error of v_2 on reconstruction of strange hadrons in Cu+Cu collisions at $\sqrt{s_{NN}}$ = 200 GeV.

3.5.3 Systematic Error on Non-flow Effect

The method of determining v_2 using cumulants of various orders has been shown to eliminate non-flow correlations. However, the method is useful only for large values of flow and multiplicity. For the relatively low values of flow and multiplicity seen in Cu+Cu collision, the non-flow correlations have been estimated, as described below.

The Event Plane method with the TPC event plane is sensitive to non-flow effects. Particles of interest tend to correlate with particles used in the flow vector calculation due to short-range non-flow correlations. Also, particles of two random sub-events tend to have those correlations. Thus, non-flow exists in both the observed v_2 (the numerator of Eq. (3.13)) and the resolution (Eq. (3.15)). To reduce non-flow effects due to short-range correlations, we take advantage of the large η gap between the two FTPCs sitting at the two sides of the collision in the forward regions. Non-flow is reduced by the η gap between the TPC and FTPCs, but this may not be large enough to remove all non-flow correlations. Thus, we investigate these effects by comparing the azimuthal correlations measured in Cu+Cu to those in p+p collisions, where all correlations are assumed to be of non-flow origin [Ada04b]. Taking into account the non-flow contribution, the numerator of Eq. (3.17) can be written as follows [Ada04b, Adl02b]:

$$\langle \sum_i \cos[2(\phi_{p_T} - \phi_i)] \rangle \;=\; M v_2(p_T)\overline{v_2} \;+\; \text{nonflow} \tag{3.19}$$

where ϕ_{p_T} is the azimuthal angle of particles from a given p_T bin ($u^*_{2,i}$ in Eq. (3.17)) and the sum goes over all tracks k in an event used to determine the flow vector (Q_2 in

Eq. (3.17)). The angled brackets denote averaging over the events. The first term in the right-hand side of Eq. (3.19) represents the contribution from elliptic flow. $v_2(p_T)$ is the value of elliptic flow at a given p_T. $\overline{v_2}$ is the elliptic flow on average for all particles used in the sum of Eq. (3.19). The multiplicity of particles contributing to the sum is denoted by M. All other correlations subject to non-flow go to the second term in the right-hand side of Eq. (3.19). It is assumed that the quantity $\langle Q_2 u^*_{2,i}(p_T)\rangle$ in p+p collisions can be used to estimate the non-flow in AA collisions [Ada04b, Ada05c].

$$M v_2(p_T)\overline{v_2} \ = \langle Q_2 u^*_{2,i}(p_T)\rangle_{AA} - \ \langle Q_2 u^*_{2,i}(p_T)\rangle_{pp} \tag{3.20}$$

Dividing both sides by $2\sqrt{\langle Q_2^A Q_2^{B*}\rangle_{AA}}$ as in Eq. (3.17) gives

$$v_2\{AA-pp\}(p_T) \ = \ \frac{\langle Q_2 u^*_{2,i}(p_T)\rangle_{AA} - \langle Q_2 u^*_{2,i}(p_T)\rangle_{pp}}{2\sqrt{\langle Q_2^A Q_2^{B*}\rangle_{AA}}} \tag{3.21}$$

because $2\sqrt{\langle Q_2^A Q_2^{B*}\rangle_{AA}} = 2\sqrt{(M/2)\overline{v_2}(M/2)\overline{v_2}} = M\overline{v_2}$.

Comparing p+p and AA collisions, one might expect some changes in particle correlations: there could be an increase in correlations due to a possible increase of jet multiplicities in AA collisions or, conversely, some decrease due to the suppression of high p_T back-to-back correlations [Adl03a]. It is difficult to make an accurate estimate of the possible uncertainties. The fact that at high p_T ($p_T > 5$ GeV/c) the p+p results are very close to central Au+Au [Ada04b, Ada05c] suggests that the uncertainties are relatively small. In the following, we use $v_2\{AA-pp, \mathrm{TPC}\}$ and $v_2\{AA-pp, \mathrm{FTPC}\}$ to denote $v_2\{AA-pp\}$ calculated with TPC and FTPC flow vectors, respectively.

Non-flow is one of the largest uncertainties in elliptic flow measurements. As we mentioned above, this effect can be investigated by comparing the azimuthal correlations measured in Cu+Cu collisions to those in p+p collisions. The event average of the sum of the correlations is given by Eq. (3.19).

Figure 3.10 shows the azimuthal correlation, Eq. (3.19), as a function of p_T for the $0-60\%$ centrality range in Cu+Cu collisions at $\sqrt{s_{NN}}$ = 200 GeV, compared to p+p collisions. As we can see, the azimuthal correlations in Cu+Cu collisions, shown as solid squares, increase with p_T and then saturate above 2 GeV/c while those in p+p collisions, shown as open squares, monotonically increase with p_T in the case of the TPC flow

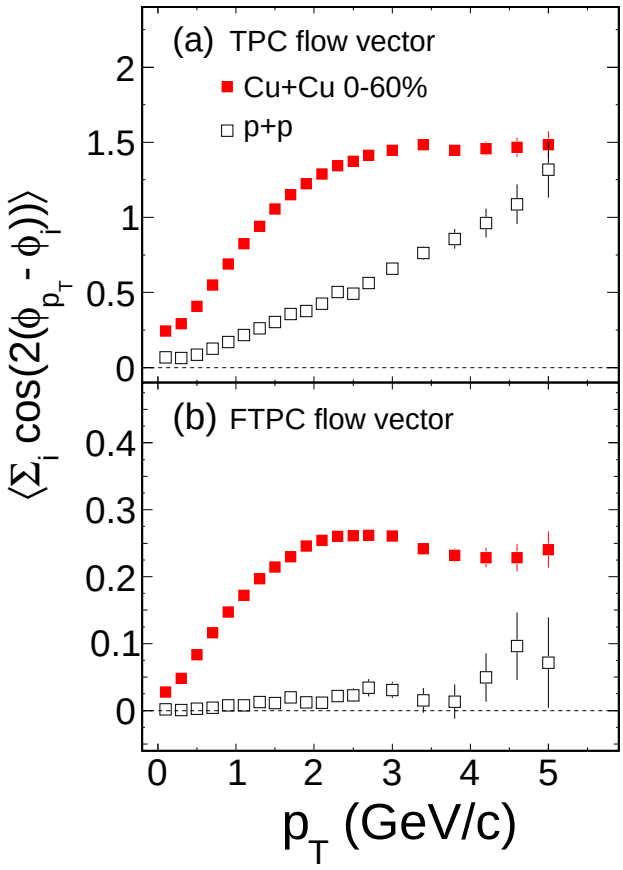

Figure 3.10: Charged hadron azimuthal correlations as a function of p_T in $\sqrt{s_{NN}} = 200$ GeV 60% most central Cu+Cu collisions (closed squares) compared to those from $\sqrt{s_{NN}} = 200$ GeV p+p collisions (open squares). Flow vector calculated from (a) TPC tracks, (b) FTPC tracks.

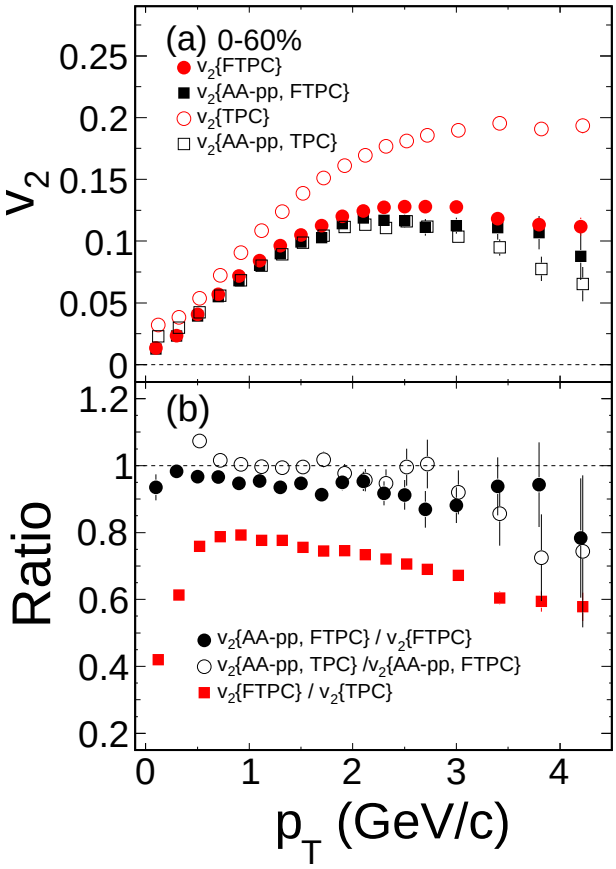

Figure 3.11: (a) Charged hadron $v_2(p_T)$ in $\sqrt{s_{NN}} = 200$ GeV $0-60\%$ Cu+Cu collisions. Open circles, closed circles, open squares and closed squares represent the results of v_2 as a function of p_T measured by the TPC flow vector ($v_2\{\text{TPC}\}$), the FTPC flow vector ($v_2\{\text{FTPC}\}$), the TPC and FTPC flow vector with subtracting the azimuthal correlations in p+p collisions ($v_2\{AA-pp, \text{TPC}\}$, $v_2\{AA-pp, \text{FTPC}\}$). (b) The ratio of the results for the various methods described in (a).

vector. With the flow vector determined from FTPC tracks the azimuthal correlations around midrapidity in p+p collisions are small when p_T is less than 4 GeV/c. It means that one strongly reduces the non-flow effects with the FTPC flow vector relative to the one seen with the TPC flow vector.

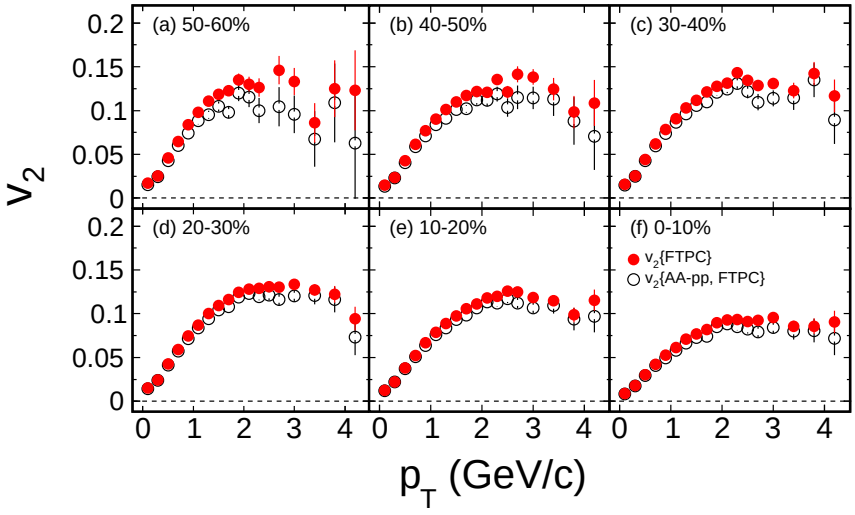

Figure 3.12: Charged hadron $v_2\{\text{FTPC}\}$ (closed circles) and $v_2\{AA-pp,\text{FTPC}\}$ (open circles) as a function of p_T in $\sqrt{s_{NN}}$ = 200 GeV Cu+Cu collisions for centrality bins: (a) $50-60\%$, (b) $40-50\%$, (c) $30-40\%$, (d) $20-30\%$, (e) $10-20\%$ and (f) $0-10\%$. The percentages refer to fraction of most central events.

In order to illustrate the sensitivity to non-flow for the various flow analysis methods, we first analyzed $h^{\pm}$ elliptic flow in the 60% most central Cu+Cu collisions at $\sqrt{s_{NN}}$ = 200 GeV. As shown in Fig. 3.11 (a), the fact that $v_2\{\text{TPC}\}$ is significantly larger than $v_2\{\text{FTPC}\}$ indicates a larger non-flow effect in $v_2\{\text{TPC}\}$. With the large η gap between West and East FTPCs, non-flow effects due to the short-range correlations are reduced in $v_2\{\text{FTPC}\}$. $v_2\{\text{FTPC}\}$ saturates at $p_T \sim 2.5$ GeV/c and then falls off slightly up to $p_T \sim 4$ GeV/c. In order to estimate the remaining non-flow effects in $v_2\{\text{FTPC}\}$, we subtract the azimuthal correlations of p+p collisions from those in Cu+Cu collisions according to Eq. (3.21). In Fig. 3.11 (a), $v_2\{AA-pp,\text{FTPC}\}$ is close to $v_2\{\text{FTPC}\}$ in the region $p_T < 4$ GeV/c. To quantitatively illustrate non-flow systematic uncertainties, Fig. 3.11 (b) shows the ratios of $v_2\{AA-pp,\text{FTPC}\}$ to $v_2\{\text{FTPC}\}$, $v_2\{AA-pp,\text{TPC}\}$ to $v_2\{AA-pp,\text{FTPC}\}$ and $v_2\{\text{FTPC}\}$ to $v_2\{\text{TPC}\}$ as

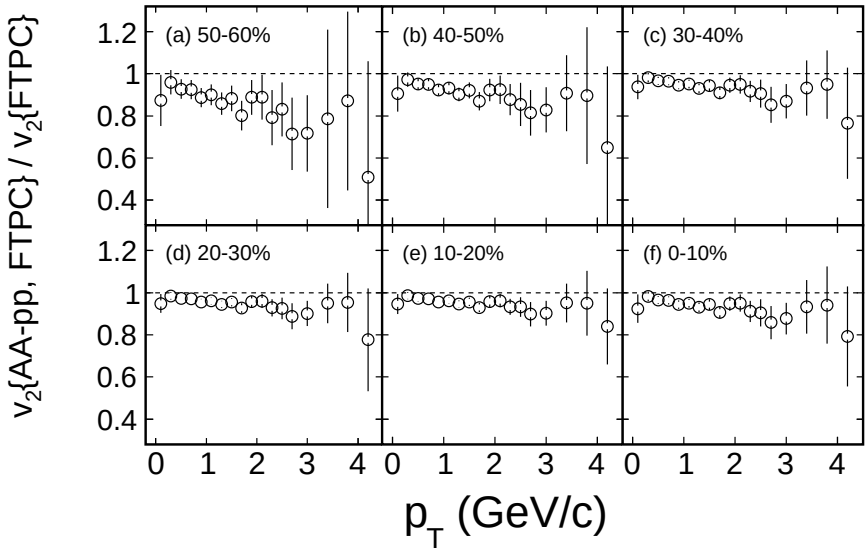

Figure 3.13: Ratios of $v_2\{AA-pp, \mathrm{FTPC}\}/v_2\{\mathrm{FTPC}\}$ for charged hadron as a function of p_T in $\sqrt{s_{NN}}$ = 200 GeV Cu+Cu collisions for centrality bins: (a) $50-60\%$, (b) $40-50\%$, (c) $30-40\%$, (d) $20-30\%$, (e) $10-20\%$ and (f) $0-10\%$. The percentages refer to fraction of most central events.

a function of p_T. $v_2\{\mathrm{FTPC}\}/v_2\{\mathrm{TPC}\}$ shows that non-flow in $v_2\{\mathrm{TPC}\}$ increases from 20% at $p_T \sim 0.8$ GeV/c to 40% at $p_T \sim 3.5$ GeV/c. Based on the comparison between $v_2\{AA-pp, \mathrm{FTPC}\}$ and $v_2\{\mathrm{FTPC}\}$, the residual non-flow in $v_2\{\mathrm{FTPC}\}$ is less than 10% below $p_T \sim 4$ GeV/c. We also checked the $v_2\{AA-pp\}$ calculated with the TPC flow vector. Beyond $p_T \sim 3$ GeV/c, $v_2\{AA-pp, \mathrm{TPC}\}$ seems systematically lower, but within errors it is similar to $v_2\{AA-pp, \mathrm{FTPC}\}$. This shows that most of the non-flow is eliminated by subtracting the azimuthal correlation in p+p collisions, validating our earlier assumption.

To illustrate the centrality dependence of the systematic uncertainties, Fig. 3.12 shows $v_2\{\mathrm{FTPC}\}$ and $v_2\{AA-pp, \mathrm{FTPC}\}$ as a function of p_T for six centrality bins. Ratios of $v_2\{AA-pp, \mathrm{FTPC}\}$ to $v_2\{\mathrm{FTPC}\}$ for each centrality bin are shown in Fig. 3.13 from (a) the most peripheral bin $50-60\%$ to (f) the most central bin $0-10\%$. For each centrality bin, the ratio falls off slightly as p_T increases. For the two peripheral bins $50-60\%$ and $40-50\%$, the ratios drop faster than in the other bins, indicating larger non-flow contributions in $v_2\{\mathrm{FTPC}\}(p_T)$ in peripheral Cu+Cu collisions. Figure 3.14

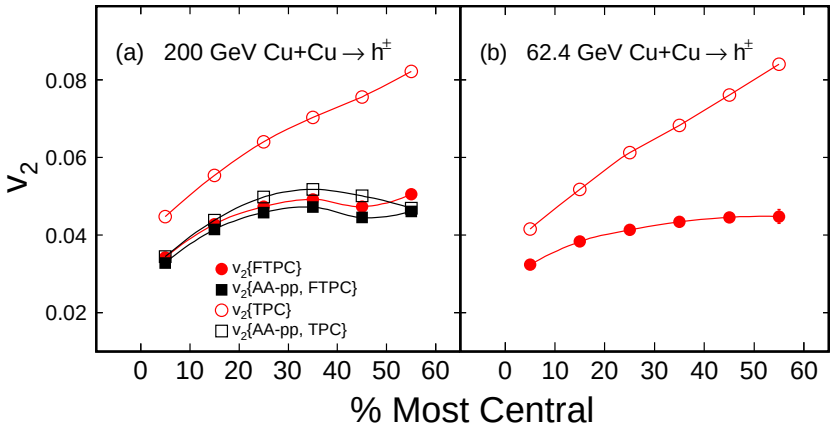

Figure 3.14: Charged hadron v_2 integrated over p_T and η vs. centrality for the various methods described in the text in $\sqrt{s_{NN}} = 200$ GeV and 62.4 GeV Cu+Cu collisions.

shows charged hadron v_2 integrated over p_T ($0.15 < p_T < 4$ GeV/c) and η ($|\eta| < 1.0$) vs. centrality for the various methods. It is clear that $v_2\{\text{TPC}\}$ is much higher than for the other methods, especially for the peripheral collisions.

To summarize the non-flow systematics we employed the Scalar Product method with TPC and FTPC flow vectors for $h^{\pm}$ in Cu+Cu collisions at $\sqrt{s_{NN}} = 200$ GeV. The results for the 60% most central events are shown in Fig. 3.11. $v_2\{\text{TPC}\}$ has large non-flow contributions while $v_2\{\text{FTPC}\}$ eliminates most of the non-flow. In what follows, we will report our results in term of $v_2\{\text{FTPC}\}$. For simplicity v_2 denotes $v_2\{\text{FTPC}\}$ except when the flow method is explicitly specified. With the assumption of pure non-flow effects in p+p collisions, we use $v_2\{AA-pp, \text{FTPC}\}$ to estimate non-flow systematic errors in $v_2\{\text{FTPC}\}$. Ratios of $v_2\{AA-pp, \text{FTPC}\}$ to $v_2\{\text{FTPC}\}$ are shown for the 60% most central events in Fig. 3.11 (b) and six centrality bins in Fig. 3.13. The ratios show that non-flow effects increase with p_T for all centrality bins and non-flow effects are larger in more peripheral bins. The non-flow systematic error is 5% for $0-40\%$ collisions and 10% for $40-60\%$ collisions. For K^0_S, ϕ, Λ and Ξ v_2, we assume a similar magnitude of non-flow contributions.

The non-flow systematic uncertainty for strange hadron in Au+Au collisions at $\sqrt{s_{NN}}$

= 200 GeV has been discussed in [Abe08a]. The systematic errors between Event Plane method (the TPC event plane) and Lee-Yang Zero method are in order of 10%. Also, for simplicity v_2 denotes $v_2\{\text{TPC}\}$ in Au+Au collisions except when the flow method is explicitly specified.

CHAPTER 4

Results

In this chapter, we present the measurements of v_2 at mid-rapidity $|Y| < 1$ ($|\eta| < 1$ for charged hadrons) from Cu+Cu and Au+Au collisions. v_2 results are presented for strange hadrons (K^0_S, Λ and Ξ) in Cu+Cu collisions at $\sqrt{s_{NN}} = 200$ GeV, for charged hadrons in Cu+Cu collisions at $\sqrt{s_{NN}} = 200$ and 62.4 GeV, for π, p, K^0_S, Λ, ϕ, Ξ and Ω in Au+Au collisions at $\sqrt{s_{NN}} = 200$ GeV, for charged hadrons in Au+Au collisions at $\sqrt{s_{NN}} = 9.2$ GeV.

4.1 Transverse Momentum Dependence of v_2 in Minibias Events

Figure 4.1 shows minimum bias v_2 for K^0_S, Λ and Ξ at mid-rapidity $|Y| < 1$ ($|\eta| < 1$ for charged hadrons) in Cu+Cu collisions at $\sqrt{s_{NN}} = 200$ GeV. The circles, squares, upper triangles and lower triangles represent K^0_S, Λ, Ξ and charged hadrons, respectively. The error bars are statistical errors. The strange hadrons v_2 is measured up to $p_T \sim 4$ GeV/c. Strange hadrons and charged hadrons v_2 increase with p_T and then saturate at higher p_T. At low p_T ($p_T < 1.5$ GeV/c), the heavier Λ has smaller v_2 than the lighter K^0_S. At intermediate p_T ($2 < p_T < 4$ GeV/c), Λ v_2 is greater than K^0_S.

Figure 4.2 shows minimum bias v_2 for π, p, K^0_S, Λ, ϕ, Ξ and Ω at mid-rapidity $|Y| < 1$ in Au+Au collisions at $\sqrt{s_{NN}} = 200$ GeV. A clear mass ordering can be seen when $p_T < 2$ GeV/c. Beyond this p_T region ($p_T > 2$ GeV/c), all particles are grouped according to hadron type (baryon or meson), and the v_2 of baryon group is greater than that of meson.

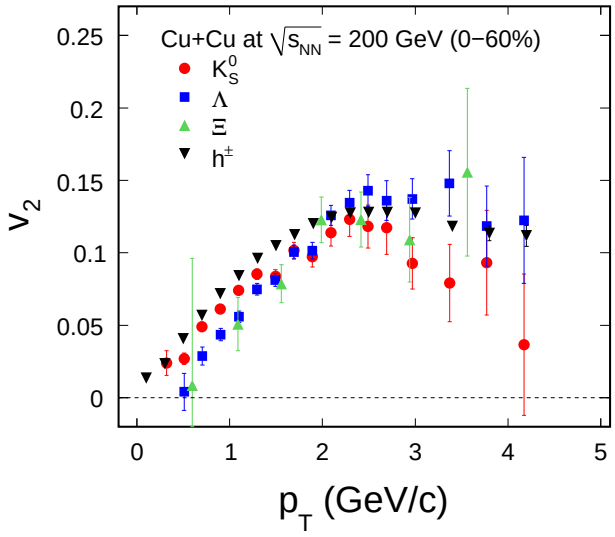

Figure 4.1: Elliptic flow (v_2) as a function of transverse momentum (p_T) at mid-rapidity $|Y| < 1$ ($|\eta| < 1$ for charged hadrons) for minimum bias ($0 - 60\%$ geometrical cross section) in Cu+Cu collisions at $\sqrt{s_{NN}} = 200$ GeV. The error bars are statistical errors.

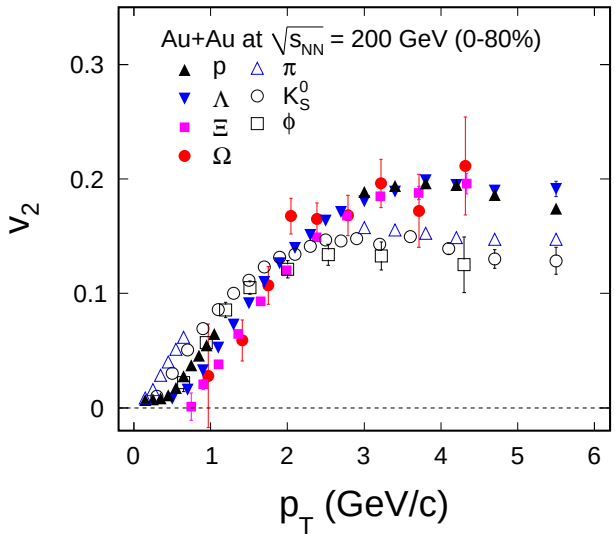

Figure 4.2: Elliptic flow (v_2) as a function of transverse momentum (p_T) at mid-rapidity $|Y| < 1$ for minimum bias ($0 - 80\%$ geometrical cross section) in Au+Au collisions at $\sqrt{s_{NN}}$ = 200 GeV. The error bars are statistical errors.

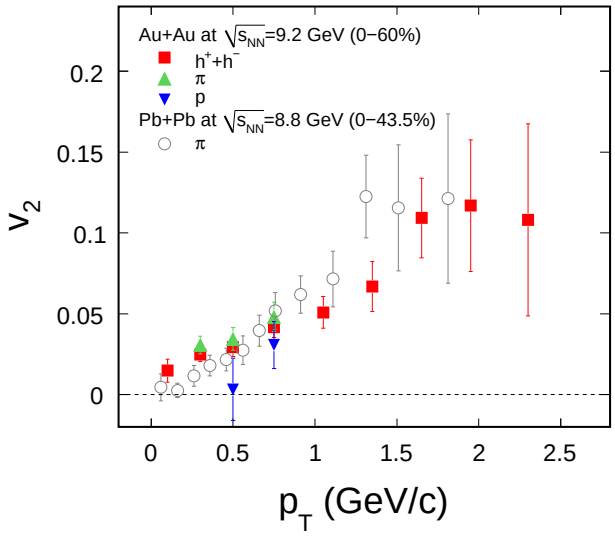

Figure 4.3: Elliptic flow (v_2) as a function of transverse momentum (p_T) at mid-rapidity $|Y| < 1$ ($|\eta| < 1$ for charged hadrons) for minimum bias ($0 - 60\%$ geometrical cross section) in Au+Au collisions at $\sqrt{s_{NN}} = 9.2$ GeV. For comparison, v_2 (p_T) results for π (open circles) from NA49 [Alt03a] in $0 - 43.5\%$ Pb+Pb collisions at $\sqrt{s_{NN}} = 8.8$ GeV, are also shown. The error bars are statistical errors.

With 3 k events collected using STAR detector from a test run of the collider in the year 2008, we present the results of an elliptic flow analysis of Au+Au collisions at $\sqrt{s_{NN}} = 9.2$ GeV. Figure 4.3 shows minimum bias v_2 for π, p and charged hadrons at mid-rapidity $|Y| < 1$ ($|\eta| < 1$ for charged hadrons). Within error bars, it is consistent with the results of NA49 at the similar beam energy and system size. It indicates the capabilities of the STAR detector to pursue the proposed beam energy scan [Abe10a].

4.2 Centrality Dependence of v_2

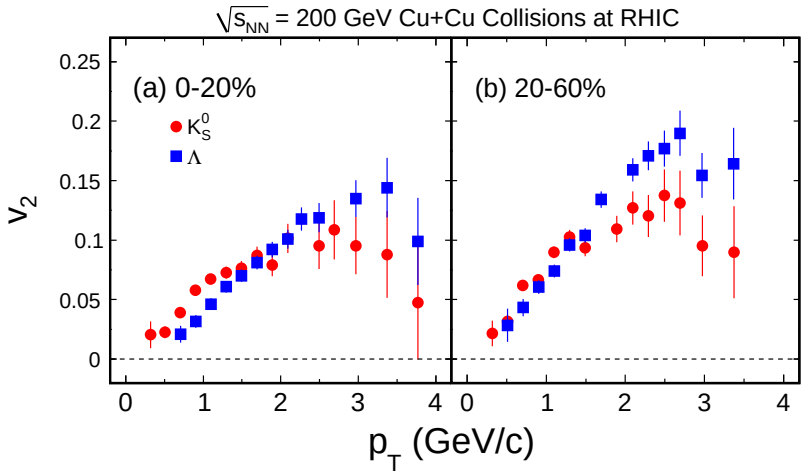

Figure 4.4: v_2 of K^0_S and Λ as a function of p_T for $0-20\%$ and $20-60\%$ centrality bins in Cu+Cu collisions at $\sqrt{s_{NN}} = 200$ GeV.

Figure 4.4 shows v_2 of K^0_S and Λ as a function of p_T at mid-rapidity for Cu+Cu collisions at $\sqrt{s_{NN}} = 200$ GeV for (a) $0-20\%$ and (b) $20-60\%$. Symbols and errors are presented in the same way as minimum bias data in Figure 4.1. The p_T dependence of v_2 is similar in these two centrality bins: v_2 increases at low p_T, and then saturates at intermediate p_T. The mass ordering ($p_T < 2$ GeV/c) and the hadron type dependence ($p_T > 2$ GeV/c) can be observed. The values of v_2 in peripheral collisions is larger than that in central collisions.

Centrality dependence of $v_2(p_T)$ for charged hadrons in Cu+Cu collisions at $\sqrt{s_{NN}} =$

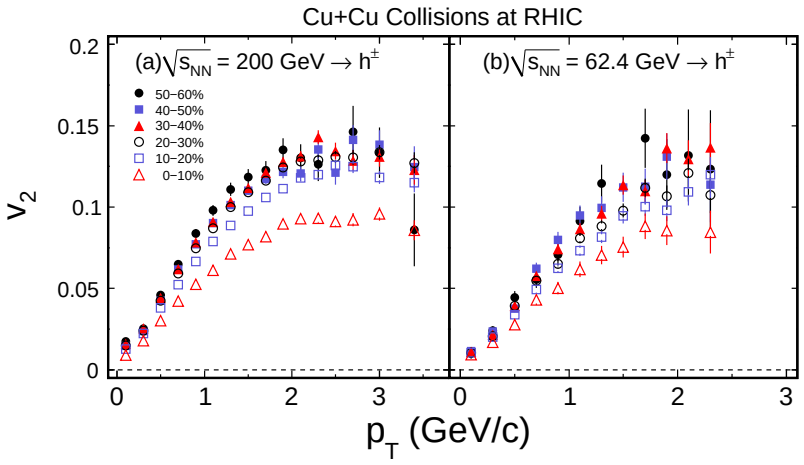

Figure 4.5: Charged hadron v_2 as function of p_T for $50-60\%$ (solid circles), $40-50\%$ (solid squares), $30-40\%$ (solid triangles), $20-30\%$ (open circles), $10-20\%$ (open squares) and $0-10\%$ (open triangles) in $\sqrt{s_{NN}} = 200$ GeV and 62.4 GeV Cu+Cu collisions.

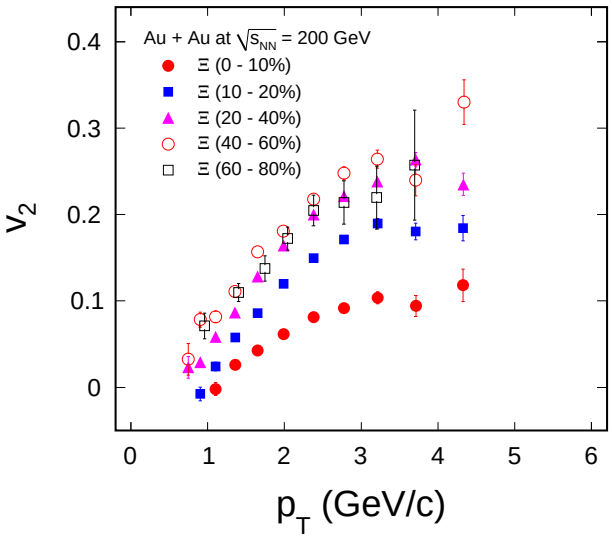

Figure 4.6: Ξ v_2 as function of p_T for $60-80\%$, $40-60\%$, $20-40\%$, $10-20\%$, and $0-10\%$ in $\sqrt{s_{NN}} = 200$ GeV Au+Au collisions.

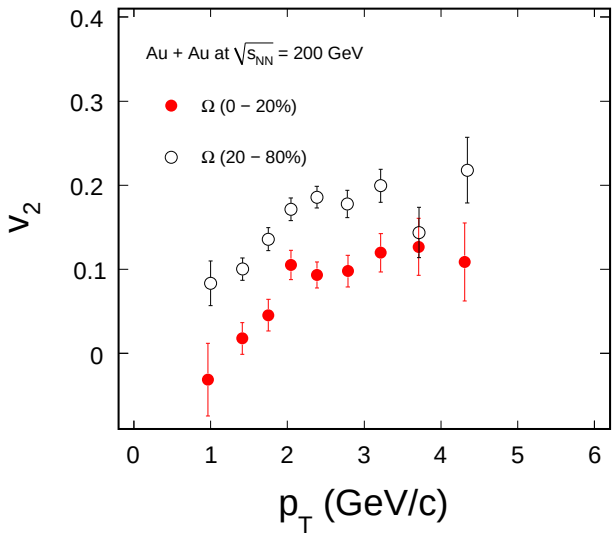

Figure 4.7: Ω v_2 as function of p_T for $20-80\%$ and $0-20\%$ in $\sqrt{s_{NN}}$ = 200 GeV Au+Au collisions.

200 GeV and 62.4 GeV are shown in Figure 4.5. The observed trend is that v_2 increases with p_T, reaches its maximum and then slightly decreases. The magnitude of v_2 increase from central to peripheral collisions.

With the large statistics in run VII, we can measured the v_2 for multi-strange hadron much more precisely. Figure 4.6 to 4.7 show the centrality dependence of $v_2(p_T)$ for $\Xi^- + \overline{\Xi}^+$ and Ω in Au+Au collisions at $\sqrt{s_{NN}}$ = 200 GeV. We divide all events into five centrality intervals for $\Xi^- + \overline{\Xi}^+$, from the top 10% to $60-80\%$ peripheral collisions. For Ω, the results are from $0-20\%$ and $20-80\%$ centrality bins. The magnitude of v_2 is smaller in the more central collisions, which is similar to the results of charge hadrons [Bai07a].

4.3 p_T-integrated v_2 for Strange Hadron

Average v_2 over measured p_T range, which we denote $\langle v_2 \rangle$ are calculated as

$$\langle v_2 \rangle = \frac{\int_0^\infty dp_T dN/dp_T \times v_2(p_T)}{\int_0^\infty dp_T dN/dp_T} = \frac{\sum_i dN^i/dp_T \times v_2^i(p_T)}{\sum_i dN^i/dp_T} \tag{4.1}$$

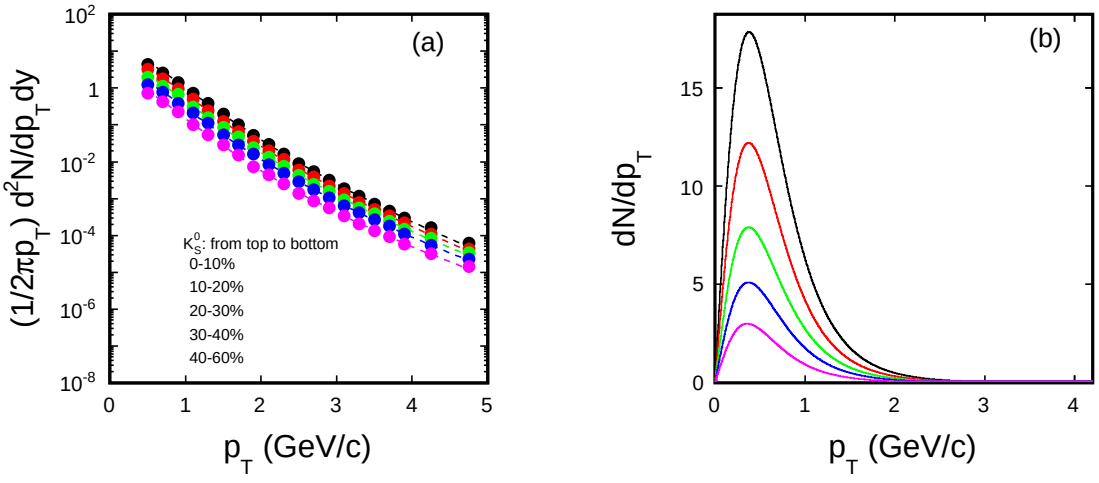

Figure 4.8: The p_T spectra and dN/dp_T distribution for K^0_S from central (top) to peripheral (bottom) collisions. Dashed lines in panel (a) represent fitting results by Eq. 4.2. The curves in panel (b) have been scaled for clarity.

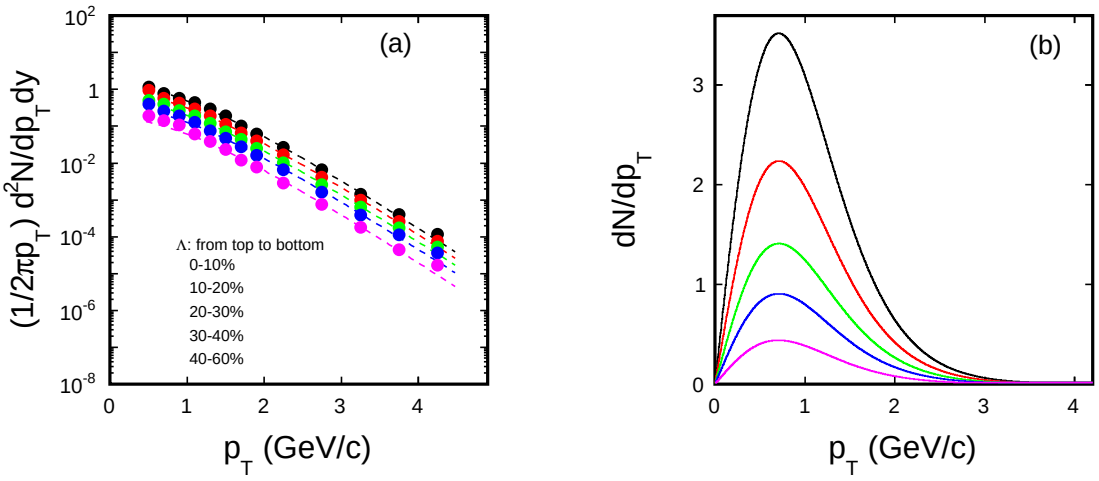

Figure 4.9: The p_T spectra and dN/dp_T distribution for Λ from central (top) to peripheral (bottom) collisions. Dashed lines in panel (a) represent fitting results by Eq. 4.3. The curves in panel (b) have been scaled for clarity.

Where dN/dp_T is the transverse momentum distributions, and $v_2(p_T)$ is the differential v_2 as a function of p_T. Since we measure both spectra and v_2 in the limited p_T, the integral in Eq. 4.1 are replaced to the sum of data points in the third term, We estimate v_2 and dN/dp_T for lower p_T range by extrapolating the fitting results to $p_T \to 0$. Higher p_T range are also extrapolated for both v_2 and dN/dp_T but they do not contribute the $\langle v_2 \rangle$ for all particle species, thus we just integrate the results up to the maximum of measured p_T.

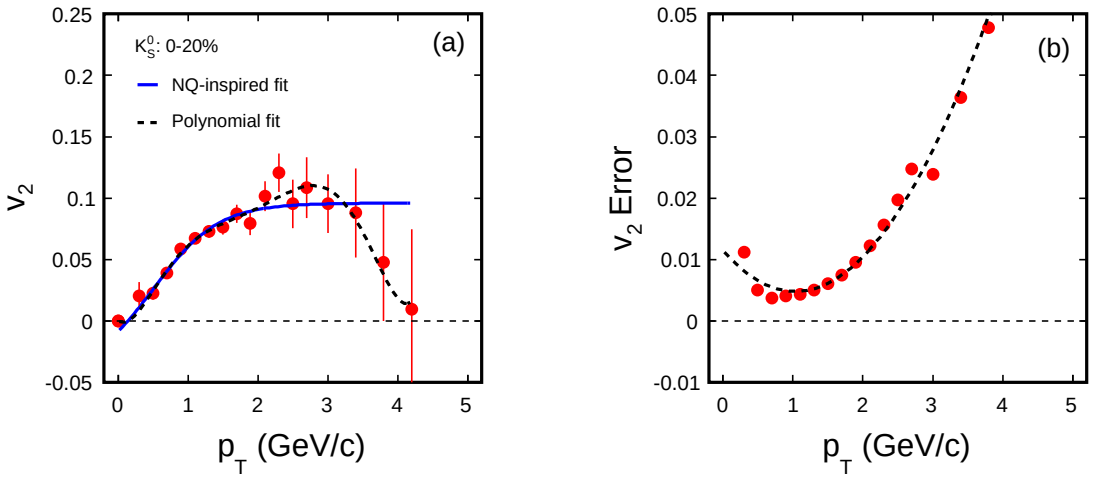

Figure 4.10: $v_2(p_T)$ for K^0_S in $0-20\%$ centrality bin. (a) Fitting results for $v_2(p_T)$ by polynomial and Eq. 4.4, (b) A polynomial fit to v_2 errors.

Fig. 4.8 - 4.9 show transverse momentum spectra for K^0_S and Λ as a function of centrality. We parameterize the p_T spectra by the following functions:

$$f^{K^0_S}(p_T) = A \cdot (1 + \frac{\sqrt{p_T^2 + m_0^2} - m_0}{nT})^{-n} \tag{4.2}$$

$$f^{\Lambda} = A \cdot \sqrt{p_T^2 + m_0^2} \cdot e^{-\frac{\sqrt{p_T^2+m_0^2}-m_0}{T}} \tag{4.3}$$

Where A, n, T are the free parameters.

Fig. 4.10 - 4.11 show the fitting results of $v_2(K^0_S)$ and $v_2(\Lambda)$ as a function of p_T for $0-20\%$ centrality bin. To extrapolate the data to low and high p_T, we use polynomials

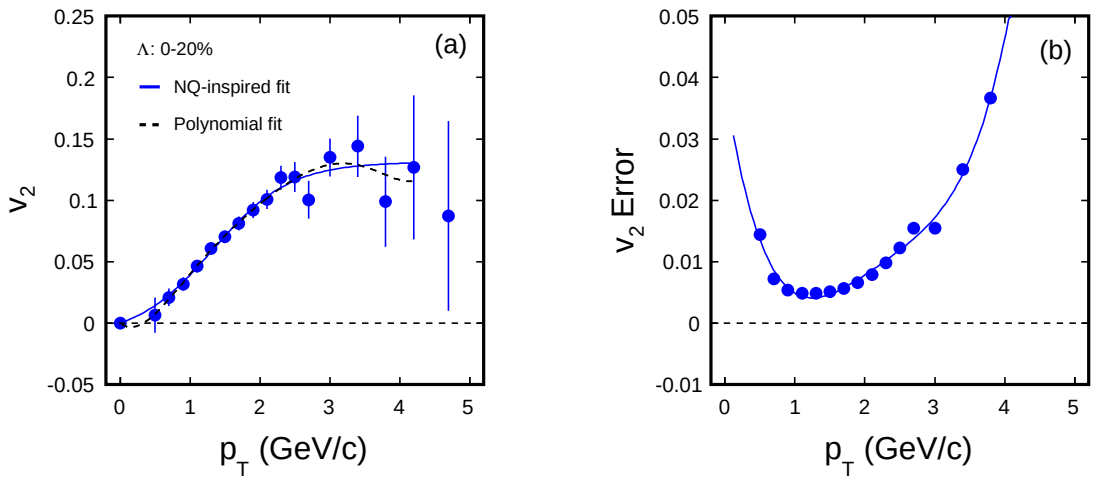

Figure 4.11: $v_2(p_T)$ for Λ in $0-20\%$ centrality bin. (a) Fitting results for $v_2(p_T)$ by polynomial and Eq. 4.4, (b) A polynomial fit to v_2 errors.

and Eq. 4.4

$$f_{v_2}(n) = \frac{an}{1 + e^{-(p_T/n-b)/c}} - dn \tag{4.4}$$

The errors of v_2 are fitted by polynomials. The fit from Eq. 4.4 (n_q-inspired fit) is used for value, and the difference of $\langle v_2 \rangle$ obtained with n_q-inspired fit and polynomial fit is quoted as systematic error.

	K^0_S			Λ		
Centrality	$\langle v_2 \rangle$	Stat. error	Sys. error	$\langle v_2 \rangle$	Stat. error	Sys. error
$0-20\%$	0.035	0.00265	0.0036	0.0403	0.00298	0.0023
$20-60\%$	0.045	0.00266	0.0010	0.0670	0.00530	0.0013

Table 4.1: Strange hadron (K^0_S and Λ) elliptic flow integrated over p_T ($p_T < 4.0$ GeV/c) and y ($y < 1.0$) in Cu+Cu collisions at $\sqrt{s_{NN}} = 200$ GeV.

Results for K^0_S and Λ in $\sqrt{s_{NN}} = 200$ GeV Cu+Cu collisions are summarized in Table. 4.1. Due to the statistics, we only extracted the integrated v_2 from two centrality bins. Fig. 4.12 shows the results for K^0_S, Λ and Ξ in $\sqrt{s_{NN}} = 200$ GeV Au+Au collisions. For Ξ, we followed the similar procedures applied to Λ to extract the integrated v_2. The errors are total statistical and systematic uncertainties added in quadrature.

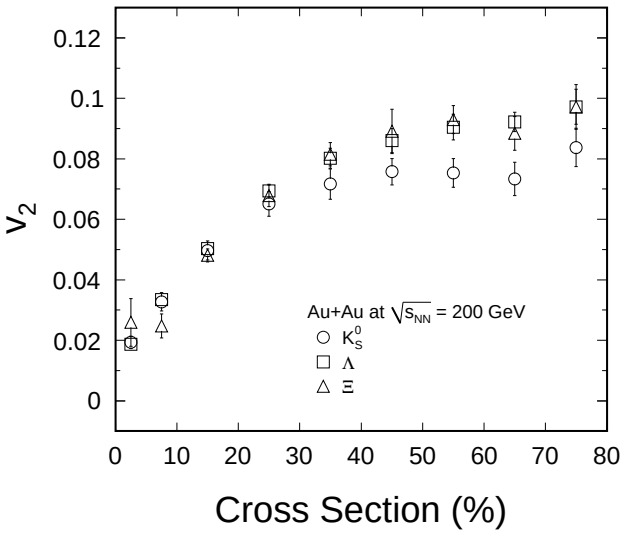

Figure 4.12: Strange hadron (K^0_S, Λ and Ξ) elliptic flow integrated over p_T ($p_T < 4.0$ GeV/c) and y ($y < 1.0$) in Au+Au collisions at $\sqrt{s_{NN}} = 200$ GeV.

CHAPTER 5

Discussion

This chapter is organized in the following way: in Section 1, we discuss the partonic collectivity at RHIC; in Section 2, we compare the experimental data to the ideal hydro calculations; in Section 3, we address the thermalization question through the system and centrality dependence of v_2; in Section 4, we investigate whether the top energy RHIC data reach the ideal hydro limit by applying a two parameter fit (Knudsen No. fit) to v_2/ε as function of particle density, the extracted Knudsen No. is also used to estimate η/s.

5.1 Partonic Collectivity

Quark coalescence [Mol03a] or recombination [Hwa03b, Fri03a] mechanisms in particle production predict that at intermediate p_T ($2 < p_T < 5$ GeV/c) Number of Quark (NQ) scaled v_2 will follow a universal curve. Thus, the NQ scaling is considered evidence for partonic degrees of freedom.

In Figure 5.1, we systematically discuss the NQ scaling at RHIC. The available data are from Au+Au and Cu+Cu colliding systems. The top beam energy is $\sqrt{s_{NN}} = 200$ GeV; we also have data from relatively lower beam energy $\sqrt{s_{NN}} = 62.4$ GeV, which can be used to study the energy dependence of NQ scaling. Figure 5.1(a) shows the results for all strange hadrons including the pure multi-strange hadrons ϕ and Ω. All data are from Run VII. With the large statistics, we can measure the v_2 much more precisely than before, especially for multi-strange hadrons. Figure 5.1(b) shows the results for K^0_S, Λ and Ξ in Cu+Cu collisions at $\sqrt{s_{NN}} = 200$ GeV. The data in Figure 5.1(c) are

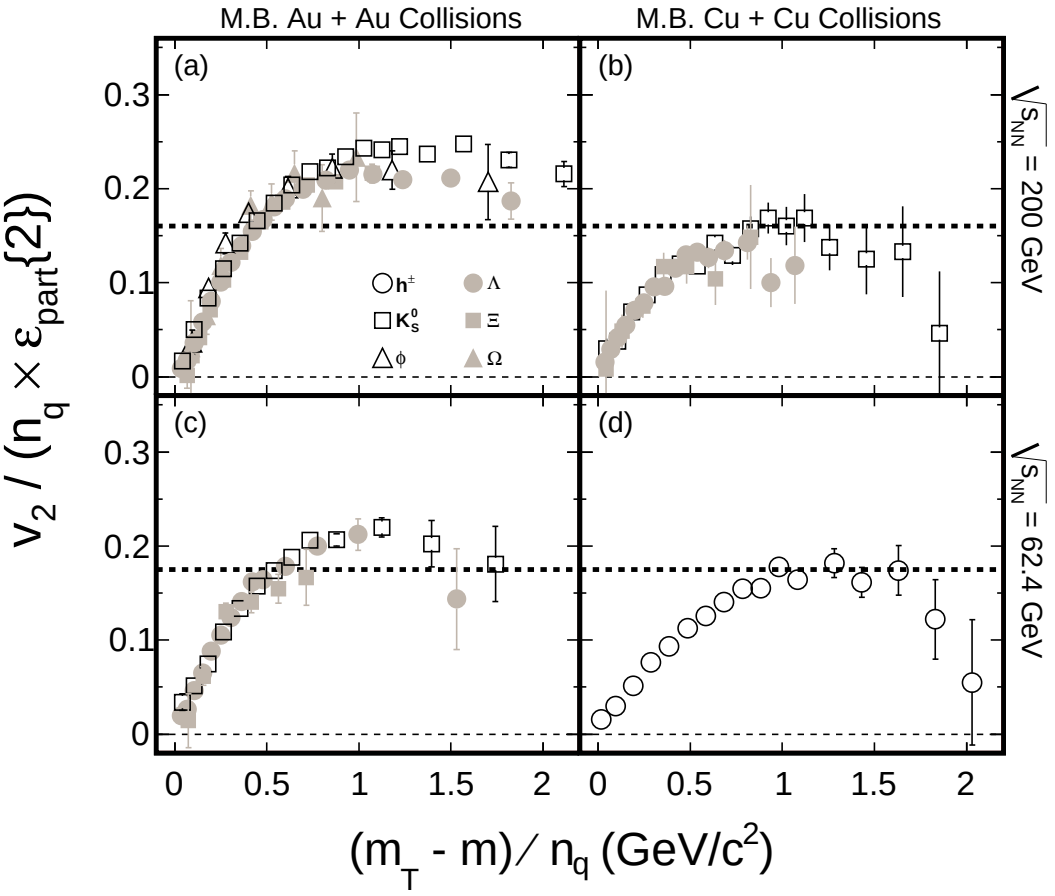

Figure 5.1: Number of Quark (NQ) and participant eccentricity scaled v_2 as a function of transverse energy $(m_T - m)$ divided by NQ for (a) Au+Au at $\sqrt{s_{NN}} = 200$ GeV, (b) Cu+Cu at $\sqrt{s_{NN}} = 200$ GeV, (c) Au+Au at $\sqrt{s_{NN}} = 62.4$ GeV and (d) Cu+Cu at $\sqrt{s_{NN}} = 62.4$ GeV minimum bias events. Open circles, squares, triangles and solid circles, squares, triangles represent charged hadrons, K^0_S, ϕ, Λ, Ξ and Ω, respectively. The error bars on the data points represent statistical uncertainties.

from the STAR publication [Abe07a]. Due to limited statistics, only charged hadron results are shown in Figure 5.1(d) for Cu+Cu collisions at $\sqrt{s_{NN}} = 62.4$ GeV. We set the mass of charged hadron equal to that of π. In order to remove the initial geometry, v_2 is scaled by eccentricity. The participant eccentricity is the initial configuration space eccentricity of the participants which is defined by [Bac07a]

$$\varepsilon_{\rm part} = \frac{\sqrt{(\sigma_y^2 - \sigma_x^2) + 4(\sigma_{xy}^2)}}{\sigma_y^2 + \sigma_x^2} \tag{5.1}$$

In this formula, $\sigma_x^2 = \langle x^2 \rangle - \langle x \rangle^2$, $\sigma_y^2 = \langle y^2 \rangle - \langle y \rangle^2$ and $\sigma_{xy} = \langle xy \rangle - \langle x \rangle \langle y \rangle$, with x, y being the position of the participating nucleons in the transverse plane. The root mean square of the participant eccentricity

$$\varepsilon_{\rm part}\{2\} = \sqrt{\langle \varepsilon_{\rm part}^2 \rangle} \tag{5.2}$$

is calculated from the Monte Carlo Glauber model [Mil03b, Mil07a] and Color Glass Condensate (CGC) model [Dre05a, Dre07a, Dre07b, Dre09a]. (See Table 5.1 for $\varepsilon_{\rm part}\{2\}$.) Since the event plane is constructed from the hadrons which have their origin in participant nucleons, what we actually measure is the root mean square of v_2 with respect to the participant plane [Pos09a] when the event plane resolution is less than 0.2. In this case, $\varepsilon_{\rm part}\{2\}$ is the appropriate measure of the initial geometric anisotropy taking the event-by-event fluctuations into account [Vol06a, Alv08a, Pos09a].

In Figure 5.1, Glauber model has been used to calculate the eccentricities, but it is similar in the case of CGC model. The conclusions from Figure 5.1 are as follows:

(i) There is a clear number of quark (NQ) scaling for all systems and beam energies studied here. (Due to the limited statics, this test is not done for Cu+Cu collisions at $\sqrt{s_{NN}} = 62.4$ GeV.) It indicate the partonic collectivity has been built up at RHIC.

(ii) After removing the initial geometry by eccentricity, stronger collective flow can be observed in the larger system.

In particularly, in Figure 5.2, we compare the elliptic flow of protons and pions to that of the multi-strange hadrons Ω and ϕ. (These hadrons have valence quark content $sss(\overline{sss})$ and $(\overline{s}s)$ respectively.) The important point is that the Ω is nearly

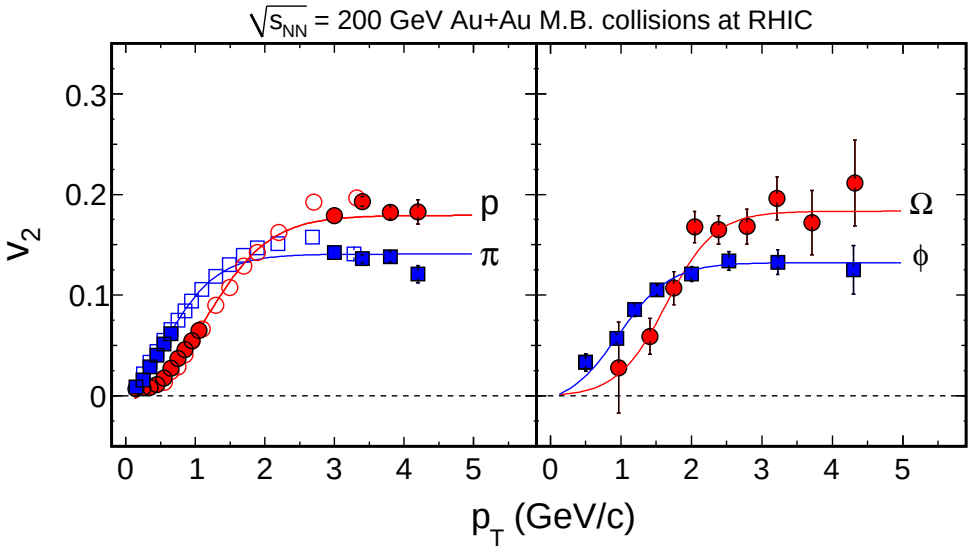

Figure 5.2: v_2 as function of p_T for π, p (left) and ϕ, Ω (right) in Au + Au minimum-bias collisions at $\sqrt{s_{NN}} = 200$ GeV. Open symbols represent results from PHENIX [Iss06a]. Lines represent NQ-inspired fit [Don04a].

twice as heavy as the proton and more importantly, both Ω and ϕ are less sensitive to the hadronic process [Sho85a, Hec98a, Bas99b, Che03a, Bia81a, Mul72a]. Nevertheless they show nearly the same elliptic flow as the protons and pions. This provides fairly convincing evidence that the majority of the elliptic flow develops during the partonic process. Thus, it directly points to partonic collectivity at RHIC.

5.2 Ideal Hydrodynamics Test

The results for π, p, K^0_S, Λ, Ξ, and Ω are shown in Figure 5.3 for various centralities of Au+Au collisions at $\sqrt{s_{NN}} = 200$ GeV. Shown are results for minimum bias and three other centrality bins. All $v_2(p_T)$ results are from the event plane method. The systematic uncertainties extracted from PID cuts, background subtractions, and combining centralities are shown as shaded bars in the figure. The systematic uncertainty in the method itself is not included. The shaded band in figure 5.3(c) indicates the nonflow systematic uncertainties for K^0_S and Λ for the $10-40\%$ centrality bin.

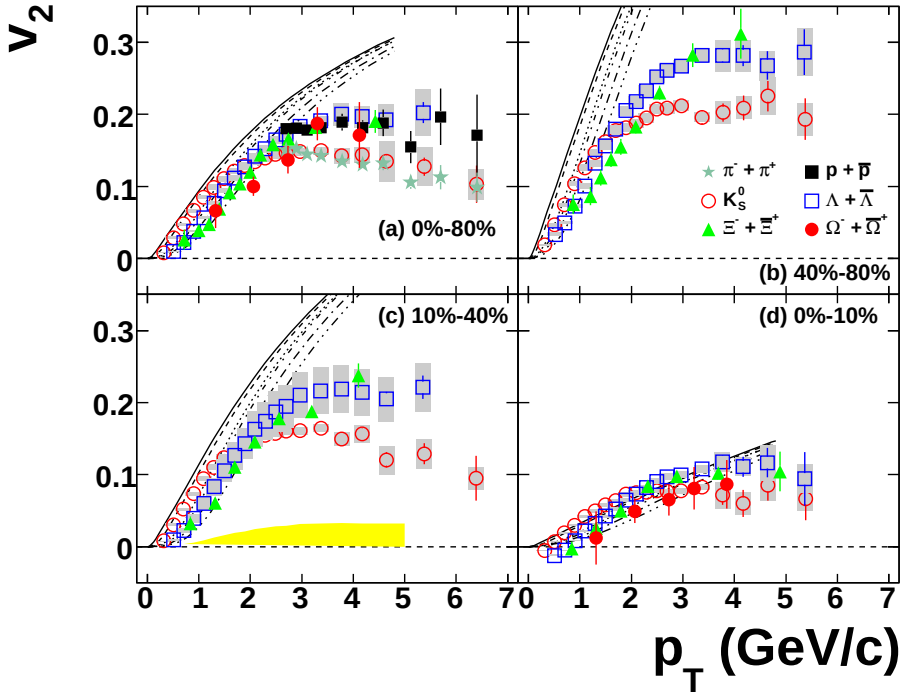

Figure 5.3: v_2 of K^0_S (open circles), Λ (open squares), Ξ (filled triangles), and Ω (filled circles) as a function of p_T for (a) $0-80\%$, (b) $40-80\%$, (c) $10-40\%$, and (d) $0-10\%$ in Au+Au collisions at $\sqrt{s_{NN}} = 200$ GeV. The error bars represent statistical uncertainties. The bands on the data points represent systematic uncertainties as discussed in the text. For comparison, π (stars) and p (filled squares) results are shown in (a). The systematic uncertainty of nonflow for K^0_S and Λ for $10-40\%$ (c) is plotted as a shaded band near 0. For comparison, results from ideal hydrodynamic calculations [Huo06a, Huo06b] are shown: at a given p_T, from top to bottom, the lines represent the results for π, K, p, Λ, Ξ, and Ω. The figure is from [Abe08a].

The results from an ideal hydrodynamic model [Huo06a, Huo06b] are displayed by the lines. Figure 5.3 shows that the ideal hydrodynamic model calculations reproduce the mass ordering of v_2 in the relatively low p_T region (the heavier the mass, the smaller the v_2) but overshoot the values of v_2 for all centrality bins. There seems to be a p_T dependence in the disagreement, and for more central collisions, the overshoot does not take place until a higher p_T. In other words, the system agrees better with the ideal hydrodynamic model for more central collisions. Although we do not expect a large nonflow contribution at the low transverse momentum region, the centrality selections between the model calculations based on the impact parameter and the data based on the multiplicity are different, which may also affect the model and data agreement. Note that we observe possible negative values of $v_2(p_T)$ for the heavier hadrons at the lowest observed p_T in the most central Au+Au collisions. At higher p_T, the hydrodynamic type mass ordering evolves into a hadron type ordering (baryons versus mesons). There the results show two groups depending on the number of quarks in the hadron; the baryons are higher than the mesons. For all p_T, v_2 evolves toward larger values in going from central collisions to more peripheral collisions. The ideal hydrodynamic model also predicts this centrality dependence, though it fails to describe the behavior at higher p_T.

Figure 5.4 shows the v_2 for K^0_S, Λ and Ξ as a function of p_T in different centrality selections for Cu+Cu collisions at $\sqrt{s_{NN}} = 200$ GeV along with results of hydrodynamical calculations [Huo08a]. The ideal hydrodynamical model does not describe the centrality dependence of our data. For $0-20\%$, the model under-predicts the data and for $20-60\%$, it over-predicts the v_2.

As a conclusion, we find that the ideal hydrodynamical calculations fails to reproduce the data in both Au+Au and Cu+Cu collisions at $\sqrt{s_{NN}} = 200$ GeV. Since hydrodynamics is a theory based on thermalization, it may provide a tool to test whether the system created at RHIC reaches thermalization. To date, there are serval effects not included in the model, such as geometrical fluctuations in the initial conditions (particularly important in central collisions), finite viscosity effects. It remains to be seen if these effects can account for the difference between the models and data.

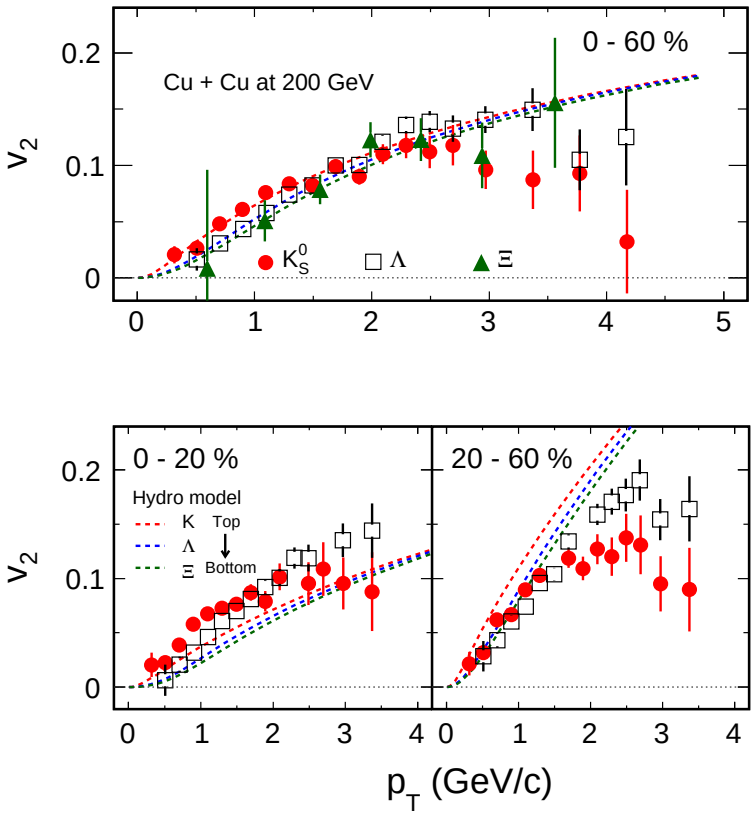

Figure 5.4: v_2 as a function of p_T for K^0_S, Λ and Ξ in $0-60\%$ (top), $0-20\%$ and $20-60\%$ (bottom) Cu+Cu collisions at $\sqrt{s_{NN}} = 200$ GeV. Dashed lines represent ideal hydrodynamical calculation [Huo08a]. From top to bottom, the lines represent the results for K, Λ and Ξ.

5.3 System and Centrality Dependence of v_2

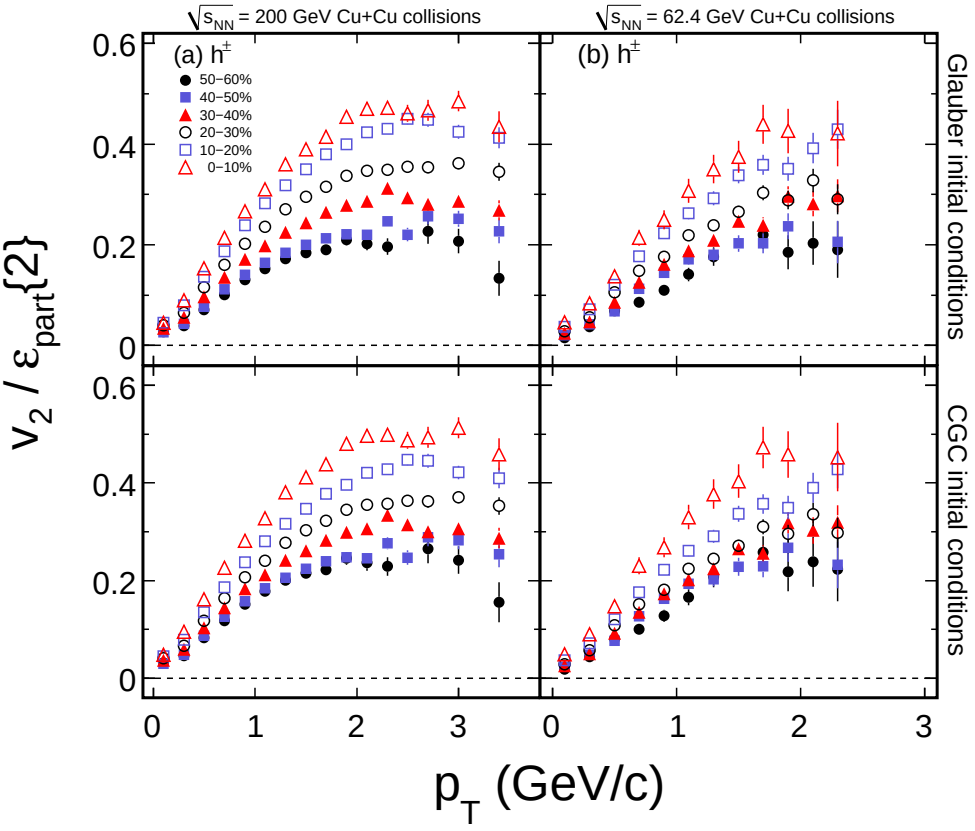

Figure 5.5: Charged hadron v_2 scaled by participant eccentricity as a function of p_T in $\sqrt{s_{NN}}$ = 200 and 62.4 GeV Cu+Cu collisions.

The centrality and system-size dependence of v_2 is related to the physics of the system created in high energy nuclear collisions. In the ideal hydrodynamic limit the centrality dependence of elliptic flow is mostly defined by the elliptic anisotropy of the overlapping region of the colliding nuclei, and in the low-density limit by the product of the elliptic anisotropy and the multiplicity. Thus, the centrality and system-size dependence of elliptic flow should be a good indicator of the degree of equilibration reached in the reaction [Vol00a].

For a study of the centrality dependence of $v_2(p_T)$ in Cu+Cu collisions together with Au+Au collisions, we divide $v_2(p_T)$ by the initial spatial anisotropy, eccentric-

	Centrality	$\varepsilon_{\rm part}\{2\}$(CGC)	$\varepsilon_{\rm part}\{2\}$(Glauber)	$N_{\rm part}$
Au+Au	$0-80\%$	0.338 ± 0.002	0.302 ± 0.004	126 ± 8
	$0-10\%$	0.148 ± 0.001	0.123 ± 0.003	326 ± 6
	$10-40\%$	0.353 ± 0.001	0.296 ± 0.009	173 ± 10
	$40-80\%$	0.554 ± 0.002	0.533 ± 0.018	42 ± 7
Cu+Cu	$0-60\%$	0.336 ± 0.009	0.350 ± 0.008	51 ± 2
	$0-20\%$	0.230 ± 0.010	0.235 ± 0.008	87 ± 2
	$20-60\%$	0.434 ± 0.003	0.468 ± 0.016	34 ± 1
	$0-10\%$	0.187 ± 0.002	0.197 ± 0.002	99 ± 2
	$10-20\%$	0.281 ± 0.002	0.279 ± 0.008	75 ± 2
	$20-30\%$	0.360 ± 0.003	0.369 ± 0.009	54 ± 1
	$30-40\%$	0.428 ± 0.002	0.458 ± 0.017	38 ± 1
	$40-50\%$	0.490 ± 0.002	0.550 ± 0.021	26 ± 1
	$50-60\%$	0.555 ± 0.004	0.643 ± 0.031	17 ± 1

Table 5.1: Participant eccentricity $\varepsilon_{\rm part}\{2\}$ and number of participants $N_{\rm part}$ from the Monte Carlo Glauber model [Mil03b, Mil07a] and Color Glass Condensate (CGC) model [Dre05a, Dre07a, Dre07b, Dre09a] calculations in Au+Au and Cu+Cu collisions at $\sqrt{s_{NN}} = 200$ GeV. The quoted errors are total statistical and systematic uncertainties added in quadrature.

ity, to remove this geometric effect. Figure 5.5 shows the centrality dependence of $v_2(p_T)/\varepsilon_{\rm part}\{2\}$ for $h^{\pm}$ in 200 and 62.4 GeV Cu+Cu collisions. For a given centrality bin, $v_2(p_T)/\varepsilon_{\rm part}\{2\}$ initially increases with p_T and then flattens or falls off at higher p_T. After the geometric effect is removed, the ordering of the distributions as a function of centrality, observed in Fig. 4.5, is reversed: the more central the collision, the higher the $v_2(p_T)/\varepsilon_{\rm part}\{2\}$. This suggests that the strength of collective motion is larger in more central collisions.

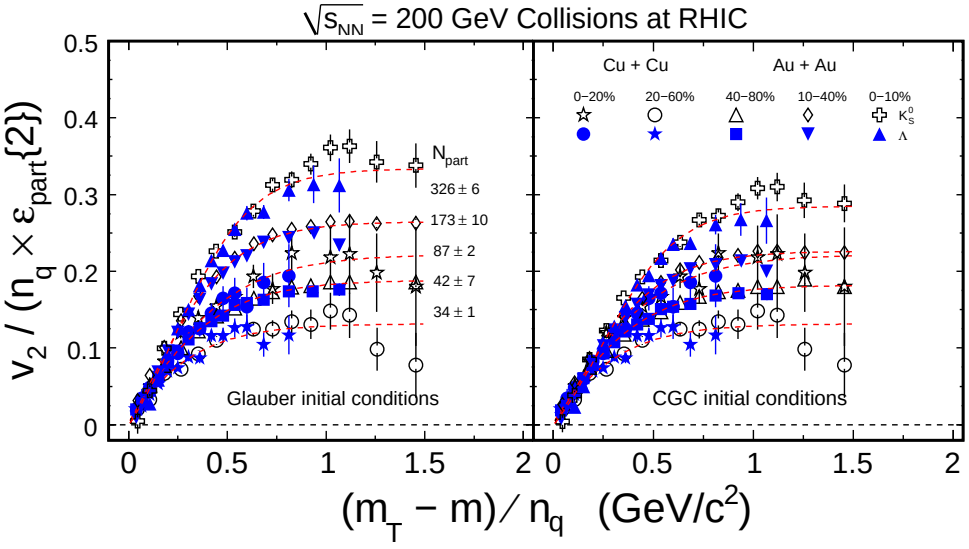

Figure 5.6: Centrality dependence of v_2 scaled by number of quarks and participant eccentricity ($v_2/(n_q \times \varepsilon_{\rm part}\{2\})$) for K^0_S (left) and Λ (right) as a function of $(m_T - m)/n_q$ in $0-10\%$, $10-40\%$ and $40-80\%$ Au+Au collisions (open symbols) [Abe08a] and $0-20\%$ and $20-60\%$ Cu+Cu collisions (solid symbols) at $\sqrt{s_{NN}} = 200$ GeV. Curves are the results of n_q-scaling fits from Eq. (4.4) normalized by $\varepsilon_{\rm part}\{2\}$ to combined K^0_S and Λ for five centrality bins. At a given p_T, from top to bottom, the curves show a decreasing trend as a function of $N_{\rm part}$.

To further study the centrality dependence of strange hadron v_2, we normalized the n_q-scaled values by $\varepsilon_{\rm part}\{2\}$ and plotted them as a function of $(m_T - m)/n_q$. The centrality dependence of K^0_S and Λ results are shown in Fig. 5.6. The full symbols show from top to bottom the results from $0-20\%$ and $20-60\%$ centrality Cu+Cu collisions. For comparison, the results from 200 GeV Au+Au collisions [Abe08a] are shown by open

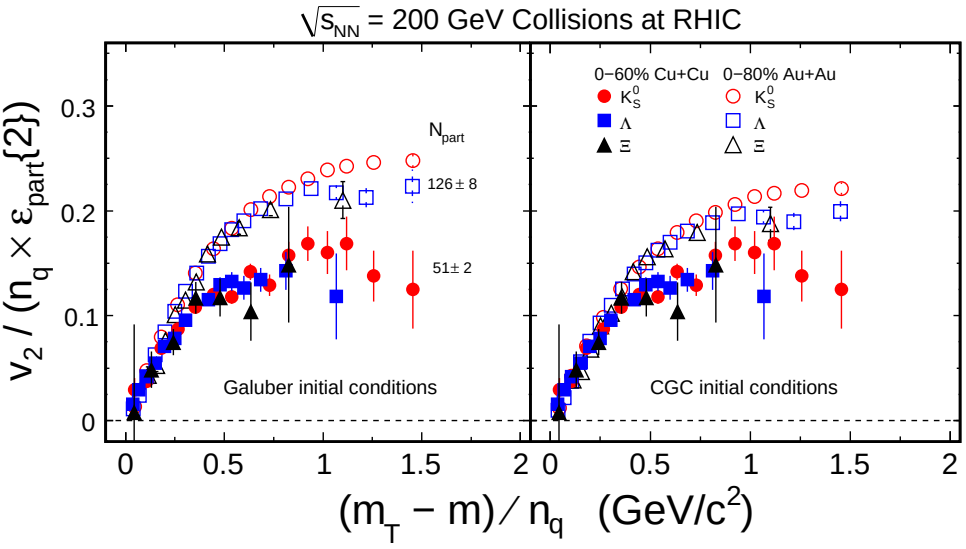

Figure 5.7: Number of quarks and participant eccentricity scaled v_2 ($v_2/(n_q \times \varepsilon_{\rm part}\{2\})$) of identified particles as a function of $(m_T - m)/n_q$ in $0-80\%$ Au+Au collisions (open symbols) [Abe08a] and $0-60\%$ Cu+Cu collisions (closed symbols) at $\sqrt{s_{NN}} = 200$ GeV. Circles, squares and triangles represent the data for K^0_S, Λ and Ξ, respectively.

symbols in Fig. 5.6. The results in Au+Au collisions are slightly different ($\sim 10\%$ larger) from the previous published results [Abe08a], which were calculated directly from the wide centrality bins. From top to bottom, the results are from $0-10\%$, $10-40\%$ and $40-80\%$ centrality bins. Curves represent n_q-scaling fits from Eq. (4.4) normalized by $\varepsilon_{\rm part}\{2\}$ to the combined data of K^0_S and Λ for five centrality bins. For a given centrality, K^0_S and Λ results follow a universal curve, which means partonic collective flow is explicitly seen in the measured scaling with n_q and $\varepsilon_{\rm part}\{2\}$. For a given collision system, the stronger partonic collective flow is apparent as higher scaled v_2 value in more central collisions. To study the system-size dependence of the scaling properties, the results from $0-60\%$ centrality Cu+Cu and $0-80\%$ Au+Au collisions are shown in Fig. 5.7. The stronger collective motion in Au+Au compared to Cu+Cu collisions becomes obvious although the constituent quark degrees of freedom have been taken into account in both systems.

In the ideal hydrodynamic limit where dynamic thermalization is reached, the mean

free path is much less than the geometric size of the system. The geometric size of the system and the centrality dependence of flow is totally governed by the initial geometry (eccentricity) [Vol00a]. As there is no universal scaling with the eccentricity among either different collision centralities or different collision system sizes, this indicates that the ideal hydrodynamic limit is not reached in Cu+Cu collisions, presumably because the assumption of thermalization is not attained. In addition, $v_2/(n_q \times \varepsilon_{\rm part}\{2\})$ shows an increasing trend as a function of $N_{\rm part}$ (See Fig. 5.6). Table 5.1 lists the values of eccentricity and $N_{\rm part}$ for the used centrality bins in Au+Au and Cu+Cu collisions. This suggests that the measured v_2 is not only dependent on the initial geometry, but also on $N_{\rm part}$.

5.4 The Ideal Hydrodynamic Limit

It was shown, in [Adl02b, Ada05a], that the measured v_2 scaled by the spatial eccentricity reaches the expected ideal hydrodynamic values but this only happens for the most central collisions. The discrepancy for more peripheral collisions as well as at lower energies and away from mid-rapidity indicates that for these collisions the elliptic flow has significant non-ideal hydrodynamic contributions. Much of this discrepancy could be explained by incorporating viscous contributions of the hadronic phase [Tea01a, Tea00a, Hir06a, Hir05a]. The resulting picture was a perfect liquid for the hot and dense part of the system surrounded by a dissipative hadronic corona. Kovtun, Son and Starinets [Kov04a], showed that conformal field theories with gravity duals have a ratio of viscosity η to entropy density s of $1/4\pi$ (in natural units). They conjectured that this value is a bound for any relativistic thermal field theory (However, Buchel, Mayers and Sinha argued that such bound can be violated in superconformal gauge theories with non-equal central charges $c \neq a$ [Buc08a]). In addition, Teaney [Tea03a] had pointed out that already very small viscosities, of the magnitude of the bound, would lead to a significant reduction in the predicted elliptic flow. Therefore models which take into account these effects find very strong constraints on the the magnitude of η/s when trying to describe the large observed elliptic flow. However, more recently, it was

realized that uncertainties in the initial conditions, e.g. the spatial eccentricity [Hir05a], and uncertainties in the EoS [Huo05a] are substantial as well, which opens up the range of possible (larger) values of η/s.

Currently there are two promising approaches to quantify how big the possible discrepancy between data and ideal hydrodynamics. The first approach is to match the data using hydrodynamic models which incorporate viscous corrections [Son08a, Rom08a]. One of the drawbacks of this approach is that η/s is not the only unknown, also the initial conditions and EoS need to be varied. The second approach is a fit of v_2/ε versus particle density based on a parametrization in terms of the Knudsen number [Bha05a, Oll07a]. The Knudsen number K is the mean free path of the constituents divided by the system size. The fit yields K and extrapolating the fit to $K = 0$ yields the ideal hydrodynamic limit of v_2/ε. The latter defines the effective velocity of sound and thus the effective EoS.

In this section, we will present STAR measurements of v_2/ε as a function of particle density in the transverse plane. This observable is considered sensitive to deviations from ideal hydrodynamics. We will compare these observables with transport model calculations and test if they can be understood with a common Knudsen number. Additionally we will test how the conclusions depend on varying the initial conditions.

To quantify this further we fit v_2/ε versus particle density based on the parameterization in terms of the Knudsen number [Bha05a, Oll07a] given by:

$$\begin{aligned} \frac{v_2}{\varepsilon} &= [\frac{v_2}{\varepsilon}]_{\rm hydro} \frac{1}{1 + K/K_0} \\ &= [\frac{v_2}{\varepsilon}]_{\rm hydro} \frac{1}{1 + (\sigma c_s \frac{1}{S}\frac{dN}{dy})^{-1}\frac{1}{K_0}} \end{aligned} \tag{5.3}$$

where K is the Knudsen number, and K_0 is a constant which can be determined through transport calculations. Following [Oll07a] we take $K_0 = 0.7 \pm 0.03$. There is a factor of 40 difference S given here and that in [Oll07a] which stems from the different definition and units of S (in STAR, $S = \pi\sqrt{\bar{x^2}\ \bar{y^2}}$, in fm^2 and in [Oll07a], $S = 4\pi\sqrt{\bar{x^2}\ \bar{y^2}}$, in mb). $[\frac{v_2}{\varepsilon}]/[\frac{v_2}{\varepsilon}]_{\rm hydro}$ and σc_s are free parameters that extracted from fitting the data. The formula has the two desired properties at two extremes: $1 - [\frac{v_2}{\varepsilon}]/[\frac{v_2}{\varepsilon}]_{\rm hydro} \propto$ K when K is small (ideal hydro limit), and $[\frac{v_2}{\varepsilon}]/[\frac{v_2}{\varepsilon}]_{\rm hydro} \propto 1/$K when K is large (low density limit). In

this approach the hydrodynamic limit of v_2/ε can be only asymptotically approached.

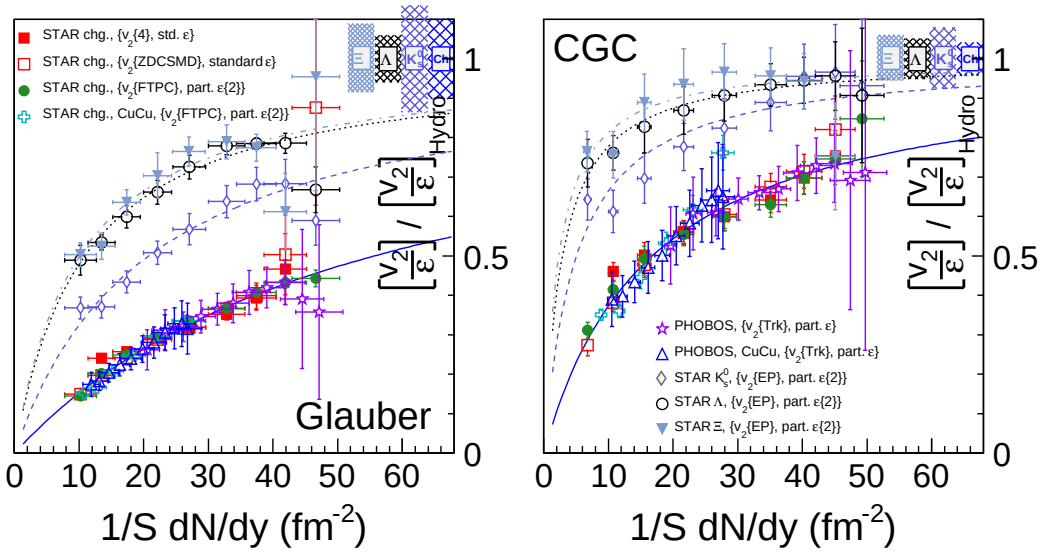

Figure 5.8: v_2/ε scaled by the corresponding hydrodynamic limits obtained from the simultaneous fitting, for Glauber (left) and CGC (right) initial conditions. The hydrodynamic limit is by definition centered at unity, with error represented by the cross-shaded bars.

In Fig. 5.8, $[\frac{v_2}{\varepsilon}]/[\frac{v_2}{\varepsilon}]_{\rm hydro}$ is plotted as a function of $1/S\ dN/dy$ for various particle species. The v_2 measurements that are sensitive to the participant plane anisotropy are scaled by the participant two particle cumulant eccentricity, and for the v_2 measurements that are sensitive to the reaction plane, by the standard eccentricity [Bha06a, Vol08a]. The participant plane measurements are i) v_2 measured with event plane constructed from Forward Time Projection Chamber (FTPC) ($v_2\{\rm FTPC\}$), ii) STAR's event plane v_2 ($v_2\{\rm EP\}$), iii) PHOBOS' track-based v_2 measurement ($v_2\{\rm Trk\}$) [Bac05b, Bac07a]; and the reaction plane measurements are STAR's four particle cumulant v_2 ($v_2\{4\}$) and v_2 measured by event plane constructed from spectator neutrons ($v_2\{\rm ZDC-SMD\}$). Data points are for collisions at $\sqrt{s_{NN}} = 200$ GeV, and by default they are for Au+Au collisions unless otherwise specified by the legends. The left panel is for the case with Glauber as initial condition, and the right panel, CGC. For the Glauber case, S and ε are calculated from a Monte Carlo Glauber with cross section of 42 mb. For the CGC case, they are based on Monte Carlo fKLN calculations [Oll07a]. dN/dy is taken from STAR's publication [Abe09a], and dN/dy used for PHOBOS data points is obtained

by projecting STAR's measurements with PHOBOS total cross sections. For charged particles, the fit is applied simultaneously to corresponding data sets (lowest group in the plot) with the additional constraint that σc_s is the same for individual data sets. The curves are obtained from the fitting and they represent the relative fraction to the fitted hydro limit, $\left[\frac{v_2}{\varepsilon}\right] / \left[\frac{v_2}{\varepsilon}\right]_{\rm hydro}$. The more saturation in the shape, the closer to the fitted hydro limit. A stronger saturation in shape is observed in CGC case if compared to that in Glauber case. That is understood as, going from peripheral to central collisions, CGC predicts a smaller decrease of eccentricity than Glauber does. The plot shows a splitting of $[\frac{v_2}{\varepsilon}]/[\frac{v_2}{\varepsilon}]_{\rm hydro}$ due to particle's mass. The heavier the particle, the more saturation in the shape is observed. Such mass hierarchy is not a built-in feature in the model [Bha05a, Oll07a], and it is desirable to see if other models can explain it.

The extracted σc_s is not meaningful for massive particles because in the transport model [Bha05a, Oll07a] that motivated this fit, $K_0 = 0.7$ is obtained with massless particles and is not applicable for massive particles. In the following, we quote numbers only for charged particles (mostly pions). To check if the procedure is robust, the fit is repeated with additional two formula.

$$\frac{v_2}{\varepsilon} = [\frac{v_2}{\varepsilon}]_{\rm hydro} \frac{2}{\pi} {\rm atan}(\frac{1}{K/K_0}) \tag{5.4}$$

$$\frac{v_2}{\varepsilon} = [\frac{v_2}{\varepsilon}]_{\rm hydro} \frac{1}{2}(1 - e^{-\frac{1}{K/K_0}} + e^{-K/K_0}) \tag{5.5}$$

In central collisions, for both Glauber case and CGC case, $[\frac{v_2}{\varepsilon}]/[\frac{v_2}{\varepsilon}]_{\rm hydro}$ obtained with different fit formula are consistent with each other within ∼20% in absolute value, and the extracted σc_s, ∼30% in relative value. Systematical errors from v_2, ε, S and dN/dy have been decomposed into correlated and uncorrelated parts, for the latter, a special procedure [Pdg08a] is carried out so that it can be included, together with uncorrelated error, in the final error extracted from the fitting. In most v_2 values used in this analysis, the correlations not related to reaction plane (nonflow) has been effectively suppressed, either by η gap between particles used to reconstruct the event plane and particles used to study the flow, or by measuring multi-particle cumulants v_2. However, it is still possible that there is additional systematical error that comes from remaining nonflow in v_2 measurements that are based on two particle correlations. Its magnitude is estimated

by comparing σc_s obtained from fitting STAR's $v_2\{\text{FTPC}\}$ and PHOBOS' $v_2\{\text{Trk}\}$, to that obtained with fitting STAR's $v_2\{\text{EP}\}$ for charged particles with corrections [Pos09a] made with following assumptions: 1.) v_2 fluctuations are originated from initial Glauber or CGC eccentricity fluctuations, 2.) azimuthal correlations in p+p collisions are all due to nonflow, 3.) nonflow in Au+Au collisions is equivalent to that in p+p collisions scaled by $2/N_{\text{part}}$, where N_{part} is the number of participant nucleons. From the fitted curve, for central Au+Au collisions, $[\frac{v_2}{\varepsilon}]/[\frac{v_2}{\varepsilon}]_{\text{hydro}}$ is $0.46 \pm 0.05(\text{fit})^{+0.23}_{-0}(\text{formula}) + 0.05(\text{nonflow})$ and $0.75 \pm 0.03(\text{fit})^{+0.14}_{-0.06}(\text{formula}) - 0.07(\text{nonflow})$, for Glauber case and CGC case, respectively. The fitted σc_s is $1.03 \pm 0.38(\text{fit})^{+0.31}_{-0}(\text{formula}) + 0.20(\text{nonflow})$ mb and $3.41 \pm 0.69(\text{fit})^{+0}_{-0.96}(\text{formula}) - 1.12(\text{nonflow})$ mb, for Glauber case and CGC case, respectively. For both initial conditions, there still might be considerable room for flow to increase before the system saturates at hydrodynamic limits.

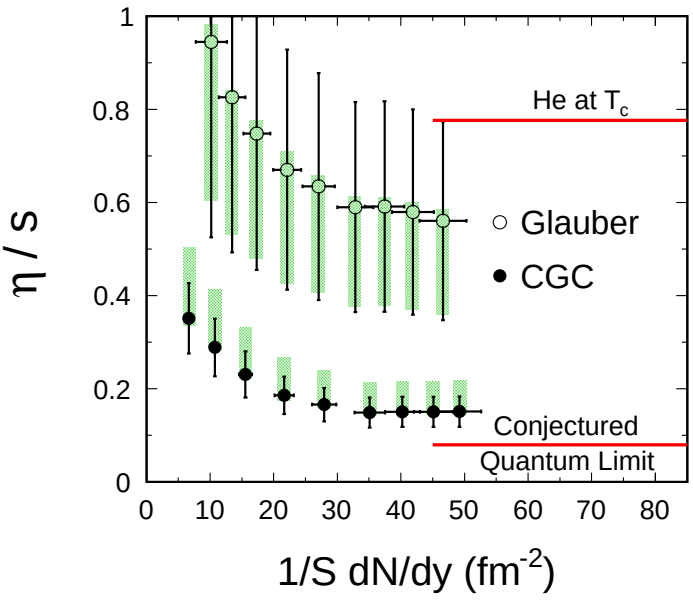

Figure 5.9: η/s as a function of $1/S\ dN/dy$ for collisions at $\sqrt{s_{NN}}$ =200 GeV. The conjectured quantum limit, as well as η/s for He at T_c is also plotted for comparison.

Following [Tea03a], the viscosity for a classical gas of massless particles with isotropic differential cross sections is $\eta = 1.264T/\sigma$ [Kox76a]. It is arguable to apply the formula to strongly interacting dense matter, however, in practice the viscosity recovered

from this procedure agrees well with that obtained from viscous hydrodynamic calculations. [Sne09a]. Taking the entropy density for a classical ultrarelativistic gas as $s = 4n$, with n the particle density, then η/s can be calculated as $\eta/s = 0.316\frac{T}{\sigma n} = 0.316\frac{T}{\sigma c_s}\frac{S\bar{R}}{dN/dy}$, where σc_s is from fitting v_2/ε mentioned above, and $\bar{R} \equiv \frac{1}{\sqrt{1/\langle x^2\rangle + 1/\langle y^2\rangle}}$ is obtained from Glauber(CGC) calculations. The temperature T is obtained from fitting STAR's π m_T slope [Abe09a]. In Fig. 5.9, η/s is plotted as a function of $1/S\ dN/dy$ for Glauber and CGC initial conditions. The symmetrical and asymmetrical error from σc_s has been propagated into the errors of η/s accordingly. The difference of T obtained from fitting STAR [Abe09a] and PHENIX's [Adl04a] π m_T spectra has been included in the systematical error. η/s for Glauber initial condition is $7.05 \pm 2.68(\text{sym. error})^{+0.28}_{-2.55}(\text{asym. error})$ times of the conjectured quantum limit, and for CGC, $1.9 \pm 0.41(\text{sym. error})^{+0.83}_{-0.08}(\text{asym. error})$ times. Both lower than η/s for He at T_c. The extracted η/s is different than that in [Oll07a] because the $1/S\ dN/dy$ used in [Oll07a] is solely from model calculations while we used dN/dy from measurements. η/s for CGC initial condition is smaller than that for Glauber initial condition, because with CGC initial condition, a stronger saturation is seen in the shape of v_2/ε vs. $1/S\ dN/dy$, which gives a larger σc_s. This does not necessarily contradict to the conclusion arrived from viscous hydro calculations [Son08a, Rom08a], in which the Equation of State is chosen to be the same for the two initial conditions. For $1/S\ dN/dy > 15$, η/s is consistent with a constant, as one expected from transport model [Oll07a]. Note that the extracted η/s is an effective quantity which includes viscous effects over different phases, including a hadronic phase for which the expected viscous effect is larger than that of the QGP phase.

In summary, we have presented v_2 scaled by initial eccentricities as a function of $1/S\ dN/dy$, we see more saturation for heavy particles. Our measurements for charged particles are compared to transport model calculations. It is found that the the system has reached $0.46^{+0.24}_{-0.07}$ and $0.75^{+0.14}_{-0.10}$ of the value at which it is supposed to saturate (ideal hydrodynamic limit), indicating that there still might be considerable amount of room for flow to increase. We report the σc_s for Glauber initial condition as $1.78 \pm 0.66(\text{fit})^{+0.53}_{-0}(\text{formula}) + 0.35(\text{nonflow})$ mb, and $5.90 \pm 1.2(\text{fit})^{+0}_{-1.67}(\text{formula}) - 1.94(\text{nonflow})$ mb

for CGC initial condition. We calculated η/s as a function of $1/S\ dN/dy$ for collisions at 200 GeV. For $1/S\ dN/dy$ that corresponds to central Au+Au collisions at 200 GeV, it is $7.05 \pm 2.68(\text{sym. error})^{+0.28}_{-2.55}(\text{asym. error})$ and $1.9 \pm 0.41(\text{sym. error})^{+0.83}_{-0.08}(\text{asym. error})$ times the conjectured quantum limit, for Glauber and CGC initial condition respectively.

CHAPTER 6

Summary and Outlook

In this thesis, we analyze the data collected with the STAR detector from $\sqrt{s_{NN}}$ = 62.4 and 200 GeV Cu+Cu collisions during the fifth RHIC run in 2005 and $\sqrt{s_{NN}}$ = 9.2 and 200 GeV Au+Au collisions during the seventh run in 2007. We present results on elliptic flow v_2 of charged hadrons and identified particles in the midrapidity region $|\eta| < 1.0$. Significant reduction in systematic uncertainty of the measurement due to non-flow effects has been achieved by correlating particles at midrapidity, $|\eta| < 1.0$, with those at forward rapidity, $2.5 < |\eta| < 4.0$. As a part of the systematic study, we also present azimuthal correlations in p+p collisions at $\sqrt{s_{NN}}$ = 200 GeV, which are used for estimating the error from non-flow effects.

We study the system size dependence of elliptic flow by comparing the results from Cu+Cu collisions with previously results [Abe08a] from Au+Au collisions at $\sqrt{s_{NN}}$ = 200 GeV. We observe that $v_2(p_T)$ of strange hadrons has similar scaling properties as was first observed in Au+Au collisions, i.e.: (i) at low transverse momenta, $p_T < 2$ GeV/c, v_2 scales with transverse kinetic energy, $m_T - m$, and (ii) at intermediate p_T, $2 < p_T < 5$ GeV/c, it scales with the number of constituent quarks (NQ).

We systematically discuss the NQ scaling at RHIC and find it holds in the intermediate p_T region, $2 < p_T < 5$ GeV/c, for all systems and beam energies studied here. In particularly, the multi-strange hadrons Ω and ϕ show nearly the same elliptic flow as the protons and pions. This provides fairly convincing evidence that the majority of the elliptic flow develops during the partonic process. Thus, it indicates the partonic collectivity has been built up at RHIC.

A comparison between data and ideal hydrodynamic calculations has been made

in Au+Au and Cu+Cu collisions at $\sqrt{s_{NN}}$ = 200 GeV collisions. We find that ideal hydrodynamic calculations fail to reproduce the centrality dependence of $v_2(p_T)$.

It is found that the $1/S\ dN/dy$ dependence of v_2/ε can be described well by transport models with finite Knudsen numbers, even for central collisions. The result indicates that the system has reached $0.46^{+0.24}_{-0.07}$ and $0.75^{+0.14}_{-0.10}$ of ideal hydrodynamic limits, using Glauber and Color Glass Condensate (CGC) initial condition, respectively. Constrains on the product of the cross section and the speed of sound are provided, η/s is estimated.

Full Time-of-Flight upgrade and construction of Heavy Flavor Tracker are two important upgrades of STAR detectors. They will significantly extend the STAR detection capabilities and physics program. The primary motivation of HFT is to extend STAR's capability to measure heavy flavor production by the measurement of displaced vertices and to do the direct topological identification of open charm hadrons. A precise measurement of the spectra of D meson will shed light on several open questions in heavy ion collisions. From the spectra and production rate of D meson, we will be able to extrapolate to the total yield for charm quark production at RHIC. Due to high open charm production rate at RHIC, the coalescence process becomes relevant for charm production. Total charm cross section will serve as a baseline for J/Ψ measurements. This will help us to answer the question of whether J/Ψ mesons are suppressed or enhanced at RHIC. Due to the large mass, the heavy quark can be used to probe the properties of the medium created in heavy ion collisions. Due to the dead cone effect, heavy flavor should radiate less gluons, hence lose less energy in the dense medium. Currently, indirect measurements of non-photonic electrons as a measurement of the abundance of charm and bottom hadrons indicate unexpected high energy loss for heavy quarks and show inconsistency with pQCD models. Measurements of charmed meson R_{AA} will be very important with HFT. Another important measurements is a measurement of the elliptic flow of D mesons down to very low p_T values. Flow of charm quarks can be taken as a probe of frequent re-scatterings of light quarks. Measurements of D meson v_2 will gain information on the thermalization among u, d, s quarks.

As the NQ scaling of v_2 indicates the hot and dense matter created in the heavy ion collisions is dominated the partonic degrees of freedom, thus the beam energy dependence

of the NQ scaling of v_2 should be a powerful tool to search for the phase boundary in the future Beam Energy Scan program at RHIC. When scan from high to low beam energy, the broken of the scaling for identified hadrons, especially for the multi-strange hadron such as ϕ will signal a system where hadronic degrees of freedom dominant. In high-energy nuclear collisions at RHIC ($\sqrt{s_{NN}} = 60 \sim 200$ GeV), the quark coalescence has been identified as the process for hadronization. As a result, one observes a scaling in elliptic flow parameter v_2 (within $2 < p_T < 5$ GeV/c region). On the other hand, in a given collision when the center of mass energy is not sufficiently high to create partonic matter, one would not expect the scaling in the final observed v_2. Hence, the scaling provides us a sensitive tool in order to search for the possible phase boundary in the hot/dense matter dominated by either partonic or hadronic degrees of freedom.

References

[Abe03a] J. Abele et al. *Nucl. Instru. Methd A*, **499** 692, 2003.

[Abe07a] B. I. Abelev et al. (STAR Collaboration), *Phys. Rev. C* **75**, 054906 (2007).

[Abe08a] B. I. Abelev et al. (STAR Collaboration), *Phys. Rev. C* **77**, 054901 (2008).

[Abe09a] B. I. Abelev et al. (STAR collaboration), *Phys. Rev. C* **79**, 034909 (2009).

[Abe10a] B. I. Abelev et al. (STAR collaboration), *Phys. Rev. C* **81**, 024911 (2010).

[Ack01a] K. H. Ackermann et al. *Phys. Rev. Lett.*, **86** 402, 2001.

[Ack03a] K. Ackermann et al. *Nucl. Instru. Methd A*, **499** 624, 2003.

[Ack03b] K. Ackermann et al. *Nucl. Instru. Methd A*, **499** 709, 2003.

[Ada03a] M. Adamczyk et al. *Nucl. Instru. Methd A*, **499** 437, 2003.

[Ada03b] J. Adams et al. *Phys. Rev. Lett*, **91** 072304, 2003.

[Ada04a] J. Adams et al. *Phys. Rev. Lett.*, **92** 182301, 2004.

[Ada04b] J. Adams et al. (STAR Collaboration), *Phys. Rev. Lett.* **93**, 252301 (2004).

[Ada04c] J. Adams et al. *Phys. Rev. Lett.*, **92** 052302, 2004.

[Ada05a] J. Adams et al. (STAR Collaboration), *Nucl. Phys. A*, **757**, 102, 2005.

[Ada05b] J. Adams et al. *Phys. Rev. Lett.*, **95** 122301, 2005.

[Ada05c] J. Adams et al. (STAR Collaboration), *Phys. Rev. C* **72**, 014904 (2005).

[Ada05d] J. Adams et al. *Phys. Lett. B*, **612** 181, 2005.

[Ada06a] A. Adare et al. *nucl-ex/0608033*

[Adc03a] K. Adcox et al. *Nucl. Instru. Methd A*, **499** 469, 2003.

[Adl02a] C. Adler et al. *Phys. Rev. Lett.*, **89** 202301, 2002.

[Adl02b] C. Adler et al. (STAR Collaboration), *Phys. Rev. C* **66**, 034904 (2002).

[Adl03a] C. Adler et al. *Phys. Rev. Lett.*, **90** 082302, 2003.

[Adl04a] S. S. Adler et al. (PHENIX collaboration), *Phys. Rev. C* **69**, 034909 (2004).

[Agg03a] M. M. Aggarwal et al. *Nucl. Instr. Method A*, **499** 751, 2003.

[All03a] C. E. Allgower et al. *Nucl. Instr. Method A*, **499** 740, 2003.

[Alt03a] C. Alt et al. (NA49 Collaboration), *Phys. Rev. C* **68**, 034903 (2003).

[Alv06a] B. Alver et al. (PHOBOS Collaboration), *nucl-ex/0610037*

[Alv08a] B. Alver et al. (PHOBOS Collaboration), *Phys. Rev. C* **77**, 014906 (2008).

[And99a] C. Anderlik et al. *Phys. Rev. C*, **59** 3309, 1999.

[And03a] M. Anderson et al. *Nucl. Instr. Method A*, **499** 659, 2003.

[Arn03a] L. Arnold et al. *Nucl. Instr. Method A*, **499** 652, 2003.

[Bac03a] B. B. Back et al. *Nucl. Instr. Methd A*, **499** 603, 2003.

[Bac05a] B. B. Back et al. *Nucl. Phys. A*, **757** 28, 2005.

[Bac05b] B. B. Back et al. (PHOBOS collaboration), *Phys. Rev. C* **72**, 051901(R) (2005).

[Bac07a] B. B. Back et al. (PHOBOS collaboration), *Phys. Rev. Lett.* **98**, 242302 (2007).

[Bai07a] Y. Bai, *Ph.D. thesis*, 2007

[Bar97a] J. Barrette et al. (E877 Collaboration), *Phys. Rev. C* **56**, 3254 (1997).

[Bar04a] O. Barannikova et al. *nucl-ex/0403014*.

[Bas99a] S. A. Bass, M. Gyulassy, H. Stöcker, W. Greiner. *J. Phys. G*, **25** R1, 1999.

[Bas99b] S. A. Bass et al., *Phys. Rev. C* **60**, 021902 (1999).

[Bas00a] S. A. Bass, A. Dumitru. *Phys. Rev. C*, **61** 064909, 2000.

[Bed03a] M. Beddo et al. *Nucl. Instr. Methd A*, **499** 725, 2003.

[Bei03a] F. S. Beiser et al. *Nucl. Instr. Methd A*, **499** 762, 2003.

[Bel03a] R. Bellwied, et al. *Nucl. Instr. Method A*, **499** 636, 2003.

[Ber03a] F. Bergsma, et al. *Nucl. Instr. Method A*, **499** 629, 2003.

[Bet02a] S. Bethke. *Nucl. Phys. Proc. Suppl.*, **121**:74-81, 2003.

[Bha03a] R. S. Bhalerao, N. Borghini, J.-Y. Ollitrault. *Nucl. Phys. A*, **727** 373, 2003.

[Bha05a] R. Bhalerao et al., *Phys. Lett. B* **627** 49 (2005).

[Bha06a] R. Bhalerao and J-Y. Ollitrault, *Phys. Lett. B* **614**, 260 (2006).

[Bia81a] S. F. Biagi et al., *Nucl. Phys. B* **186**, 1 (1981).

[Ble99a] M. Bleicher et al. *J. Phys. G*, **25** 1859, 1999.

[Ble02a] M. Bleicher, H. Stöcker. *Phys. Lett. B*, **526** 309, 2002.

[Bon03a] B. Bonner et al. *Nucl. Instru. Method A*, **508** 181, 2003.

[Bor01a] N. Borghini, P. M. Dinh, J.-Y. Ollitrault. *Phys. Rev. C*, **63** 054906, 2001.

[Bra95a] P. Braun-Munzinger, J. Stachel, J. Wessels and N. Xu. *Phys. Lett. B*, **344** 43, 1995.

[Bra99a] P. Braun-Munzinger, I. Heppe, J. Stachel. *Phys. Lett. B*, **465** 15, 1995.

[Bra03a] P. Braun-Munzinger, K. Redlich, J. Stachel, in Quark Gluon Plasma 3, eds.

[Bra04a] E. L. Bratkovskaya et al. *Phys. Rev. C*, **69** 054907, 2004.

[Bre69a] M. Breidenbach et al. *Phys. Rev. Lett*, **23** 935, 1969.

[Buc08a] A. Buchel, R. Myers and A. Sinha, *arXiv:0812.2521.*

[Bur04a] G. Burau, J. Bleibel, C. Fuchs, A. Faessler, L. V. Bravina, E. E. Zabrodin. *Phys. Rev. C*, **71** 054905, 2005.

[Che03a] Y. Cheng et al., *Phys. Rev. C* **68**, 034910 (2003).

[Coo74a] F. Cooper and G. Frye. *Phys. Rev. D*, **10** 186, 1974.

[Dre05a] H. J Dresher et al., *Phys. Rev. C* **74**, 044905 (2006).

[Dre07a] H. J Dresher and Y. Nara, *Phys. Rev. C* **76**, 041903 (2007).

[Dre07b] H. J Dresher and Y. Nara, *Phys. Rev. C* **75**, 034905 (2007).

[Dre09a] H. J Dresher and Y. Nara, *Phys. Rev. C* **79**, 064904 (2009).

[Dks03a] G. Dissertori, I. Knowles, and M. Schmelling. *Quantum Chromodynamics - High Energy Experiments and Theory.* Oxford Universidy Press, 2003.

[Don04a] X. Dong et al., *Phys. Lett. B*, **597** 328 (2004).

[Dum99a] A. Dumitru et al. *Phys. Lett. B*, **460** 411, 1999.

[Fri03a] R. J. Fries et al., *Phys. Rev. Lett.* **90**, 202303 (2003).

[Fri04a] R. J. Fries. *J. Phys. G*, **31** S379, 2005.

[Gel64a] M. Gell-Mann. *Phys. Letters*, **8** 214, 1964.

[Gre03a] V. Greco, C. M. Ko, P. Levai. *Phys. Rev. Lett.*, **90** 202302, 2003.

[Hec98a] H. van Hecke, H. Sorge, and N. Xu, *Phys. Rev. Lett.* **81**, 5764 (1998).

[Hir05a] T. Hirano et al., *Phys. Lett. B* **636** (2006) 299.

[Hir05b] T. Hirano. *nucl-th/0510005*

[Hir06a] T. Hirano and M. Gyulassy, *Nucl. Phys. A* **769** (2006) 71.

[Hua88a] K. Huang. *Statistical Mechanics*, John Wiley and Sons, 1988.

[Hun98a] C. M. Hung, E. V. Shuryak. *Phys. Rev. C*, **57** 1891, 1998.

[Huo01a] P. Huovinen, P. F. Kolb, U. Heinz, P. V. Ruuskanen and S. A. Voloshin. *Phys. Lett. B*, **503** 58, 2001.

[Huo03a] P. Huovinen. *private communication*, 2003.

[Huo05a] P. Huovinen. *Nucl. Phys. A*, **761** 296, 2005.

[Huo06a] P. Huovinen and P.V. Ruuskanen, *Ann. Rev. Nucl. Part. Sci.* **56**, 163 (2006).

[Huo06b] P. Huovinen, *private communication*, 2006.

[Huo08a] P. Huovinen, *private communication*, 2008.

[Hwa03a] R. C. Hwa, X. N. Wang. *World Scientific, Singapore*, 2003.

[Hwa03b] R. C. Hwa and C. B. Yang, *Phys. Rev. C* **67**, 064902 (2003).

[Hwa04a] R. C. Hwa and C.B. Yang. *Phys. Rev. C*, **70** 024904, 2004.

[Iss06a] M. Issah and A. Taranenko for the PHENIX Collaboration, *nucl-ex/0604011*

[Kar02a] F. Karsch. *Nucl. Phys. A*, **698** 199, 2002.

[Kol03a] P. F. Kolb and U. Heinz. *nuch-th/0305084*.

[Kov04a] P. Kovtun, D. Son and A. Starinets, *Phys. Rev. Lett.* **94** (2005) 111601.

[Kox76a] A.J. Kox, S.R. de Groot and W. A. van Leeuwen, *Phys. A* **84** 155 (1976).

[Leb02a] A. Lebedev. *Nucl. Instru. Method A*, **478** 163, 2002.

[Lin02a] Z. W. Lin and C. M. Ko. *Phys. Rev. Lett.*, **89** 202302, 2002.

[Mag99a] V. K. Magas et al. *Heavy Ion Phys.*, **9** 193, 1999.

[Mar98a] S. Margetis. *STAR Note 0367*, 1998.

[Mat87a] T. Matsui, *Nucl. Phys. A* **461**, 27 (1987).

[Mat03a] H. S. Matis et al. *Nucl. Instru. Method A*, **499** 802, 2003.

[Mcl01a] L. McLerran, *hep-ph/0104285*

[Mil03a] M. Miller. *PhD thesis*, Yale University, 2003.

[Mil03b] M. Miller and R. Snellings, *nucl-ex/0312008*

[Mil07a] M. Miller et al., *Ann. Rev. Nucl. Part. Sci.* **57**, 205 (2007).

[Mil07b] M. Miller et al. *nucl-ex/0701025*

[Mol03a] D. Molnar and S. A. Voloshin, *Phys. Rev. Lett.* **91**, 092301 (2003).

[Mul72a] R. A. Muller, *Phys. Lett.* **38B**, 123 (1972).

[Non05a] C. Nonaka and S. A. Bass. *nucl-th/0510038*

[Old04a] M. Oldenburg et al. *J. Phys. G*, **31** S437, 2004.

[Old05a] M. Oldenburg et al. *nucl-ex/0510026*

[Oll92a] J.-Y. Ollitrault. *Phys. Rev. D*, **46** 229, 1992.

[Oll93a] J.-Y. Ollitrault. *Phys. Rev. D*, **48** 1132, 1993.

[Oll07a] H. Drescher et al., *Phys. Rev. C* **76** 024905 (2007).

[Pdg08a] Section 5.2.1, Particle Data Group, *Review of Particle Physics* (2008).

[Pos98a] A. M. Poskanzer and S. A. Voloshin, *Phys. Rev. C*, **58** 1671, 1998.

[Pos09a] A. M. Poskanzer, S. A. Voloshin and J-Y. Ollitrault, *Phys. Rev. C* **80**, 014904 (2009).

[Rei04a] W. Reisdorf and H. G. Ritter. *Ann. Rev. Nucl. Part. Sci.*, **47** 663, 1997.

[Rom08a] M. Luzum and P. Romatschke, *Phys. Rev. C* **78**, 034915 (2008).

[Rut11a] E. Rutherford. *Phil. Mag*, **21** 669, 1911

[Rut14a] E. Rutherford. *Phil. Mag*, **27** 488, 1914

[Sat00a] H. Satz. *Rept. Prog. Phys.*, **63** 1511, 2000.

[Sch93a] E. Schnedermann, J. Sollfrank, and U. Heinz. *Phys. Rev. C*, **48** 2462, (1993).

[Sel08a] I. Selyuzhenkov and S. Voloshin, *Phys. Rev. C*, **77**, 034904 (2008).

[Sho85a] A. Shor, *Phys. Rev. Lett.* **54**, 1122 (1985).

[Sne09a] R. Snellings et al., arXiv:0908.0430 (2009).

[Son08a] H. Song and U. Heinz, *Phys. Rev. C* **78**, 024902 (2008)

[Sor95a] H. Sorge. *Phys. Rev. C*, **52** 3291, 1995.

[Sor97a] H. Sorge. *Phys. Lett. B*, **402** 251, 1997.

[Sor97b] H. Sorge. *Phys. Rev. Lett.*, **78** 2309, 1997.

[Sto81a] H. Stöcker, M. Gyulassy, J. Boguta. *Phys. Lett. B*, **103** 269, 1981.

[Sto86a] H. Stöcker and W. Greiner. *Phys. Rept.*, **137** 277, 1986.

[Tea00a] D. Teaney, J. Lauret and E. Shuryak, *Phys. Rev. Lett.* **86** (2001) 4783.

[Tea01a] D. Teaney, J. Lauret and E. Shuryak, *nucl-th/0110037*

[Tea03a] D. Teaney, *Phys. Rev. C* **68** (2003) 034913.

[Tho897] J. J. Thomas. *Phil. Mag.*, **44** 293, 1897.

[Tho02a] J. H. Thomas. *Nucl. Instru. Method A*, **478** 166, 2002.

[Vol96a] S. Voloshin and Y. Zhang. *Z. Phys. C*, **70** 665, 1996.

[Vol98a] A. M. Poskanzer and S. A. Voloshin. *Phys. Rev. C*, **58** 1671, 1998.

[Vol00a] S. A. Voloshin and A. M. Poskanzer, *Phys. Lett. B* **474**, 27 (2000).

[Vol02a] D. Molnar, S. Voloshin. *Phys. Rev. Lett.*, **91** 092301, 2003.

[Vol06a] S. A. Voloshin, *nucl-th/0606022*

[Vol07a] S. A. Voloshin. *arXiv: nucl-ex/0701038*, 2007.

[Vol08a] S. A. Voloshin et al., *Phys. Lett. B* **659**, 537 (2008).

[Wan92a] X. N. Wang, M. Gyulassy. *Phys. Rev. Lett.*, **68** 1480, 1992.

[Wan97a] X. N. Wang, *Phys. Rep.* **280**, 287 (1997).

[Wan98a] X. N. Wang. *Phys. Rev. C*, **58** 2321, 1998.

[Wan05a] X. N. Wang. *Nucl. Phys. A*, **750** 98, 2005.

[Wil74] K. G. Wilson. *Phys. Rev. D*, **10** 2455, 1974.

[Wie06a] H. Wieman et al. *Technical Report*, 2006.

[Xu02a] N. Xu, M. Kaneta. *Nucl. Phys. A*, **698** 306c, 2002.

[Xu04a] N. Xu. *Prog. Part. Nucl. Phys.*, **53** 165, 2004.

[Zwe64a] G. Zweig. *CERN preprints Th.*, 401 and 412, 1964.

Presentations and publication List

Presentations

1. A Monte Carlo Study on the Expansion of Hadronic Gas in Relativistic Heavy Ion Collisions (oral)

   The Seventh Meeting of the High energy Physics Divisions of the Chinese Physical Society, Guilin, China, 2006.

2. Partonic collectivity at RHIC (oral)

   Third Joint Meeting of the Nuclear Physics Divisions of the American Physical Society and The Physical Society of Japan, Hawaii, USA, 2009.

3. Can we measure the viscosity from the system size dependence of v_2 (oral)

   Joint CATHIE/TECHQM Workshop, Brookhaven National Laboratory, USA, 2009.

4. Flow results from STAR at RHIC

   Heavy Ion Tea seminar, Lawrence Berkeley National Laboratory, USA, 2010.

Proceedings

1. K^0_S and Λ elliptic flow from 200 GeV Cu+Cu collisions, Shusu Shi for the STAR collaboration,

   20th International Conference on Ultra-Relativistic Nucleus Nucleus Collisions (Quark Matter 2008).

2. Strange hadron elliptic flow from 200 GeV Cu+Cu collisions, Shusu Shi for the STAR collaboration,

   Proc. 24th winter workshop on nuclear dynamics, 2008.

3. Event anisotropy v_2 at STAR, Shusu Shi for the STAR collaboration,

   21th International Conference on Ultra-Relativistic Nucleus Nucleus Collisions (Quark Matter 2009).

Publication list

1. A Monte-Carlo study on the multiplicity dependence of event- by- event transverse momentum fluctuation in relativistic heavy ion collision,

   Shusu Shi, and Jiaxin Du, *Huazhong Normal University Journal of Postgraduates* **13**, 144-146 (2006).

2. A Monte Carlo study on the expansion of hadronic gas in relativistic heavy-ion collisions,

   Shusu Shi, and Lianshou Liu, *High Energy Physics and Nuclear Physics* **31**, 56-58 (2007).

3. The inversion-asymmetry of particle emission source in relativistic heavy-ion collisions,

   Shusu Shi, Jiaxin Du and Lianshou Liu, *Eur. Phys. J. A* **33**, 53-56 (2007).

4. Strange hadron elliptic flow from 200 GeV Cu + Cu collisions,

   Shusu Shi, EP Systema, Budapest, ISBN **978 963 86934 3 3**, 43-48, 2008.

5. Event anisotropy v_2 at STAR,

   Shusu Shi, *Nucl. Phys. A* **830**, 187-190 (2009).

STAR Publications as principal author:

6. Identified particle production, azimuthal anisotropy, and interferometry measurements in Au+Au collisions at $\sqrt{s_{NN}} = 9.2$ GeV,

   B.I. Abelev, et al., STAR collaboration, *Phys. Rev. C* **81**, 024911 (2010).

7. Charged and strange hadron elliptic flow in Cu+Cu collisions at $\sqrt{s_{NN}} = 62.4$ and 200 GeV,

   B.I. Abelev, et al., STAR collaboration, arXiv:1001.5052, submitted to *Phys. Rev. C.*

8. Anisotropic flow at RHIC and the deviation from the ideal hydrodynamic limit,

   B.I. Abelev, et al., STAR collaboration, STAR internal review, target journal: *Phys. Rev. Lett.*

9. Breaking of number of constituent quark scaling at high transverse momentum for Au+Au Collisions at $\sqrt{s_{NN}} = 200$ GeV,

   B.I. Abelev, et al., STAR collaboration, STAR internal review, target journal: *Phys. Rev. C.*

STAR Publications:

10. Hadronic resonance production in d+Au collisions at $\sqrt{s_{NN}}$ =200 GeV measured at the BNL Relativistic Heavy Ion Collider,

    B.I. Abelev, et al., STAR collaboration, *Phys. Rev. C* **78**, 044906 (2008).

11. Spin alignment measurements of the $K^{*0}(892)$ and $\phi(1020)$ vector mesons in heavy ion collisions at $\sqrt{s_{NN}} = 200$ GeV,

    B.I. Abelev, et al., STAR collaboration. *Phys. Rev. C* **77**, 061902 (2008).

12. Centrality dependence of charged hadron and strange hadron elliptic flow from $\sqrt{s_{NN}} = 200$ GeV Au+Au collisions,

    B.I. Abelev, et al., STAR collaboration. *Phys. Rev. C* **77**, 054901 (2008).

13. Indications of Conical Emission of Charged Hadrons at the BNL Relativistic Heavy Ion Collider,

    B.I. Abelev, et al., STAR collaboration, *Phys. Rev. Lett.* **102**, 052302 (2009).

14. Charge Independent(CI) and Charge Dependent(CD) correlations vs. Centrality from $\Delta\phi\Delta\eta$ Charged Pairs in Minimum Bias Au+Au Collisions at $\sqrt{s_{NN}}$ = 200 GeV,

    B.I. Abelev, et al., STAR collaboration, arXiv:0806.0513. Submitted to *Phys. Rev. C.*

15. System-Size Independence of Directed Flow Measured at the BNL Relativistic Heavy-Ion Collider,

    B.I. Abelev, et al., STAR collaboration, *Phys. Rev. Lett.* **101**, 252301 (2008)

16. Beam-energy and system-size dependence of dynamical net charge fluctuations,

    B.I. Abelev, et al., STAR collaboration, *Phys. Rev. C* **79**, 024906 (2009)

17. Systematic measurements of identified particle spectra in pp, d+Au, and Au+Au collisions at the STAR detector,

    B.I. Abelev, et al., STAR collaboration, *Phys. Rev. C* **79**, 034909 (2009)

18. Measurements of ϕ meson production in relativistic heavy-ion collisions at the BNL Relativistic Heavy Ion Collider (RHIC),

    B.I. Abelev, et al., STAR collaboration，*Phys. Rev. C* **79**, 064903 (2009)

19. Energy and system size dependence of ϕ meson production in Cu+Cu and Au+Au collisions,

    B.I. Abelev, et al., STAR collaboration, *Phys. Lett. B.* **673**, 183 (2009)

20. Observation of Two-Source Interference in the Photoproduction Reaction AuAu $\rightarrow$ AuAuρ^0,

    B.I. Abelev, et al., STAR collaboration, *Phys. Rev. Lett.* **102**, 112301 (2009)

21. Measurement of D^* mesons in jets from p+p collisions at $\sqrt{s_{NN}}$ =200 GeV,

    B.I. Abelev, et al., STAR collaboration, *Phys. Rev. D* **79**, 112006 (2009)

22. K/π Fluctuations at Relativistic Energies,

    B.I. Abelev, et al., STAR collaboration, *Phys. Rev. Lett.* **103**, 092301 (2009)

23. Pion interferometry in Au+Au and Cu+Cu collisions at $\sqrt{s_{NN}}$ = 62.4 and 200 GeV,

    B.I. Abelev, et al., STAR collaboration, *Phys. Rev. C* **80**, 024905 (2009)

24. J/Ψ production at high transverse momentum in p+p and Cu+Cu collisions at $\sqrt{s_{NN}}$ = 200 GeV,

    B.I. Abelev, et al., STAR collaboration, *Phys. Rev. C* **80**, 041902(R) (2009)

25. System size dependence of associated yields in hadron-triggered jets,

    B.I. Abelev, et al., STAR collaboration, *Phys. Lett. B* **683** (2010) 123

26. Growth of Long Range Forward-Backward Multiplicity Correlations with Centrality in Au+Au Collisions at $\sqrt{s_{NN}}$ = 200 GeV,

    B.I. Abelev, et al., STAR collaboration, *Phys. Rev. Lett.* **103**, 172301 (2009)

27. Center of mass energy and system-size dependence of photon production at forward rapidity at RHIC,

    B.I. Abelev, et al., STAR collaboration, *Nucl. Phys. A* **832** (2009) 134

28. Neutral pion production in Au+Au collisions at $\sqrt{s_{NN}}$ = 200 GeV,

    B.I. Abelev, et al., STAR collaboration, *Phys. Rev. C* **80**, (2009) 044905

29. Long range rapidity correlations and jet production in high energy nuclear collisions,

    B.I. Abelev, et al., STAR collaboration, *Phys. Rev. C* **80** (2009) 064912

30. Yields and elliptic flow of $d(\overline{d})$ and ${}^3He(\overline{{}^3He})$ in Au+Au collisions at $\sqrt{s_{NN}}$ = 200 GeV,

    B.I. Abelev, et al., STAR collaboration, arXiv:0909.0566v1, submitted to *Phys. Lett. B*

31. Azimuthal Charged-Particle Correlations and Possible Local Strong Parity Violation,

B.I. Abelev, et al., STAR collaboration, *Phys. Rev. Lett.* **103** (2009) 251601

32. Observation of charge-dependent azimuthal correlations and possible local strong parity violation in heavy ion collisions,

B.I. Abelev, et al., STAR collaboration, arXiv:0909.1717v1, submitted to *Phys. Rev. C.*

33. Longitudinal Spin Transfer to Lambda and Anti-Lambda Hyperons in Polarized Proton-Proton Collisions at $\sqrt{s_{NN}} = 200$ GeV,

B.I. Abelev, et al., STAR collaboration, *Phys. Rev. D* **80** (2009) 111102

34. Observation of an Antimatter Hypernucleus,

B.I. Abelev, et al., STAR collaboration, arXiv:1003.2030v1, accepted by *Science.*

35. Longitudinal double-spin asymmetry and cross section for inclusive neutral pion production at midrapidity in polarized proton collisions at $\sqrt{s_{NN}} = 200$ GeV,

B.I. Abelev, et al., STAR collaboration, *Phys. Rev. D* **80** (2009) 111108

36. Identified high p_T spectra in Cu+Cu collisions at $\sqrt{s_{NN}} = 200$ GeV,

B.I. Abelev, et al., STAR collaboration, arXiv:0911.3130v1, submitted to *Phys. Rev. C.*

37. Observation of $\pi^+\pi^-\pi^+\pi^-$ Photoproduction in Ultra Peripheral Heavy Ion Collisions at STAR,

B.I. Abelev, et al., STAR collaboration, arXiv: 0912.0604v1, submitted to *Phys. Rev. C.*

38. Studying Parton Energy Loss in Heavy-Ion Collisions via Direct Photon and Charged-Particle Azimuthal Correlations,

B.I. Abelev, et al., STAR collaboration, arXiv: 0912.1871v1, submitted to *Phys. Rev. Lett.*

39. Inclusive π^0, η, and direct photon production in p+p and d+Au collisions at $\sqrt{s_{NN}}$ = 200 GeV,

    B.I. Abelev, et al., STAR collaboration, arXiv: 0912.3838v1, submitted to *Phys. Rev. C.*

40. Upsilon cross section in p+p collisions at $\sqrt{s_{NN}}$ = 200 GeV,

    B.I. Abelev, et al., STAR collaboration, arXiv: 1001.2745v1, submitted to *Phys. Rev. C.*

41. Three-particle coincidence of the long range pseudorapidity correlation in high energy nucleus-nucleus collisions,

    B.I. Abelev, et al., STAR collaboration, arXiv:0912.3977v2, submitted to *Phys. Rev. Lett.*

42. Longitudinal scaling property of the charge balance function in Au+Au collisions at $\sqrt{s_{NN}}$ = 200 GeV,

    B.I. Abelev, et al., STAR collaboration, arXiv:1002.1641v1, submitted to *Phys. Lett. B.*